AD-A171 480 HIGH TEMPERATURE MONOTONIC AND CYCLIC DEFORMATION IN A 1/2
DIRECTIONALLY SOLI..(U) GEORGIA INST OF TECH ATLANTA
SCHOOL OF MATERIALS ENGINEERING.. E S HURON MAY 86
UNCLASSIFIED NASA-CR-175101 NAG3-503 F/G 11/6 NL

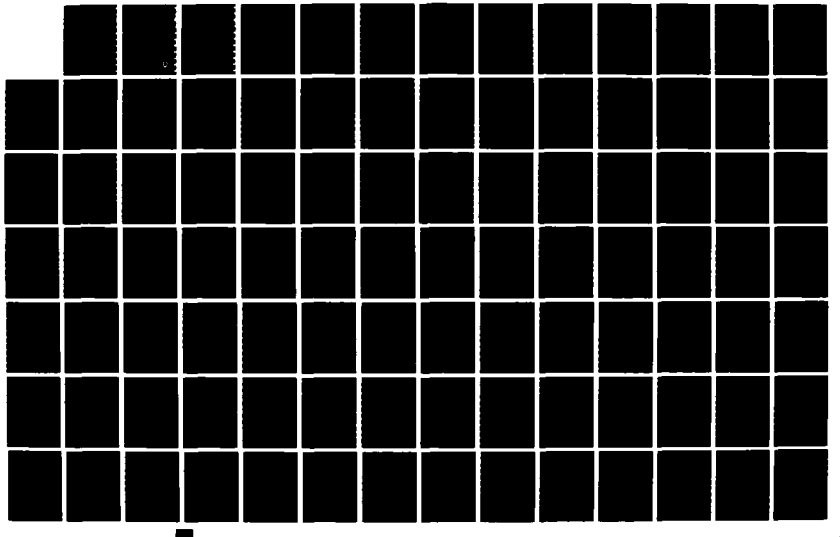

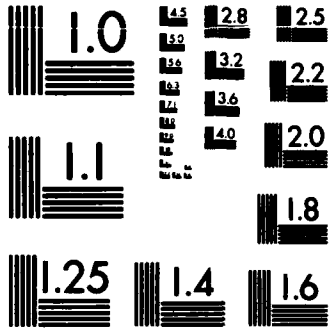

NASA
Contractor Report 175101

USAAVSCOM
Technical Report 86-C-19

High Temperature Monotonic and Cyclic Deformation in a Directionally Solidified Nickel-base Superalloy

Eric Huron
Georgia Institute of Technology
Atlanta, Georgia

May 1986

Prepared for
Lewis Research Center
Under Grant NAG 3-503

TABLE OF CONTENTS

SUMMARY

The relationships between mechanical properties and microstructure were investigated for the nickel-base superalloy, MAR-M246+Hf, in the directionally solidified (DS) form. This alloy is currently being used in the turbo pump blades of the Space Shuttle Main Engine. MAR-M246+Hf contains many alloying elements and a high volume fraction of the gamma prime precipitate to provide excellent high temperature properties.

Mechanical testing was done in two modes - tension and strain-controlled low cycle fatigue. Testing was done at two strain rates at temperatures ranging from room temperature to 1093°C, using a computer-controlled servohydraulic machine. All specimens were carefully examined through optical and electron microscopy.

In tension, the temperature and strain rate were observed to significantly affect the properties and microstructure of the material. Yield strength was constant up to 704°C, and at higher temperatures a drop in strength was seen. Lower strain rates decreased strength at the higher temperatures. These effects were due to changes in the deformation mode in the material.

In low cycle fatigue, temperature and strain rate were again very important. For a given plastic strain

range, lives were shortest at 704°C and longest at 1093°C. Failure at the lower temperatures initiated due to slip bands emanating from carbides, and propagation was transgranular or crystallographic. At the higher temperatures failure was initiated by the formation of oxide spikes, with non-crystallographic propagation. Lower strain rates reduced life at 704°C and increased lives at the higher temperatures. The effects of strain rate could be explained by the effective stresses resulting from the applied strains, and corresponded to microstructural changes in the material depending on test condition. A trend of increasing slip homogeneity with increasing temperature and decreasing strain rate was observed.

The longitudinal grain boundaries were found to influence slip behavior. At the lower test temperatures in fatigue, secondary slip was observed on the surfaces of the specimens at grain boundaries. The degree of secondary slip was found to be related to the misorientation between the grains.

CHAPTER I

INTRODUCTION

Materials used in gas turbine engines are subjected to conditions of high mechanical stress, thermal cycling, and environmental attack. Nickel-base superalloys have been used successfully in these applications for several decades. At first these alloys were used in conventionally cast or wrought form, with randomly oriented grains. The demand for increased fuel efficiency has led to increased operating temperatures, which increase the possibility of failure at grain boundaries normal to the stress axis. To counter this problem, directional solidification techniques have been developed to produce columnar-grained and single crystal turbine blades. The columnar-grained blades, also called directionally solidified (DS) blades, contain primarily longitudinal boundaries, while the single crystal (XL) blades contain no grain boundaries. Because of the directional structure, these materials are highly anisotropic.

The alloy MAR-M246 is currently being used in the DS form for turbine blades of the high pressure turbopump of the Space Shuttle Main Engine (SSME). The single crystal alloy PWA 1480 is being considered as a replacement material

to improve performance. To aid in understanding how the anisotropy of the materials affects their constitutive behavior, or stress-strain response, a comprehensive program to study the fatigue and tensile properties of the two alloys was undertaken, one portion of which is reported in this thesis. The variables included strain rate, strain range, environment, and temperature, with tests to failure and interrupted tests. Testing of specimens with different stress axis orientations was included in the test matrices.

This thesis reports the results of the initial phase of the study on the DS alloy, MAR-M246+Hf. Tensile and Low Cycle Fatigue (LCF) tests have been conducted in air, at temperatures of room temperature, 704°C (1300°F), 927°C (1700°F), and 1093°C (2000°F). All tests in this phase of the program have been on [001] oriented specimens tested to failure. Failure modes and the effects of deformation on the microstructure have been studied.

In addition to this introduction chapter, the thesis is organized as follows: Chapter II presents a comprehensive literature review covering the physical metallurgy and background of directional solidified nickel-base superalloys. Chapter III includes details of the procedure used, with additional details given in the two Appendices. Chapter IV presents the results and pertinent discussion, and Chapter V contains summary statements and conclusions. Tables and Figures follow the Appendices.

CHAPTER II

LITERATURE REVIEW

A great deal of literature on all aspects of fatigue is available, including several reviews (1-5). Wells et. al. (1) discuss mechanisms of deformation including slip mode, strain softening/hardening, and grain boundary effects. Antolovich (4) discussed high temperature fatigue with a particular emphasis on damage mechanisms. An important point made in this article is that each material has unique fatigue characteristics and different models may be required for different materials. The following discussion is presented to highlight the important characteristics of the metallurgy of nickel-base superalloys and how their mechanical properties are related to their structure. Emphasis will be placed on effects particularly associated with directional solidification. The reader should consult the reviews cited (1-5) for additional background information.

Physical Metallurgy

The physical metallurgy of Ni-base superalloys has been covered in several review papers (6-8). The following summary is drawn mainly from these references.

Composition and Phases

Nickel-base superalloys contain a variety of alloying elements to achieve different desirable properties. The compositions of the alloys MAR-M200 and MAR-M246, including the composition of the alloy under investigation, are given in Table 1. The phases and effects of the alloying elements are summarised below.

Matrix. The matrix is FCC nickel with the solid solution strengthening elements V, Cr, Mo, W, Fe, and Co. Al can also provide solid solution strengthening (6).

Gamma Prime (γ'). Gamma prime is an ordered precipitate of chemical composition Ni_3Al. It has an LI_2 structure, with Ni atoms at face centers and Al atoms at cube corners. Other γ' forming elements which may substitute for Ni are Ti, Nb, and Ta. γ' has been found to remain ordered up to elevated temperatures (9).

The precipitate is coherent with the FCC γ matrix, but depending on composition the γ' and γ may have different lattice parameters. This leads to coherency strain, or misfit. The misfit parameter is defined by the equation (10):

$$\frac{a_p - a_m}{\bar{a}} \qquad (2.1)$$

a_p is the unconstrained lattice parameter of extracted γ', a_m is the lattice parameter of the matrix, and $\bar{a}$ is the

average lattice parameter. Note that the lattice parameter of extracted γ' (δ) and in situ γ' (ε) are not necessarily the same. The unconstrained and in situ lattice parameters may be related through the equation (10):

$$\varepsilon = \delta \cdot \frac{1 + \nu}{1 + 2k + \nu(1-4k)} \qquad (2.2)$$

ν is the Poisson's ratio of the precipitate, and k represents the ratio of the shear modulus of the matrix to the shear ratio of the precipitate. An approximate relationship can be obtained by letting ν be 1/3 and k be 1.0. This gives $\varepsilon = 2/3\ \delta$ as an estimate.

Small mismatch and small precipitate size tend to produce spherical γ'. Large mismatch and large precipitate size tend to produce cuboidal γ'. Mismatch is affected by composition (11-13). Ti, Nb, and C increase mismatch by expanding a_p, while Cr, Mo, and Fe decrease mismatch by expanding a_m, and Co has little reported effect.

Although γ' is usually thought to precipitate in the γ matrix, precipitation of γ in γ' particles has been seen in aged alloys (14). This is favored for large, coherent γ'.

Carbides. The carbide forming elements, in order of decreasing effectiveness (8) are: V, Ti, W, Mo, Cr, Nb, and Ta. Note that this is not as predicted by classical thermodynamics.

Three major classes of carbides are common. MC carbides are FCC in structure and form between carbon and refractory metal elements. MC carbides can form intragranularly as well as at grain boundaries and in the intragranular form can exhibit a network-like "Chinese script" morphology. MC carbides are relatively stable at high temperatures for short exposure times (15) but decompose with increasing time at high temperatures into M_6C and $M_{23}C_6$ (15,16). MC carbide forming elements include Ta, Nb, Ti, and V (6) and W (15).

Hafnium is also an MC carbide former and has been reported to be a stronger carbide former than Ta, Nb, Ti, or V (17). Hafnium segregates to interdendritic regions in DS alloys (18). The most important benefit of Hf additions is to alter the MC carbide morphology from the Chinese script morphology to a uniform dispersion of discrete carbide particles. This effect has been observed in 713-LC (19,20) and in B-1900, U-700, and MAR-M246 (19). Kotval and coworkers (19) also observed that Hf changed the nature of the grain boundaries from relatively smooth and planar to irregular and interlocking. In MAR-M200, a high volume fraction γ' alloy, Hf additions increased the amount of γ/γ' eutectic constituent formed, in addition to affecting the MC carbide morphology (21). The addition of 2 w/o Hf improved creep rupture life and creep ductility and tensile ductility in the transverse direction. In the longitudinal

direction, creep rupture life was unaffected, but creep rupture ductility and tensile ductility were improved. These results are presented in Table 2. Similar results were reported for MAR-M246 (22) and are given in Table 3.

$M_{23}C_6$ carbides are complex cubic and are usually of Cr composition, but Mo, W, and Ni can substitute for the Cr, with $Cr_{21}W_2C_6$ often observed. These carbides tend to form at grain boundaries during cooling or can be made to form with a carbide precipitation treatment (16). They are generally stable at intermediate temperatures in the range 870-980°C (8), but their behavior depends on specific alloy composition.

M_6C carbides are similar instructure to $M_{23}C_6$ and tend to form in grain boundaries, at high temperatures and after long exposures (15,16). Their formation is favored when Mo and W are present (6).

Other Phases. Boron is added to superalloys to form borides, which provide grain boundary strengthening. Borides generally have the formula M_3B_2 (16). Small amounts of elemental boron and zirconium are thought to occupy grain boundary positions and restrict grain boundary diffusion (23). In B-1950, an alloy containing a large amount of boron (0.20 w/o), large, coarse M_3B_2 borides were present after casting (24). After heat treatment at 1079°C for 4 hours and 899°C for 10 hours, fine particles of another boride identified as MB_{12} was reported. Electron microprobe

analysis indicated this phase was rich in Cr and W. Note that most superalloys, including MAR-M246, contain less than 0.02% boron.

The so-called Topologically Close-Packed Phases (TCP) can form and are detrimental to mechanical properties (25). These are the sigma and mu phases. σ phase is associated with the $M_{23}C_6$ carbide and μ phase is associated with the M_6C carbide. They have a plate-like morphology. Sigma phase has received the most attention. It forms in the range 650 to 925°C. This phase usually nucleates on $M_{23}C_6$ carbides, often within the matrix, and causes reductions in stress rupture strength and ductility. σ formation can be minimized through chemistry control, particularly of cobalt, and the PHACOMP (8) computer composition calculation method has been successfully applied inalloy design. Another detrimental phase is the eta phase, which has an Ni_3X composition and forms from γ' with high Ti, Nb, or Ta content with a HCP structure (8). Eta may precipitate in cellular form at grain boundaries, causing a reduction in notched stress rupture strength, or eta may precipitate intragranularly, causing a reduction in tensile strength (7). The formation of eta as Ni_3Ti has been shown to cause a loss of hardness and to be retarded by the presence of tungsten (26). Boron also retards the formation of eta (6).

Summary of the Roles of Alloying Elements. Nickel of

course provides the basic FCC matrix. Ni has a high melting point of 1453°C, a high tolerance for alloying and forms protective oxide scales (6).

Chromium is mainly added to form a Cr_2O_3 - rich protective scale. It also provides solid solution strengthening and forms carbides. Cr partitions to the matrix (27).

Aluminum is added to form γ'. It partitions in a 5:1 ratio between the γ' and the matrix (27). In the matrix it provides solid solution strengthening and helps form protective oxide scales (6).

Titanium is also a γ' former, partitioning strongly to the precipitate (27). Ti provides strengthening and raises the Antiphase Boundary Energy (APB) of the precipitate and the Ti/Al ratio is important in determing the degree of mismatch. Ti reduces the solubility of Mo in the precipitate (10) and is an MC carbide former.

Tungsten partitions about evenly between the matrix and precipitate, and molybdenum partitions in a ratio of 3:1 between the matrix and precipitate (27). These elements are solid solution strengtheners and M_6C carbide formers. Mo and W reduce the solubility of Al in the matrix (10) and thereby promote precipitate formation.

Tantalum forms MC carbides, enhances oxidation resistance, and provides some solid strengthening (11). It partitions strongly to the γ' (27). Niobium also partitions

to the γ', where it increases the APB energy (28).

Cobalt lowers the stacking fault of the matrix, raises the γ' solvus temperature (29), and close control of Co is necessary to avoid sigma phase formation. Co partitions about 1:2 between the precipitate and the matrix (27). When Co levels were reduced in Waspaloy, tensile properties were only slightly affected, but creep properties were greatly diminished (30). In a recent study on the role of Co in MAR-M247 (31), it was found that decreasing levels of Co from 10% to 0% caused a decrease in γ' volume fraction, an increase in γ' size, a decrease in Ti and W concentration in γ' (lowering the APB energy), and a decrease in Cr and Al concentrations in γ. Decreasing Co also caused a tendency for increased carbide precipitation and formation of a continuous carbide grain boundary film. As a result, tensile strengths were only slightly affected, but creep rupture times were decreased with decreasing Co content. Thus the primary importance of Co is in improving creep properties.

Carbon, boron, zirconium, and hafnium are associated with carbides and grain boundary effects. B, Zr, and Hf improve ductility. B forms grain boundary stabilizing borides. Hf promotes a benign MC carbide morphology, increases the amount of eutectic at grain boundaries, and changes grain boundary shape (18). Hf causes significant effects on ductility and creep properties (21) as already

discussed.

Strengthening Mechanisms

Solid Solution Strengthening of γ.

Hardening can occur in the matrix by solid solution strengthening elements. However, solid solution strengthening is weak compared to precitate strengthening in high Vf γ' alloys. The degree of hardening is related to lattice expansion and electron vacancy number (6). Mott and Nabarro (32) proposed an equation for the yield stress of a dilute solid solution hardened by lattice expansion:

$$\tau = 2G\varepsilon c \qquad (2.3)$$

G is the shear modulus, c is the concentration, and ε is the lattice misfit from the solute atoms. Modulus mismatch and short range order have also been suggested as contributors to solid solution strengthening (33).

Solid solution strengthening weakens at higher temperatures. Above about 0.6 Tm diffusion becomes important, and slower diffusing elements such as Mo and W are the most effective hardeners.

Precipitate Strengthening.

In alloys containing γ', the γ' provides a major part of the strength. Several factors influence the amount of strengthening: the antiphase boundary (APB) energy and flow

stress of the precipitate itself, the degree of coherency strain between the γ' and the matrix, and the particle size and volume fraction (Vf). Much understanding of the behavior of nickel-base superalloys has resulted from studies on single-phase γ' deformation.

The flow stress of the gamma prime phase is influenced by composition. In particular Ti has been shown to increase the strength of γ' because it substitutes for Al and provides strength through lattice strain (34). Rawlings and Staton-Bevan (35) showed that the alloy strengthening behavior in Ni_3Al was a function of the degree of stoichiometry. Al-rich Ni_3Al compositions were found to be stronger than stoichiometric and Ni-rich compositions. For elements that substituted for Al, the strengthening was found to be a function of the atomic size difference, and considerable strengthening was observed in Al-rich and stoichiometric compositions, but little strengthening was observed in Ni-rich compositions. For elements that substituted for Ni, little strengthening was observed, regardless of stoichiometry.

The most remarkable characteristic of γ' is that is displays an increasing flow stress with increasing temperature to a peak at about 760°C. This has been studied extensively (28,34-45). Pope and Ezz (36) have presented a very complete review on the temperature dependence of the mechanical properties of alloys with a high Vf of γ'.

The ordered structure of γ' is the reason for the unusual increase in yield stress with increasing temperatures. The LI_2 structure has Ni atoms at cube faces and Al atoms at cube corners, with an ordered nearest neighbor arrangement. In the normal FCC lattice, movement of atoms by a unit lattice translation on adjacent planes does not cause a change in the nearest neighbor arrangement and the dislocations are normally a/2<110> type (37). However, movement of atoms on adjacent planes in the LI_2 structure can create antiphase boundary (APB) from improper nearest neighbors (38). As a result, a/2 <110> dislocations occur in pairs, in an arrangement called a superlattice dislocation or superdislocation (36). The net Burger's vector is a<110> which does not disrupt the superlattice nearest neighbor arrangement, over long distances. However, between the a/2 <110> dislocations a region of APB is created. When the dislocation pair moves through the lattice, the leading dislocation creates APB and the trailing dislocation annihilates it. The energy of the dislocation pair is a balance between the APB pushing them together and their elastic repulsion pushing them apart. The a/2 <110> dislocations themselves may be separated into partial dislocations (Figure 1).

The driving force to eliminate or reduce the APB gives rise to several possible arrangements of stacking faults and dislocation reactions in γ'. Stacking faults can

occur in three variations in the superlattice (39): as intrinsic/extrinsic faults (SISF/SESF), as APB faults, or as complex faults (a combination of APB and SISF). One a/2<110> dislocation can form two a/3 <112> dislocations and an intrinsic fault. Two a/2 <110> dislocations can form three a/3<112> dislocations and a combination of intrinsic and extrinsic faults. APB faults are created by {111} a/2<110> dislocations, and complex faults are created through {111} a/6<110> shear displacements (39). The preferred reaction must depend on the relative strength of the APB. SISF faults have been reported for pure γ' (40), and SISF/SESF faults have been observed in MAR-M200 (41).

Flinn (38) considered the geometry of the LI_2 superlattice and demonstrated that the APB energy was different on different planes. In particular he showed that the APBE on {001} planes is lower than on {111} planes. He proposed that superlattice dislocations could rearrange by diffusion, aided by the reduction in APB energy, to cube planes, where the dislocations became immobile. He proposed that this would account for the observed temperature dependence of the flow stress of γ'. Flinn's model is incomplete because the flow stress of γ' increases even at low temperatures where diffusion is insignificant.

Kear and Wilsdorf (42),Thornton, Davies, and Johnson (43) and Takeuchi and Kuramoto (40) based explanations of

the temperature dependence of the flow stress of γ' on the "cross-slip" model. In this model screw segments of a/2 <110> {111} dislocations cross-slip onto {010} planes where they are immobile at intermediate temperature, leading to strain hardening. Above the peak temperature {010} slip and thermally activated dislocation movement occur easily enough for a drop in strength to be seen. The cross-slip model seems to be able to explain the behavior of the strength of γ' fairly well at lower temperatures. The transition from octahedral slip to cube slip has been well documented (40,43,44). Takeuchi and Kuramoto (40) and Kuramoto and Pope (44) found an orientation dependence for the flow stress and that the resolved shear stress for octahedral slip depended on the resolved shear stress for cube slip. Lall and coworkers (28) observed some differences in the flow stress between tension and compression. To explain this they added a term to the theory of Takeuchi and kuramoto to account for constriction of Shockley partial dislocations on (111). These partials consist of parallel screw and antiparallel edge segments. A change in direction in the applied force (tension vs. compression) will have the opposite effect on the edge segments and therefore a different flow stress is seen between tension and compression. Most recently Ezz, Pope, and Paidar (45) have added another term to account for the constriction of Shockley partials on (1-11) as well. By considering a total

of four Schmid factors these authors were able to explain the behavior of tensile and compressive flow stress throughout the unit triangle.

The cross-slip model process depends on the constriction of partial dislocations and therefore changing the APB energy should effect the strength. This was observed for alloys with Nb additions (28), which increased the APB energy. These alloys showed greater initial stresses, easier cross-slip, and a larger orientation dependence.

In a γ/γ' alloy, the behavior of the alloy parallels the behavior of the pure γ', with additional complications. One additional factor already mentioned is the degree of misfit, which influences the mechanism and effectiveness of precipitate strengthening. The effect of misfit on strength was studied by Decker and Mihalisin (1). They designed alloys with varying compositions, chosen in an attempt to keep all but one variable constant, and measured the mismatch. They found that alloys with increased mismatch showed the greatest increases in hardness. Si was added to test for solid solution strengthening, and Mn was added to vary APB, but neither of these additions produced observed effects.

Grose and Ansell (13) have also studied the effect of coherency strain on hardness. They used four groups of alloys based on Ni-15Cr-Al-Ti-Mo. By varying the Ti/Al

ratio and varying the Mo content they varied the misfit and APB. They also included control alloys hardened by solid solution strengthening. Grose and Ansell measured mismatch using extracted γ' and calculated the corresponding value of in situ mismatch. They found a linear relationship between misfit and flow stress, with the relationship degenerating at higher temperatures. They also made microstructural examinations of deformation modes in tension. Grose and Ansell found that for alloys with high misfit and either high or low APB, deformation occurred by bypass of dislocations around γ', with a strong correlation between misfit and flow stress increase. Alloys with low misfit and high APB energy deformed through particle shear by intrinsic/extrinsic stacking faults, and alloys with low misfit and low APB energy deformed by particle shear by superlattice dislocations coupled to APB. Thus misfit tends to act as a barrier to penetration of γ' by dislocations, influencing strength and deformation mode.

Grose and Ansell showed that the thermal expansion coefficients of γ and γ' differ. This is significant because the lattice mismatch must change with temperature, which should be considered in measuring lattice mismatch in experiments. If lattice mismatch measurements are made at low temperatures and then used to draw conclusions for elevated temperature behavior, the variation of mismatch should be taken into effect. Ideally the mismatch should be

measured at the temperature of interest using elevated temperature x-ray diffraction equipment.

Elevated service temperatures, above about 0.6 Tm (6), will cause γ' to coarsen. Coarsening is analogous to overaging - the interparticle distance increases and looping is increasingly favored. Coarsening is generally detrimental to strength properties and beneficial to ductilty properties (15). The slow-diffusing elements Ni and Ta partition to the γ' and retard coarsening. Coarsening is strongly affected by the degree of misfit. This has recently been studied by Ricks, Porter, and Ecob (47). This work looked at growth of γ' during aging. This paper proposed that growth of the precipitate starts with spheres, then cuboids, then cuboidal arrays. The cuboidal arrays were explained to grow as a result of preferred growth of cuboid corners in the [111] direction. However, in this study only isolated particles were observed and the growth was done just under the solidus temperature, minimizing impingement from neighboring particles. The study found that in positive misfit alloys (Nimonic 80A and Nimonic 90) the change to cuboids occurred at small particle sizes, as growth occurred during aging. In negative misfit allys (Nimonic 105 and Udimet 720) the γ' remained spherical to a larger size.

In addition to misfit, the particle size and Vf of γ' also influence strengthening in γ/γ' alloys. In general,

particle shearing by dislocations is favored by large Vf, small interparticle spacing as well as small misfit (48). As long as the precipitate is being sheared, increased particle size increases strength. However, for a given γ' volume fraction, increasing particle size, either during aging heat treatment or coarsening during service, corresponds to increased interparticle spacing and a tendency for looping to occur.

Increasing the Vf of precipitate is one of the design goals of several modern alloys, including MAR-M200, MAR-M246, and MAR-M247. These alloys contain roughly 60 volume percent of γ'. In γ/γ' alloys, the effects of γ' misfit, coarsening, and Vf all combine to determine deformation behavior. Deformation behavior in γ/γ' alloys will be discussed in more detail in later sections.

Carbides.

Carbides can serve as a "strengthening mechanism" because of their relationship to grain boundaries. $M_{23}C_6$ carbides in particular tend to form at the grain boundary. A dispersed network of such carbides on the boundaries is beneficial to creep rupture life by limiting sliding, while a continuous grain boundary carbide film has been shown to reduce rupture life, impact resistance, and ductilty (12). This is one of the reasons for Hf additions - to break up the continuous mc "Chinese script" carbide morphology. In studies on MAR-M200 (49,50), MC intragranular carbides were

shown to be important as crack initiation sites in fatigue at room temperature and 760°C. MC carbides were present in the material both as cast and after solutionizing and aging. Some cracks were present around the carbides after casting, and during fatigue, cracks initiated at these sites. Most effects of carbides are due to interactions with grain boundaries and dendrite boundaries.

Grain Size and Grain Boundary Effects

It is well known that grain boundaries have definite effects on properties. In a previous section on precipitate strengthening, results of several single crystal studies were cited. When a single crystal is deformed, the tensile axis rotates towards the slip direction. When a polycrystalline material yields, rotation of individual grains is constrained by neighboring grains. More constraint is provided by finer grains, and at lower temperatures flow stress and hardness of metals increases with finer grain size.

Two approaches have been used to explain relationships between grain size and strength. The first is based on the consideration that if dislocations are piled up at a grain boundary, the stress concentration must be sufficient to nucleate slip in the adjacent grain (51). The equation is the familar Hall-Petch equation (52,53):

$$\sigma = \sigma_o + kd^{-1/2} \qquad (2.4)$$

where σ is the yield stress and σ_o is a constant related to the lattice friction stress. d is the grain size, and k is the slope of the line through the data. The value of k has been considered to be related to dislocation pinning by solute atoms. This would predict a strong temperature dependence for k, which is seen under certain yielding conditions (54). The equation was originally developed empirically and equally good agreement with the data has been shown to result from using d^{-1} or $d^{-1/3}$ (55). Li has presented a similar equation for the flow stress expressed in terms of dislocation density, ρ (56):

$$\sigma = \sigma_o + \alpha b \mu \rho^{-1/2} \qquad (2.5)$$

σ has the same significance, μ is the shear modulus, b is the Burgers vector, and α is a numerical constant. Both of these equations predict what is commonly accepted: an inverse square root dependence of strength on grain size or dislocation cell size.

Under certain conditions, the rate of creep is dependent on grain size. For very large grain sizes, creep rates are independent of grain size, but with decreasing grain sizes, faster creep rates are often observed (57). This is due to the influence of grain size on grain boundary

sliding, Nabarro-Herring (lattice diffusion) creep, and Coble (grain boundary diffusion) creep. For MAR-M200, increasing grain size has been shown to reduce creep rate (58). The shape and composition of the grain boundaries also influence the rate of creep (59,60). Changing the shape from smooth and planar to rough and convoluted acts as a barrier to sliding (60), which is another benefit of Hf additions, which have been observed to change the shape of the boundary in Ni-base superalloys (19,20). The segregation of boron and zirconium to grain boundaries prevents depletion by oxidation of other elements in the grains adjacent to the boundary (6). Carbides also tend to form at grain boundaries, and provide a pinning mechanism.

Under certain conditions, the rate of creep is dependent on grain size. For very large grain sizes, creep rates are independent of grain size, but with decreasing grain sizes, faster creep rates are often observed (57). This is due to the influence of grain size on grain boundary sliding, Nabarro-Herring (lattice diffusion) creep, and Coble (grain boundary diffusion) creep. For MAR-M200, increasing grain size has been shown to reduce creep rate (58). The shape and composition of the grain boundaries also influence the rate of creep (59,60). Changing the shape from smooth and planar to rough and convoluted acts as a barrier to sliding (60), which is another benefit of Hf additions, which have been observed to change the shape of

the boundary in Ni-base superalloys (19,20). The segregation of boron and zirconium to grain boundaries prevents depletion by oxidation of other elements in the grains adjacent to the boundary (6). Carbides also tend to form at grain boundaries, and provide a pinning mechanism.

In DS alloys, the material is polycrystalline but in a special way: the growth direction and grain boundaries are parallel (usually to the stress axis), resulting in a structure of aligned columnar grains. The grain size vs. strength relationships presented earlier and other general concepts based on conventional randomly oriented polycrystalline materials are still useful in providing insight but are not necessarily directly applicable. One area of research that has been helpful in understanding the role of grain boundaries in DS materials is the study of bicrystal and tricrystal deformation (61-66). Bicrystals and tricrystals consist of single crystals bonded in common grain boundary planes.

Aust and Chen (61) found that for aluminum bicrystals an increase in misorientation caused an increased flow stress, and an increase in the rate of strain hardening. Hauser and Chalmers (62) studied silver bicrystals. They found that bicrystals showed increased strain hardening, especially in the easy glide region, compared to single crystals. They also tested a "totally surrounded" bicrystal. This was made by making a core of a rectangular

bicrystal and surrounding it on all sides with slabs of a bicrystal with another orientation. This sample showed higher strengths than the bicrystals and approached the behavior of a polycrystalline sample, except that it showed a region of easy glide not seen in the polycrystalline sample. Hauser and Chalmers also tested a single crystal that had been annealed to produce a polycrystalline outer surface. This crystal was also harder than the single crystal. All the samples in this study showed yield points that were essentially the same.

Margolin and coworkers (63,64) have studied bicrystals of β brass. They found that bicrystals had much greater strength than single crystals and that tricrystals had somewhat higher strength than the bicrystals. They saw a size effect in the bicrystals, with increasing strength with decreasing size. Note that this correlates to the grain size-strength relationships of Petch-Hall (52,53) and Li (56). Margolin and coworkers explained the effect in bicrystals through this equation for the total stress, σ_T:

$$\sigma_T = \sigma_{BULK} \quad V_{BULK} + \sigma_{gb} V_{gb} \qquad (2.6)$$

σ_{BULK} is the average stress in the body of the grain, σ_{gb} is the average stress in the grain boundary rebion, V_{BULK} is the volume fraction of the grain interior, and V_{gb} is the volume fraction of the grain boundary region. As the size

of the bicrystals decreased, the relative volume of the harder grain boundary region increased, and the resulting stress increased. These results are direct evidence of strengthening caused by grain boundaries.

Hauser and Chalmers (62) and Hook and Hirth (65,66) have expressed the elastic compatibility requirements for bicrystal geometry (Fig. 2). In order for the grain boundary to remain compatable, the following requirements must hold:

$$\varepsilon_{zz}^{A} = \varepsilon_{zz}^{B} \qquad \varepsilon_{xx}^{A} = \varepsilon_{xx}^{B} \qquad \varepsilon_{xz}^{A} = \varepsilon_{xz}^{B} \tag{2.7}$$

The strain ε_{zz} is specified by the test. In general, these conditions require four slip systems to operate - three in one crystal and one in the other or two in each crystal. There are special configurations in which less than four systems are required. For the totally surrounded bicrystal (62) it was shown that at corners, the greater constraints necessitated the operation of more slip systems.

The strain components can be related to the slip systems. For small amounts of shear S_i on the slip system i, the strains are proportional to S_i (62,65):

$$\varepsilon_{xx} = S_i \, (e_i \cdot x) \, (g_i \cdot x) \tag{2.8}$$

$$\varepsilon_{zz} = S_i \, (e_i \cdot z) \, (g_i \cdot z)$$

$$\varepsilon_{xz} = S_i \left[(e_i \cdot x)\,(g_i \cdot z) + (e_i \cdot z)\,(g_i \cdot x)\right]$$

These are summed over the i slip systems. x, y, z are unit vectors in the x, y, and z directions. e_i is a unit vector normal to the slip plane, and g_i is a unit vector in the slip direction. Thus, in general, the contribution to strain in the grain boundary plane from plastic flow in each grain will be different. This causes plastic incompatibility.

The isoaxial bicrystal case can be compared to an ideal directionally solidified part, where there is no off-axis grain misorientation. For an isoaxial bicrystal under a uniaxial stress σz, only one of the compatibility requirements is satisfied: $\varepsilon_{zz} = \varepsilon_{zz}$. To determine the strains ε_{xx} and ε_{xz} for each component crystal, a tensor transformation must be made between the old axes corresponding to the cube axes in each crystal to a common new axis system in the grain boundary plane, with x' and z' in the plane and y' normal to it. The elastic strains resulting from the applied stress σ_z are:

$$\varepsilon'_x = S_{13}\,\sigma_z \qquad (2.9)$$

$$\varepsilon'_y = S_{23}\,\sigma_z$$

$$\varepsilon'_z = S_{33}\,\sigma_z$$

$$\varepsilon'_{xz} = S_{53}\,\sigma_z$$

$$\varepsilon'_{yz} = S_{43}\,\sigma_z$$

$$\varepsilon'_{xy} = S_{63}\,\sigma_z$$

The S_{ii}'s represent elastic compliance constants.

The significant result is that additional stresses are developed through the above strains, and these are the origin of a second incompatibility, elastic incompatibility. The elastic incompatibility must be considered because the resulting stresses may be sufficient to add to the local resolved shear stress and slip nucleation at grain boundaries could result. Hook and Hirth (65,66) observed that slip was nucleated at the grain boundaries and could be explained by considering both elastic and plastic incompatibility, but not by plastic strain effects alone.

Prakash (67) presented an alternative measure of the incompatibility for a DS superalloy based simply on rotational misorientation. Each grain is assumed to be very slightly misoriented from the [001] axis so that only one of the (111) <110> slip systems is operable, but with a small enough misorientation that the grain can be treated as having a [001] axis. The Miller indices of the grain boundary plane are [hko]. The slip vector normal to the

boundary is the projected length along the unit vector v:

$$v = \frac{[hko]}{||\ [hko]\ ||} = \frac{[hko]}{h^2 + k^2} \qquad (2.10)$$

It is assumed that [-101] is the Burger's vector of slip in each grain, and the grains are rotated relative to one another by an amount ϕ. The slip vector in grain a is a = [-101]. A rotation operation must be performed to bring the slip vector in grain b into a common coordinate system. In the orthonormal coordinate system, the rotation matrix R for a rotation about the axis [xyz] is given by:

$$R = \cos\theta \begin{bmatrix} 1 & 0 & 0 \\ 0 & 1 & 0 \\ 0 & 0 & 1 \end{bmatrix} + 1-\cos\theta \begin{bmatrix} xx & xy & xz \\ yx & yy & yz \\ zx & zy & zz \end{bmatrix} + \sin\theta \begin{bmatrix} 0 & -z & y \\ -z & 0 & -x \\ -y & x & 0 \end{bmatrix} \qquad (2.11)$$

For the present situation, [xyz] becomes [001]. R becomes:

$$\begin{bmatrix} \cos\theta & -\sin\theta & 0 \\ \sin\theta & \cos\theta & 0 \\ 0 & 0 & 1 \end{bmatrix}$$

After the rotation, b = [$\cos\theta$ $-\sin\theta$ 1]. The next step in the calculation is to obtain the components of a and b projected into the (001) plane. The boundary is assumed to be parallel to [001] and only the components of slip in the (001) plane, normal to the boundary, will be considered.

These are:

$$a_p = [-1 \; 0 \; 0]$$

$$b_p = [-\cos\theta \;\; -\sin\theta \;\; 0]$$

The difference in the vectors, c, is:

$$c = [-1 + \cos\theta \quad \sin\theta \quad 0]$$

To determine the component normal to the boundary, the dot product $c \cdot v$ is obtained.

$$c \cdot v = || c || \;\; || v || \;\; \cos\theta \qquad (2.12)$$

Performing the operation and simplifying gives the following result:

$$\Delta = \frac{-h}{h^2 + k^2} \; (1 - \cos\theta - k/h \sin\theta) \qquad (2.13)$$

This equation predicts increasing incompatibility with increasing degree of misorientation (θ). Note that the components of slip in the grain boundary plane, which may be significant, are not considered.

In a production DS part, there is the additional

complication of misorientation of the growth axis between adjacent grains. This gives a non-isoxial case. Elastic and plastic incompatibility will be present just as in the isoaxial case, and in addition, the effective modulus in each grain will be different and the Schmid factors for particular slip systems will be different. The effect of orientation differences on modulus is shown in Figure 4. Additional effects of directional solidification on properties will be discusses in a later section.

Tensile and Creep Deformation in γ/γ' Alloys

The flow stress of high Vf γ' alloys shows a peak at about 800°C, but while pure γ' shows increasing strength up to the peak temperature, γ/γ' alloys show relatively constant strength up to the peak temperature. This is due to the balance between softenig in the matrix and hardening of the precipitate and the effect depends strongly on the (Vf) of the precipitate. Beardmore, Davies and Johnson (68) showed this in a study on alloys with varying volume fractions. As the volume fraction of precipitate was increased the peak in the flow stress curve became sharper and appeared at a higher temperature. A study of MAR-M200, showed essentially constant yield stress up to about 760°C (69). Similar results were reported by Davies and Johnson (46) for MAR-M246 (Fig. 5). The drop at approximately 760°C corresponds to the temperature of peak strength for

pure γ'. Some data is available for MAR-M246 and MAR-M246 + Hf (22) which indicates a strength minimum at about 500°C (Table 3).

Copley and Kear (70) developed a theory for precipitation hardening in superalloys alloys. Their model was developed by considering velocities of dislocation pairs which were controlled by the force on the dislocation lines caused by APB. After making some assumptions, they arrived at the following equation for the critical resolved shear stress (CRSS) of the alloy:

$$\tau_c = \frac{\gamma}{2b} - \frac{T}{br} + \frac{K'}{2}(\tau_m + \tau_p) \qquad (2.14)$$

γ is the APB energy, b is the Burger's vector, r is the particle radius, K' is a constant, and τ_m and τ_p are the CRSS for the matrix and precipitate. T is the line tension. The first term represents the force from APB energy, the second term force due to line tension, and the third term the contribution from the flow stresses of the matrix and precipitate. Note that the contribution of the line tension term is negative because the resistance of the dislocation to bending (looping) will aid in driving the dislocation into the precipitate particle. Copley and Kear explained the drop in strength above the peak temperature by considering the APB energy to decrease above the peak temperature. Later studies (40-45) have shown that the drop

in strength is due to the operation of a different deformation mechanism, cross-slip of dislocations onto cube planes. Note that the particle size is treated as being uniform, but some alloys have varying particle sizes (duplex structure).

Strain rate and temperature have been shown to influence monotonic slip behavior in high Vf alloys. For MAR-M200 (71), strain rates corresponding to tension tests produced deformation by shear by glide of a/2 <110> dislocations, while lower strain rates, corresponding to creep, produced deformation in the primary creep range by intrinsic/extrinsic stacking faults with a Burgers vector of a<112>. The temperature of this study was 760°C. The effect of temperature was further clarified in other work (72-74) at 760°C and 857°C. Most of this testing was for orientations near [001], and microstructural examination was done on failed specimens. At 760°C an incubation period before creep began was seen. The deformation mechanism system during primary creep was observed to be precipate shearing by <112> type dislocations, associated with stacking faults. This type of dislocation movement was viscous in character and therefore was not seen at high strain rates (tensile testing). The transition to secondary creep occurred after sufficient dislocation interaction took place and deformation in secondary creep was produced by a/2<110> dislocation pairs. At 857°C no incubation period

was seen and creep in both primary and secondary creep occurred by a/2<110> type dislocation movements.

Creep of γ/γ' alloys is very dependent on Vf of γ'. The maximum creep strength for γ' alloys occurs at about 60 Vf of γ' (28). This is shown in Figure 6. Jackson et. al. (75) conducted a study on creep in directionally solidified MAR-M200 + Hf. By varying heat treatments they produced alloys with varying amounts of fine precipitate (less than 0.5 μm). hey found a strong relationship between Vf fine γ' and stress-rupture life.

Creep of high Vf alloys is orientation dependent. For Mar-M200, the effect of orientation has been shown to vary between 760°C and 857°C (72,72). This was due to primary creep occurring by precipitate shearing by a/3<112> dislocations at 760°C but by a/2<110> dislocations at 857°C. At the lower temperature crystals near [001] but on the [001] [111] boundary required larger rotations to produce intersecting slip and secondary creep, resulting in high steady-state creep rates. Crystals near [001] but on the [001] [011] boundary were already oriented for duplex slip, and showed small primary creep strains and low steady-state creep rates. At 857°C the opposite behavior was seen: crystals along the [001] [111] boundary were more creep resistant than crystals along the [001] [011] boundary. MacKay and Maier (76) have reported similar results for the dependence of creep on orientation in

another high Vf alloy, MAR-M247, tested at 774°C. They explained the effects of orientation on creep life were due to lattice rotations, as in MAR-M200. An important point is that these studies on the orientation dependence of creep were made using constant load. The crystals which required large deformations before reaching steady-state creep had undergone larger reductions in area, and thus were exposed to higher effective stresses. Constant stress tests would be an appealing way to clarify these results.

Fatigue Deformation in γ/γ' Alloys

Fatigue refers to the failure of a part under conditions of cyclic loading. Fatigue life is of critical importance in turbine components. In general, fatigue life is reduced with increased temperature and generally reduced by increased levels of stress and strain. However, in high Vf γ' Ni-base alloys, a ductility minimum and therefore reduced fatigue life are usually seen at some intermediate temperature. It is important to remember that each alloy system may have unique fatigue behavior and though comparisons can be made between alloys, generalizations are dangerous and definite understanding can best be gained through direct experimental evidence.

Slip Mode

Perhaps the most basic way of understanding fatigue on the microstructural level is by slip character. Slip

character refers to the way in which dislocations move through the material, and is classified as either planar or wavy.

For planar slip, dislocations move in planar arrays. Planar slip is also referred to as heterogeneous slip because slip is concentrated in planar zones within the material. Planar slip is encouraged by ordering, coherent precipitates, low temperatures, small strains, and low SFE (2).

Wavy slip occurs when deformation is spread throughout the material, and is also called homogeneous slip. Wavy slip is promoted by high SFE, incoherent precipitates, large strains, and high temperatures (2).

Crack Initiation and Propagation

Fatigue cracking is considered to be a two stage process: crack initiation and crack propagation. Cracking occurs either intergranularly or transgranularly, with intergranular cracking occurring at a faster rate (2).

Transgranular cracking occurs in two modes. Stage I or "crystallographic" cracking occurs when the crack follows wwell-defined slip planes. Stage I fracture in a Ni-base superalloy on {111} planes along <110> directions has been documented (77). Stage I cracking is favored by conditions of planar slip, low temperatures and high frequencies. Stage II cracking is non-crystallographic and tends to occur normal to the stress axis; it is favored by wavy slip

conditions, high temperatures and low frequencies. A transition between Stage I and Stage II mode has been observed by Gell and Leverant (78) for MAR-M200. Single crystals were tested over ranges of temperature and frequency, and detailed fractography was done on the samples. At low temperatures and high strain rates, Stage I {111} fracture occurred, while at high temperatures and low strain rates, Stage II fracture occurred. These authors found that for a given temperature a frequency range existed where a transition in cracking mode occurred. Duquette and Gell (79) found that for a fixed strain rate a transition temperature existed - they observed Stage I fracture at 760°C and Stage II fracture at 927°C. Similar results were reported by Milligan, Jayaraman, and Bill (80) for MAR-M200.

A transition in failure behavior with temperature was seen in IN-617, a solid solution alloy (81). At 760°C intragranular slip and crystallographic failure occurred. At 871°C, grain boundary sliding and oxide-induced non-crystallographic failure was seen.

Strain Rate Effects on Life

The effects of strain rate and frequency of cycling have already been shown to be important in crack behavior. The effect is more pronounced at higher temperatures, above about 0.4 Tm (2). High enough strain rate or cyclic frequency can produce planar slip even at high temperatures by reducing time available for creep.

It has been generalized that as frequency is lowered, the life (number of cycles to failure, Nf) is lowered (1). However, this is a broad statement and the exact behavior will depend on the particular material. For MAR-M200 the expected trend, lowered life with lowered frequency, was seen for 927°C. For temperatures of 843°C and below, an optimum frequency occurred to maximize life (78). Any increase in frequency above the optimum lead to reduced lives. This was attributed to intense planar slip at the higher frequencies. Increases with life with decreasing frequency have been seen in Rene 77 (82) and Rene 80 (83,83), when the life was represented on the basis of plastic strain. Coffin (84) interpreted the reduction in life for Rene 80 to the increased time available for environmentally produced cracking at lower frequencies, for a given number of cycles. Antolovich et. al. (83,85) determined the life to be a trade-off between structural coarsenig and oxidation failure in Rene 77 and 80.

Organ and Gell (86) found that for U700 at 760°C a peak occurred in the life versus frequency curve. The frequencies in this test ranged from 2 to 60000 cycles/min (cpm), and the peak occurred at 600 cpm. The lives were in the hig cycle fatigue range. The increase in life between 2 and 600 cpm was attributed to a reduction in creep and oxidation effects, and the decrease in life above 600 cpm was attributed to increasing slip heterogeneity. This agrees well with the results reported for MAR-M200 (78).

Precipitate Effects

In γ'-strengthened alloys the fatigue behavior is determined by the interactions between strain rate and amplitude, temperature, and the nature of the precipitate. The misfit, the APB energy, the particle size, morphology, and Vf (all discussed in the section on Strengthening Mechanism) are all important factors. Particle shearing is favored by low APB energy, low misfit, and low Vf (48), and small γ' particle size (87). All of these conditions favor planar slip. Orowan looping is favored by high APB energy, high misfit, and high γ' Vf (48), and large γ' particle size (87). Orowan looping leads to slip homogenization.

The stability of the precipitate is important in high temperature LCF. As reviewed by Antolovich and Jayaraman (48), it depends on misfit and temperature. These authors discussed results of studies of Rene 77, Rene 80, Nimonic 90, and Waspaloy. In alloys where the misfit is large (Rene alloys), γ' coarsening was prevalent. The LCF life decreased with temperature to a minimum at about 760^{o}C, and then increased with temperature. The life reduction was found to be due to surface contamination from oxidation, while the coarsenig wa beneficial. In the low misfit alloys (Waspaloy and Nimonic 90), the γ' was stable. Twinning and carbide precipitation were observed. Carbide precipitation led to low ductility and to sites susceptible to rapid environmental attack.

Cyclic Stress and Strain Response

For precipitate shearing systems, the fatigue behavior at lower temperatures is characterized by initial hardening followed by softening (5). The initial hardening occurs in the matrix. Eventually the dislocation density builds up to a point that the stress is sufficient to cause precipitate shearing to occur. As the precipitates are sheared they become weaker and weaker. The stress range is reduced, which is beneficial to fatigue life. For precipitate looping systems, the dislocations bypass the precipitates, and cyclic hardening is observed.

In a study of LCF behavior of Waspaloy at room temperature using plastic strain control (88), the cumulative glide behavior was found to be a function of γ' size. For small (80 Å) precipitates, hardening to a maximum followed by softening was observed, and particle shearing occurred. For larger (900 Å) precipitates, the stress range increased up to a stable value, and inhomogeneous deformation was observed.

Another study of LCF behavior of Waspaloy at room temperature and at higher temperatures (87) was performed using two heat treatments for different microstructures - fine grained and large precipitates (FG-LP) and coarse grained and small precipitates (CG-LP). At room temperature, CG-FP material hardened to a maximum, then softened, while FG-LP material hardened to saturation. The

FG-LP material hardened at 500°C, consistent with looping, and softened at higher temperatures due to coarsening. The CG-FP material softened significantly at 700°C and 800°C, due to coarsening, but unexpectedly hardened continuously at 500°C. Metallography showed this was a result of carbon atmospheres restricting dislocation movement.

For UDIMET 700 during LCF testing (89), initial hardening, followed by softening occurred at room temperature and 99°C (210F). Between 204°C and 538°C hardening took place throughout the test. Above 649°C, hardening to a maximum followed by softenig occurred.

Some results concerning cyclic stress behavior of MAR-M200 tested using strain-controlled zero-tension-zero testing have been reported (49,50). At room temperature (49), for small strain ranges below 1.4% total strain, the stress range remained constant throughout the fatigue test. The hysteresis loop closed within a few cycles and reamined closed until failure. For total strain ranges of 1.6 and 1.8 percent, the loop width first decreased and then increased, and the stress range reached a maximum and then decreased throughout the test. This was due to initial dislocation buildup in the matrix, with precipitate shearing and subsequent softening once a critical stress was reached at the precipitate-matrix interfaces. For elevated temperatures (50), at both 760°C and 927°C, the stress range remained constant. The hysteresis loops closed after a few

cycles at 760°C but remained opened at 927°C. At 927°C, the stress dropped as a result of precipitate coarsening.

Environmental Effects

As is the case for all other variables in fatigue, the effect of vacuum versus air environment varies depending upon the exact conditions. The effect of environment is concentrated at microstructural defects, especially grain boundaries. Grain boundaries provide a preferential site for oxidation because they are regions of high mismatch and defect concentration and provide an easy path for diffusion, and they are rich in the oxidisable elements Al, Ti, and Cr in the form of γ', MC, and $M_{23}C_6$ (90).

It would seem that an air environment would be detrimental to life compared to an inert gas environment or a vacuum. This was observed for Rene 95, where creep crack growth rates in air were up to 1000 times faster than in argon (91). However, shorter lives in vacuum compared to air have been observed in some cases. Fatigue life for MAR-M200 single crystals at 927°C was shorter in a vacuum, and lives between 427 to 760°C were unaffected by environment (79). The frequency was 5 cycles/second. At 927°C, cracks initiated at the surface in both air and vacuum, and the longer lives in air were thought to be due to beneficial crack blunting by oxides. At the lower temperatures in air, cracks reportedly initiated in the interior regions. Note that this material had no grain boundaries which are

preferential sites for environmental attack. In U-700 (92) at 760°C the exact nature of the grain boundaries was found to influence the effect of environment. In specimens aged to precipitate carbides at the grain boundaries, creep rates in air were lower than in vacuum. In specimens with grain boundaries without carbides, the creep rate in air was higher than in vacuum. The grain size did not have a strong observed effect.

Directional Solidification

Production of Directionally Solidified Castings

Much of the early work on DS turbine blades was done by Pratt and Whitney (93). The chief benefit of DS is the elimination of grain boundaries transverse to the stress axis. This is done by producing columnar grains in the casting. Columnar grains are formed by creating a unidirectional heat flow so that the solid-liquid interface moves in one direction, and not allowing solidification to occur ahead of the interface. This is achieved using a special mold and casting technique, with one end of the mold chilled. In early attempts the temperature gradient control was achieved by using resistance heating. More recently a withdrawal process was used where the castings were removed from a furnace gradually. The latest techniques involve an exothermic reaction to provide the heat necessary for the steep temperature gradient (94-96).

Because of the temperature gradient, growth of columnar grains with preferred orientation is promoted. In nickel-base superalloys the preferred orientation is [001]. Grains with this orientation grow more rapidly and crowd out other grains. The final result is a casting consisting of parallel columnar grains with no transverse grain boundaries.

The technique for XL materials is similar, except a mold with right angle bends or a helix shape in the ingate section is used. The bends serve as a selector. The grain which is favorably orientated for growth in perpendicular directions blocks out all others at the bends and grows into the mold cavity. XL crystal alloys thus have no grain boundaries and might be expected to have superior properties. However, DS components are normally used because they are less expensive due to higher production yields and still have considerably improved properties compared to conventionally cast parts. In comparisons between XL and DS MAR-M200, little difference in fatigue life was seen between the two cast forms (49). Thus DS materials are a cost effective compromise for certain applications.

DS castability is influenced by alloy chemistry. Kotval and coworkers (19) suggested that hafnium additions would be beneficial to DS production of castings. Hf-modified alloys have in fact been used for DS parts, as Hf

apparently combats grain boundary cracking during casting (96). However, levels above about 2% lead to inclusions. The other grain boundary elements (Zr, B, and C) can cause grain boundary cracking when present in high levels.

The as cast structure of DS alloys such as MAR-M200, MAR-M246, and MAR-M247 is highly dendritic and consists of coarse γ' in interdendritic regions (slower cooling rates) with finer γ' in the dendrite cores (higher cooling rates). Eutectic γ/γ' constituent and carbides are present, mainly at grain boundaries but also along dendrite boundaries. Heat treatments are performed to refine this structure by dissolving the as cast γ', called solutionizing, followed by quenching to prevent γ' precipitation. Finally aging is done to precipitate fine γ' evenly throughout the material. Coatings can be applied before the aging treatment (95). As discussed before, it is desirable to solutionize at the highest possible temperature, limited only by incipient melting, to dissolve the maximum amount of as cast γ'. Solutionizing temperatures are commonly about 1200-1350^{o}C for two hours. Aging temperatures are in the 800-1000^{o}C range for 20-24 hours. Combinations of temperatures can be used.

Achieving a proper quench is important to prevent coarse γ' from reforming in the material when cooling from the solutionizing temperature. In the work reported by

Strangman et. al. (94) some material received a delayed argon quench. This material displayed lower tensile yield and ultimate strengths and lower stress rupture life.

Influence of Directional Solidification on Properties

The improvements in properties in a DS casting compared to a CC casting are due to the elimination of transverse grain boundaries.

Flow stress of the DS material is only slightly improved over CC material, but ductility is substantially improved. This was observed in MAR-M200 (93,69). In both of these studies the 0.2% yield stress vs. temperature dependence for the two conditions was essentially the same, but the DS material displayed tensile elongations of 8-10% compared to 4-5% for the CC material. However, the DS material had a more pronounced ductility minimum at 760^{o}C. See Figure 7.

Creep performance is substantially improved through directional solidification. This has been reported for MAR-M246 (97-99), IN-100 and 713C (97), for MAR-M200 (98,93), and for Rene 120 (100). Rupture lives are improved, the stress to cause failure in a set time is increased, and creep ductility is improved. For MAR-M246, Tilly and Harrison (99) observed tensile minimum creep rates that were similar for both CC and DS material, but the tertiary creep stage was reached more rapidly in the CC material. A comparison of the tensile creep rates for CC and DS material

is shown in Figure 8. These authors found little improvement in compressive creep for DS material. A Larson-Miller curve for MAR-M246 (98) is shown in Figure 9, showing a great improvement due to directional solidification.

One characteristic of creep behavior for some alloys in the DS form is a large primary creep strain, in certain ranges of stress and temperature. For MAR-M200, large primary creep strains have been seen at hig stresses around 760°C (101). Primary creep has been shown to occur in this temperature range in this alloy by the viscous glide of a<112> dislocations (72), in a very planar mode of deformation. In CC material, long range planar movement of these dislocations is prevented by grain boundaries, but in the DS material there are no transverse grain boundaries and the dislocations can glide longer distances before encountering strain fields due to grain boundaries. Secondary creep occurs only after sufficient dislocation-dislocation interactions have occurred and a steady-state substructure has formed. The large primary creep strains were not observed at higher temperatures, because the deformation mode is more homogeneous (73), leading to a faster transition to secondary creep. A similar dependence of primary creep strain on the deformation mode has been observed in another study (102). As long as deformation was planar (particle shearing), large primary creep strains were observed. In this study, primary creep strain was also

related to lattice mismatch. Two alloys, one of low mismatch and one of high mismatch, were tested in creep in CC and DS forms. At 740°C, the high mismatch alloy showed a small primary creep strain in both forms. The low mismatch alloy showed a large primary creep strain in DS form but a low primary creep strain in CC form. The many interfacial dislocations and the resistance to precipitate shearing in the high misfit alloy led to rapid strain hardening, while in the low misfit alloy deformation was heterogeneous. At higher temperatures, 850°C and 900°C, the observed primary creep strains were low in all the alloys. This was caused by a more homogeneous and thermally activated deformation mode and more rapid strain hardening.

The benefits of DS material in creep are related to orientation of the boundaries. As the orientation changes fro longitudinal (0 degrees) to transverse (boundaries 90 degrees from the stress axis), the advantage of the DS material diminshes. For DS IN-738 (103), longitudinal orientations showed the longest rupture lives at high temperatures and low stresses. However, longitudinal orientations showed short lives at low temperatures and high stresses, and had lowest creep strength. Longitudinal orientations were also found to be superior for DS DK5, an alloy similar to Rene 80, but with higher Al and lower Ti (104).

In fatigue, DS has been shown to lead to improved

properties. Tilly and Harrison (99) found that for a 3 cycles/hour, triangular wave, tension-zero-tension test cycle, DS material in longitudinal orientation showed an approximately 3-fold increase in life. For alloy DK5, DS material was found to have lower crack growth rates (da/dN) at 700°C and 950°C (104).

As in creep, the fatigue properties of a DS part depend on orientation. For alloy DK5, at 70°C, crack growth rates (da/dN) were found to depend on orientation as well as ΔK (104). Longitudinal orientations showed lower da/dN values than transverse orientations at all ranges. 45° orientations showed highest da/dN values for low ΔK and lowest da/dN values at the high ΔK range.

Wright and Anderson (100) studied the effect of orientation on fatigue in DS Rene 150 in high cycle fatigue and DS Rene 120 in low cycle fatigue. They found little orientation dependence in the high cycle fatigue experiments but a strong orientation dependence in the low cycle fatigue testing. Longitudinal orientations showed longest lives, 45° orientations showed shortest lives, and transverse orientations gave intermediate lives (Fig. 10). These results were interpreted as being due to the anisotropy of the elastic modulus. The effect of the modulus differences was to change the stress range for the strain controlled testing, with higher stress ranges causing reduced lives. It was suggested that maximum tensile stress was the main

factor in determining fatigue life for these alloys, rather than plastic strain. The influence of modulus extended to hold time tests and combined thermal and mechanical cycling tests, resulting in lives for each orientation that were inversely proportional to the modulus.

Raquet, Antolovich, and Payne (105) examined the LCF behavior of DS Rene 80 and Hf-modified DS Rene 80, over a temperature range of 24-871^{o}C. Testing was done in the plastic strain control mode, and adjustments were made throughout the tests to keep the plastic strain range approximately constant. All samples showed a life minimum in the range of 550-760^{o}C. Life was greatest for the longitudinal orientations, shorter for the 45 degree orientations, and shortest for transverse orientations. Hf additions were found to change the carbide morphology from script to discrete particles, but Hf increased the strength of the alloy and in the strain controlled testing this corresponded to increased cyclic stresses and shorter lives. The Hf-containing alloy displayed more crystallographic fracture character than the standard composition. At 25^{o}C, slip was planar in character, and precipitate shearing occurred. At 760^{o}C slip was less planar. Dislocations were present at interfaces and were apparently unable to penetrate the γ'. Dislocation loops and tangles, and pairs of dislocations around small γ' particles, were also seen. At 871^{o}C the γ' had

coarsened significantly. Evidence of shearing was not seen and dislocation loops were observed in the γ/γ' interface regions.

An additional benefit of directional solidification is resistance to thermal stress fatigue. A study of thermal stress fatigue for twenty-six superalloys (106) found that DS materials were far more resistant to thermal stress failure than any of the CC or wrought materials tested. This was attributed to the lower elastic modulus and absence of transverse grain boundaries in the [001] direction.

Summary of Past Investigations on MAR-M246

Some results of studies on MAR-M246 have been mentioned earlier in the literature review. This section is meant to summarize available information on this alloy. MAR-M246 was developed by the Martin Metals Company. The chief difference between MAR-M246 and MAR-M200 is the addition of Ta in MAR-M246 in place of Nb to improve high temperature grain boundary strength, because tantalum carbide is thermodynamically more stable than niobium caribde (22). The alloy in the present investigation contains a Hafnium addition of 2.0% for ductility improvements (Tables 2 and 3). The microstructure of this alloy has been characterized in several investigations (107,108). The alloy contains a volume fraction of 60% γ' and an unconstrained lattice mismatch of 0.52% based

on measurements of extracted γ' by Bowman (107). The γ' cubes have sharp corners as a result. The alloy contains $M_{23}C_6$ carbides and MC carbides. Collins (16) found that after 5000 hour exposures at 927°C, the MC carbides decomposed to M_6C. Restall (109) reported precipitation of M_6C after only 200 hours at 1050°C. Johnston and Parr (108) found that faster cooling rates led to narrow dendrite spacing and increased tendency for the script MC carbide morphology. The carbide morphology is influenced by the Hf in the alloy: at fast cooling rates, the low solubility of Hf in Ni causes the Hf to be rejected, ultimately forming the script MC carbides. Some incipient melting was also found which was considered to be a result of regions of high hafnium content. Johnston and Parr found that at aging at 871°C and 970°C caused the volume fraction of precipitate to level off at about 60% in approximately 100 hours, but at 871°C the precipitate size was constant, and at 970°C the γ' coarsened.

Tilly and Harrison (99) presented one of the earliest comprehensive studies available in the literature on deformation of MAR-M246. They investigated the static and cyclic creep (low strain rate fatigue) properties of DS, XL, and CC MAR-M246 at 850°C and 900°C. They found that the tensile creep lives of XL and DS material were similar, and were longer than the creep lives of CC material (Fig. 8). In compressive creep, all three forms displayed similar

lives. They concluded the chief benefit of DS material in creep was a delay in the onset of tertiary creep.

Hold time, load controlled fatigue tests were also conducted in this study, with a zero-tension-zero waveform and 6 minute holds at each limit. Anelastic recovery during the off-load period was initially small, but rapidly built up to a steady-state value (dependent on stress) and finally increased prior to failure. Most of the time-dependent damage accumulated in the load holds was thus recovered during off-load period. However, rupture times calculated from summing load periods were approximately equal to tensile creep rupture times. This result leads to the conclusion that oxidation may have been important in light of the elevated temperatures. Unfortunately, no results of microstructural examination were presented.

Triangular zero-tension-zero tests were also conducted at 3 cycles/hour and 300 cycles/hour. For this type of test, the cyclic tests displayed longer lives than similarly stressed static creep tests. Note that in this type of test a major portion of the actual test time is spent at loads well below the maximum tensile level.

Some push-pull tests were done as well, using the rectangular waveform and 6 minute holds and the triangular waveform at 3 cycles/hour. The hold time tests displayed lower lives in terms of stress vs. rupture time. Note that for a given stress, the rectangular waveform includes a

greater amount of time spent at the maximum stress than the triangular waveform test.

Northwood (98) reported a creep results similar to those of Harrison and Tilly: DS and XL material displayed similar creep lives, superior to CC material (Fig. 9). The experimental details of this study were not presented.

Johnston and Parr (108) reported some results of HCF testing of MAR-M246 + Hf in the single crystal form, tested at 843^{o}C at R ratios of 0.4 and 0.8. They found that lives diminished as deviation of the tensile axis from the [001] growth direction increased, with particularly significant decreases in life at deviations above 10 degrees. They stated that the decrease in life was due to increased amounts of lattice rotation necessary to achieve a multiple slip condition, similar to the explanation given by Mackay and Maier (76) for creep in MAR-M247. According to this argument, increased rotation led to an increase in the effective strain.

CHAPTER III

MATERIALS AND PROCEDURE

Material

The alloy used for this investigation was MAR-M246+Hf. The composition is given in Table 1. The material was supplied in the form of machined tensile and smooth-bar low cycle fatigue (LCF) specimens by NASA Lewis Research Center. Specimens were machined from investment castings produced by TRW Aircraft Components Group. All specimens had an [001] longitudinal orientation, with a specified maximum allowable deviation of the columnar grains from the longitudinal axis of 8 degrees. Cooling rates were not available.

The heat treatment performed was as follows: 2 hours in vacuum atmosphere at 1221^{o}C, air cool, followed by 24 hours in air at 871^{o}C. After machining, the specimens were stress relieved for 8 hours at 871^{o}C.

The tensile and LCF specimen dimensions are shown in Figure 11.

Experimental Procedure

Test Matrices

As mentioned in the introduction, the present study is part of an overall program to study the constitutive

behavior of the alloy, in monotonic and cyclic deformation. The variables chosen for the study included temperatures of room temperature, 704°C (1300°F), 927°C (1700°F), and 1093°C (2000°F), two target plastic strain ranges of approximately 0.025% and 0.1%, two strain rates of 50%/minute and 0.5%/minute, and length of test (interrupted and failure tests). In addition, tests were planned for vacuum environment and using off-axis specimens. The final area of the study was to include some thermal-mechanical fatigue (TMF) tests using a bithermal test procedure. The present work has involved completion of all the [001] oriented tests, in air, to failure. The total isothermal test matrices and completed tests are shown in Tables 4 and 5.

Sample Preparation

All specimens were electropolished before testing to reduce surface-related scatter in the results. The details of this procedure are given in Appendix A.

Mechanical Testing

All mechanical testing was conducted in air, using a SATEC Systems computer-controlled servohydraulic testing machine. This machine uses a minicomputer (Digital PDP 11/34) for digital control of the hydraulic ram. A separate microcomputer is used for test set-up and data acquisition.

The elevated temperature testing made a specially modified extensometer necessary. Details of the

construction of the extensometer are given in Appendix B.

Temperature control was achieved through induction heating, using a Lepel 2.5KW generator and induction coils formed from copper tubing. Calibration of the sample temperature was carefully performed as described in Appendix B to maintain a temperature gradient of +/- 2°C over the gauge length of the specimen.

Tensile Testing. Tests were conducted at 20°C at a strain rate of 50%/minute and at 704°C, 927°C, and 1093°C at 50%/minute and 0.5%/minute. Tensile tests were performed using strain control to a point past yielding (approximately 1.0% strain) and stroke control for the remainder of the test at a displacement rate chosen to provide approximately the desired strain rate. The 704°C, 50%/minute test could not be used for analysis because of extensometer slippage which caused a loss of machine control and loss of the test. After this experience, the tips of the alumina rods were ground frequently to ensure a sharp point. Because insufficient samples were available to repeat the test, an interrupted test (originally planned for a later portion of the overall test program) was run. This test was performed using a feature of the SATEC machine called combinatorial feedback, which allowed a user-defined control signal to be used. An equation was programmed into the machine which measured plastic strain, and the plastic strain was used as the control signal to stop deformation of the sample and

return to zero load, as described in Appendix B. In all tests to failure, the extensometer was removed before failure to prevent its being damaged upon specimen separation.

Low Cycle Fatigue Testing. LCF tests were performed over the same temperatures and strain rates as the tension tests using total axial strain control and a fully reversed triangle waveform. The total strain range was chosen to produce a desired inelastic strain range and was held constant throughout the test. Tests were run at constant strain rates of 50%/minute and 0.5%/minute as described in Appendix B.

The minimum and maximum stress vs. cycle and periodic hysteresis loops were monitored using both conventional recording instruments and the data acquisition capability of the microcomputer. Initiation was determined using the double secant method. In this method, the load vs. cycle plots were examined, and initiation was determined by the intersection of two lines: one drawn through the maximum stress points in the steady-state region of the test, and one drawn through the maximum stress points in the final load drop region.

Sample Sectioning and Microstructural Examination

The as-received material was characterized using metallography and x-ray diffraction. A small block (0.5 cm x 2 cm x 3 cm) was available for this purpose. Slices 0.2

mm thick parallel to the columnar grains (longitudinal) and perpendicular to the columnar grains (transverse) were used for TEM foil preparation as described below. Larger samples were sectioned and mounted for optical examination. Lattice parameter and mismatch determinations were made using a Phillips diffractometer and copper Kα radiation.

Tested samples were examined optically. On some specimens, cellulose acetate replicas were taken of the specimen surface. After examination the samples were sectioned. Sectioning details are given in Appendix A. Fracture surfaces were examined using the SEM, longitudinal sections through the specimens were examined optically to study crack paths, and deformation substructures were studied using the TEM. Metallography and foil preparation methods are given in Appendix A.

To determine if deformation would influence microstructural changes at elevated temperatures, samples were taken from the threaded ends (undeformed) of the incorrectly tested 704°C, 50%/minute tensile specimen. These samples were placed in a furnace for 49 hours, one at 927°C and one at 1093°C. The end sections of the sample had not been subjected to deformation or elevated temperatures. Slices were cut from these samples after exposure for TEM examination to compare the coarsening in these undeformed samples with failed specimens.

CHAPTER IV

RESULTS AND DISCUSSION

Initial Material Characterization

The microstructure of the untested specimens is shown in Figures 12-15. The structure consisted of columnar grains approximately parallel to [001]. The grain diameters varied but were on the order of 100 microns. The grain boundaries were serrated and irregular, and some transverse boundaries and tapered grains were observed [Fig. 12a). Each grain possessed a dendritic structure, with finer γ' near the dendrite cores and coarser γ' near the interdendritic regions. This is a consequence of the faster cooling rate in the dendrite cores. The dendrite cores are reportedly rich in W and Co, and the interdendritic regions are rich in Cr, Ti, Al and C (18). MC and minor amounts of $M_{23}C_6$ carbides and $\gamma - \gamma'$ eutectic pools were present at grain boundaries and interdendritic boundaries. The MC carbides in the alloy displayed a slight script morphology, despite the Hf content of the alloy. In an alloys containing no Hf, MC carbides tend to form late in the solution process in the interdendritic regions, leading to the script morphology. Hf tends to minimize the formation of script carbides, because its strong affinity to carbon

allows the MC carbides to form earlier in the solidification sequence with a more blocky morphology (20). At higher cooling rates, however, the poor solubility of Hf in Ni causes it to be rejected during solidification, ahead of the freezing interface, leading to the script carbide morphology. Some scattered micropores were observed, but the low level of porosity was not considered to be significant, as subsequent mechanical testing (described in the following sections) revealed no initiation or failure due to micropores.

The γ' structure is shown in Figures 14-15. The volume fraction was measured by Bowman to be 60% using phase extraction techniques (107). The lattice parameters of the precipitate and matrix were determined from in situ measurements to be 3.581 A and 3.563 A respectively. This results in an in situ lattice mismatch of 0.50%. Using equation 1.2, a value of ν of 0.391 as reported for MAR-M200 (117), and $k = 1.0$, the unconstrained mismatch was calculated to be 0.65%. This value is higher than the value of 0.52% reported by Bowman (107). The difference may be due to variation due to dendritic segregation. The accuracy of the in situ determination of mismatch is also limited by the resolution of the recording instrument and other errors as described in detail by Bowman (107). The antiphase boundary energy (APBE) of the γ' was measured to be 0.21 J/m^2 (107). Note that some stacking faults are present in

the starting microstructure. TEM micrographs of a eutectic γ/γ' region are shown in Figure 15. A diffraction spot corresponding to the carbides was used to form the image shown in Fib. 15b.

Tensile Behavior

Strain Hardening Behavior

The stress strain curves are shown in Figure 16, and the tensile properties are given in Table 6. Note that in Fig. 16 the upper endpoints of the curves do not correspond to specimen failure because the extensometer was removed before failure to prevent damage to it. The shape of the stress strain curves indicated a change in strain hardening behavior. At room temperature and 704°C, 50%/min. strain rate, the stress strain curves were approximately horizontal after yielding. For all other test conditions, stress continued to rise with increasing strain. The monotonic strain hardening exponents were calculated, and the values for room temperature and 704°C, 50%/min. tests were lower than the other values. The low n values are indicative of more heterogeneous deformation (37), and TEM studies discussed later confirmed this result. The 927°C, 0.5%/min. n value was higher than the 927°C, 50%/min. value. This was an indication that at the slower strain rate, more non-planar, intersecting slip was occuring due to thermal activation, leading to more strain hardenig. At 1093°C, the

0.5%/min. n value was lower than the 50%/min. value. A reasonable explanation for this is that the temperature was sufficient to allow recovery and precipitate coarsening during the slow strain rate test, reducing the amount of hardening, and similar to the 1093°C fatigue tests. The slow strain rate test took approximately 25 minutes to complete. TEM studies, discussed in subsequent paragraphs, supported these conclusions.

Mechanical Properties

The 0.2% yield stress result are shown in Figure 17. The yield stresses at 20°C and 704°C were similar. Above 704°C the strength decreased with increasing temperature, and the material displayed a ductility minimum at 704°C as measured by reduction of area values. These results are typical for high volume fraction nickel-base superalloys. Figure 5 shows a yield stress vs. temperature curve for conventionally cast MAR-M246 (46), which displayed essentially constant yield strength up to about 750°C. Figure 7 shows a stress vs. temperature curve for DS MAR-M200 (69), which displayed a peak in yield stress at about 760°C, and a pronounced ductilty minimum. The 704°C samples failed outside the gauge section, near the specimen shoulders. This result indicates a strength minimum below this temperature. Conventionally cast MAR-M246+Hf, aged for 16 hours at 870°C after casting, showed a minimum in 0.1% yield strength at 500°C (22) (Table 3). The heat treatment

given the material in the present investigation has resulted in higher strength and lower ductility values than reported for the conventionally cast material.

The effect of strain rate on strength was dependent on the temperature. At 704°C, the lower strain rate changed the degree of strain hardening and the shape of the stress strain curve (as previously discussed), and as a result, the difference in yield strength depended on how yield strengths were defined. Yield strengths were approximately equivalent between the two strain rates (Table 6). At 927°C and 1093°C all yield stress values were lower at the slower strain rate. The strain rate sensitivity of strength is indicative of the increasingly important role of thermal activation in deformation. Single crystal MAR-M200 displayed a similar dependence of strength on strain rate (71), with strain rate independent flow stress at 760°C over the range of strain rates of 0.1%/minute to 100%/minute, increasing flow stress with increasing strain rate up to 100%/minute at 843°C, and continuously increasing flow stress with increasing strain rate at 927°C.

The role of thermal activation in yielding in nickel-base superalloys has been discussed in detail by Milligan and Antolovich (110). They showed that yielding behavior was a function of strain rate and level, and that a plot of $\ln \sigma_{ys}/E$ vs. the reciprocal of absolute temperature could be used to arrive at a value of the activation energy for

yielding, through an analysis based on the simple creep equation:

$$\sigma/E = A \exp (Q^*/RT) \qquad (4.1)$$

σ is the applied stress, E is the modulus, A is a material constant, T is the temperature, and R is the gas constant. Q^* represents an apparent activation energy. The slope of the ln σ/E vs. $1/T$ curve is used to calculate Q^*.

Such a plot is given for the present results in Figure 18. The calculated values of Q^* above 704°C are given in Table 10. Examination of these values reveals some discrepancies from the results of Milligan and Antolovich (110). The slope of the plot between 20°C and 704°C would be expected to be horizontal if there is little contribution from thermal activation. Instead, a slightly positive slope was observed. At higher temperatures, the slope (and Q^*) increases sharply. The values for the two strain rates should be close at very high temperatures, where thermal activation dominates. The observed values were close but not identical. The final discrepancy is that between 704°C and 927°C, the Q^* value for the slow strain rate was lower than for the fast strain rate. This is oppcsite to what would be expected: at lower temperatures, thermal activation manifests itself first at slow strain rates. It is felt that these variations are due to three factors.

First, the low number of tests and temperatures studied limited the accuracy of the slope determination. Also, some scatter was expected due to variations between the grain structures of the specimens. Finally, although the temperature around 704°C represents a transition in yielding behavior from athermal slip to thermally activated climb processes and the functional form of the relationship is probably not linear, a linear relationship was used in the Q^* calculation. Nevertheless, the data does show trends supporting the results of Milligan and Antolovich (110). In their study, interrupted tests were carried out on PWA 1480 over a wide range of temperatures at the same strain rates as in the present study, and TEM analysis showed that the change in slope of the $\ln \sigma_{ys}/E$ vs. $1/T$ curve occurred because of a change in the yield process: from precipitate shearing at lower temperatures and faster strain rates, to dislocation bypass at higher temperatures and slower strain rates. Dislocation bypass involves climb and therefore is more dependent on thermal activation, and as a result showed a higher activation energy. They went on to show that the value of Q^*, the apparent activation energy, could be related to the activation energy for creep, Q, based upon the fundamental creep equation:

$$\dot{\varepsilon}_s = A \left(\frac{\sigma}{E}\right)^n \exp\left(Q/RT\right) \qquad (4.2)$$

$\dot{\varepsilon}_s$ is the steady state creep rate, A is a constant, and n is the creep exponent, obtained from $d\ln \dot{\varepsilon}/d\ln \sigma$. The other symbols have the usual meanings. Assuming that the yielding process in tension can be described by the value of Q, and that $\dot{\varepsilon}_s$ is constant in yielding, σ_{ys} can be substituted for σ:

$$\ln (\sigma/E) = (Q/Rn)\ 1/T + (\ln \dot{\varepsilon}_s/A)/n \qquad (4.3)$$

Q can be calculated from Q^*: b

$$Q = n\ Q^* \qquad (4.4)$$

Creep data for DS MAR-M246, containing no Hafnium, from Reference 99 was used to obtain a value of n for MAR-M246 of 9.75. The resulting values of Q are summarized in Table 10. Although the tests run in this study were tested to failure, and the high dislocation density of the failure tests prevented confirmation of the processes occurring at yielding, the results of this study and the activation energy analysis showed the same trends as seen for PWA 1480 (110). The values of Q obtained are within the range of values reported in that study for steady state creep.

The modulus vs. temperature curve is shown in Fig. 19. For each temperature, the average modulus of all tests (including the LCF tests discussed in the next sub-section)

was plotted. In DS materials, the number and orientations of the grains is subject to wide variation from sample to sample. This explains the scatter seen in the modulus data. The effect of modulus variations due to differences ingrain cross-sections has been described in detail by Raquet, Antolovich, and Payne (105). These authors showed that apparent wide scatter in LCF results could be rationalized due to grain variations between samples.

Optical Metallography

Optical examination along planes perpendicular to the fracture surface revealed a trend toward increasing void formation at eutectic regions with increasing temperature and decreasing strain rate (Fig. 20). At 1093°C, tests at both strain rates showed void formation, while at 927°C, void formation was only evident in the slow strain rate test. The formation of such voids indicates that significant self diffusion is occurring and therefore significant climb is possible. Thermally activated climb was proposed as the rate controlling mechanism in the thermal activation analysis of Milligan and Antolovich (110).

Fracture Surface Character

Tensile fracture surfaces were macroscopically flat (Fig. 21). At room temperature the tensile fracture occurred by dimple rupture, but with very brittle fracture associated with script carbides in the interdendritic

regions (Fig. 21a). At elevated temperatures the overall fracture surfaces were more ductile in appearance (Fig. 21b), consistent with an increase in reduction in area from 7.9% at 20°C to over 30% at 1093°C. Note the 704°C fracture surfaces were not examined due to the location of the final specimen failure, in the shoulders of the specimen.

Dislocation Substructures

Examination of the dislocation substructure of the tested specimens was performed using TEM techniques, and the substructure was highly dependent on test condition. At room temperature, the dislocation networks were predominantly planar (Fig. 22). Dislocations were stored on the precipitate-matrix interface, but dislocations were also present within the precipitate and some slip bands were observed. The dislocations on the interfaces show that the penetration of the precipitate is the probable rate controlling step in yielding. This correponds to a heterogeneous, precipitate shearing deformation mode and is consistent with the low strain hardening exponent value, 0.072.

At 704°C, 50%/minute strain rate, the substructure was similar to that observed at room temperature, with precipitate shearing and planar dislocations (Fig. 23a). The overall dislocation density was lower, due to the fact that this specimen was not tested to failure, but only to 0.32% plastic strain. At 704°C, 0.5%/minute strain rate,

the structure was similar to the structure of the fast strain rate test, with precipitate shearing observed (Fig. 23b). The dislocation structure explains the increased strain hardening (n = 0.226) at the slow strain rate at 704°C. The more homogeneous nature of the substructure was indicative of thermally activated deformation, and a lower 0.05% yield strength was observed at the lower strain rate. However, increasing slip homogeneity led to more rapid strain hardening, and the 0.2% yield strengths were very close. This specimen was tested to failure and in the absence of any recovery effects, would be expected to have a higher dislocation density than an interrupted test, limiting the possible comparisons with the 50%/min. interrupted specimens.

At 927°C the dislocation substructures were very homogeneous and wavy in character at both strain rates (Fig. 24), consistent with the high degrees of strain hardening at this temperature. At 0.5%/min. strain rate, few of the dislocations were linear, and the initial formation of dislocation networks on the interfaces was noted (fig. 24b). Because these tests were run to failure, the dislocation density was very high, which led to difficulty in obtaining acceptable TEM thin foils. The dislocation structure is obviously a function of the level of strain, and the structures shown are not necessarily descriptive of dislocation behavior during initial yielding. Still, the

homogeneous nature of the substructure indicated that thermally activated dislocation movements were occurring at these temperatures, consistent with the lower yield strength with slower strain rates. For single crystal MAR-M200 (71), the strain rate dependence was attributed to a transformation from diffusionless shear of γ' by dislocations at lower temperatures and faster strain rates to diffusion-assisted deformation at the higher temperatures and slower strain rates. The results of Milligan and Antolovich (110) previously discussed and the behavior shown in Figure 18 support the conclusion that thermal activation is important in MAR-M246 as well.

At 1093°C, 50%/min., the dislocation substructure was similar to the structure at 927°C, but with an overall lower dislocation density (Fig. 25a). The dislocations were fairly homogeneously dispersed, corresponding to the high degree of strain hardening (n = .317). At the slow strain rate at 1093°C, the γ' had coarsened significantly (Fig. 25b). The overall dislocation density was much lower, and almost all of the dislocations were stored in the form of interfacial networks. The lower dislocation density is an indication of recovery, and together with the precipitate coarsening, explains the reduced level of strain hardening at the slower strain rate (n = .221).

Fatigue

Life Correlation Results

The LCF test results are summarised in Table 7. The life was correlated with several parameters using linear regression on a log-log basis. The analysis was performed on the 50%/min. data on the limited number of points available: 3 points each for 704°C and 1093°C, and 4 points for 927°C. The data was first fitted to the well-known Coffin-Manson Law (111):

$$\Delta\varepsilon_p = C\ Nf^b \qquad (4.5)$$

$\Delta\varepsilon_p$ is the plastic strain range (usually at half-life), C is a constant, Nf is the number of cycles to failure, and b is the Coffin-Manson exponent. This relationship is shown in Figure 26. Note that in this commonly used analysis, $\Delta\varepsilon_p$ is treated as the dependent variable, even though the life is actually the dependent variable (87). The resulting Coffin-Manson equations were:

$$704°C: \quad \Delta\varepsilon_p = .08\ Nf^{-0.783}$$

$$927°C: \quad \Delta\varepsilon_p = .11\ Nf^{-0.676}$$

$$1093°C: \quad \Delta\varepsilon_p = .80\ Nf^{-0.762}$$

The correlation coefficients were 0.996, 0.986, and 0.999 respectively. Error analysis was not considered meaningful because of the limited number of data points for each test condition.

In all analysis Nf was used rather than Ni, the cycles to initiation. Ni was calculated using the double secant method (Chapter III) from the load vs. cycle records. Following Lerch (118), the crack size corresponding to Ni was calculated to be about 800 microns. Thus the value of Ni represents some amount of propagation.

Life was also plotted and correlated against total strain range (Fig. 27a) and stress range (Fig. 27b). In both of these analyses Nf was again treated as the independent variable for the sake of comparison of correlation with the Coffin-Manson analysis. The resulting correlation coefficient values are given in Table 8. Both approaches give lower correlation values than those for the Coffin-Manson law. It has been shown (112) that LCF life for single crystal 7-14-6 could be correlated with ($\Delta\varepsilon_t E$) or the Neuber parameter (sqrt ($\Delta\varepsilon_T . E . \sigma_{MAX}$)), even for different orientations. The present data were analysed with these parameters and the correlations (Table 8) are higher than those for σ_{MAX} or $\Delta\varepsilon_t$ alone. This confirms that elastic modulus, which is subject to variation in DS materials due to misorientation, is obviously significant in determining

fatigue life in the strain-controlled LCF tests, through its effect on stress. Note that the Coffin-Manson law, based on plastic strain range, gave higher correlation values than any other parameter. This means that to predict fatigue life accurately, the exact mode of damage must be considered.

At 927°C and above, oxidation was found to play a significant effect in determining fatigue life, as discussed in subsequent sections. Antolovich, Baur, and Liu (85) have presented a model for the effect of oxidation on life. The model assumes parabolic oxidation kinetics and relates the depth of oxide spikes to the time of the test. The relative depth, l_i, of an oxide spike, taking the shortest test time (t_o) as unity, is given by:

$$l_i = (t_i/t_o)^{1/2} \qquad (4.6)$$

t is the time to failure of the test. For oxide-induced failure, the maximum stress at initiation was proportional to $l_i^{1/4}$. Figure 28 shows a plot of maximum stress at initiation vs. the relative oxide depth for the present study. Visually, the correlation appears to be best for 1093°C, and the horizontal slope at 704°C implies no dependence of failure on oxidation. Antolovich, Baur, and Liu (85) showed that for fully reversed testing, the life to initiation, Ni, could be predicted by the equation:

$$Ni = C_2 \frac{\nu}{1 + \nu t_h} \exp(-Q/RT)\ \Delta\varepsilon_p^{-8n'} \qquad (4.7)$$

C_2 is constant, ν is the test frequency, t_h is hold time (if any), Q is the activation energy for oxidation, $\Delta\varepsilon_p$ is the plastic strain range, and n' is the cyclic strain hardening exponent. R and T have their usual meanings. The 50%/minute data was fitted to this equation, using the value of Q for oxidation given for Rene 80 (85) of 9.6 kcal/mole. Highest correlations were obtained for the 1093°C data. The ability of this model to predict the data well only at higher temperatures will be discussed in light of failure mechanisms in later sections. Note that 0.5%/min. data was not considered because of limited data and no value for n'.

Effects of Strain Rate on Life

Some of the effects of strain rate on fatigue life can be understood by comparing Figures 26 and 27. At 704°C, the 0.5%/minute strain rate resulted in shorter lives, on the basis of plastic strain range. This was due to the difference in monotonic strain hardening behavior, as predicted by the Ramberg-Osgood relationship:

$$\frac{\varepsilon}{\varepsilon_o} = \frac{\sigma}{\sigma_o} + \alpha \left(\frac{\sigma}{\sigma_o}\right)^N \qquad (4.8)$$

σ_o and ε_o are the yield point stress and strain, α is a constant, and N is the reciprocal of n, the strain hardening exponent. For a given amount of strain the higher degree of strain hardening at the 0.5%/minute strain rate resulted in a higher stress range. On the basis of stress range, the lives were approximately equal between the two strain rates. The importance of stress range on life has been recognized by other investigators (85,100,105). A similar reduction in life with decreasing strain rate was found for cast IN738LC, tested at 850°C (113,114).

At 927°C and 1093°C, the slow strain rate lives were longer on the basis of plastic strain range. This was due to the fact that, for a given number of cycles, increased time was available for softening due to precipitate coarsening. This caused a beneficial reduction in stress, although increased time was available for oxidation. When lives were plotted against stress range (Fig. 27b), the lives were shorter at the slower strain rates. Again, the slow strain rate led to beneficial coarsening, but it increased the susceptibility to oxidation-induced failure by lengthening the actual time of the test.

Cyclic Stress-Strain Behavior

The cyclic stress-strain curves for the 50%/minute tests are shown in Figure 29. The cyclic (n') and monotonic (n) strain hardening exponents are compared in Table 9. The number of LCF tests run at 0.5%/min. was insufficient to

allow computation of the n' values for the slow strain rate. The cyclic values generally follow the monotonic patterns, with a significantly lower value at 704°C. This is again indicative of more heterogeneous deformation at 704°C.

Cumulative Glide Behavior

The LCF tests were conducted using total strain control. In this type of test, the plastic strain range and the stress range change depending on the degree of hardening or softening in the material. A final load drop is usually seen corresponding to macrocrack formation and eventual failure. The cumulative glide curves, plotting stress vs. cycle, are given in Figs. 30. At 20°C the stress range increased to a maximum, followed by a gradual decrease over the remainder of the test. Similar behavior has been observed in MAR-M200 (49) and Waspaloy (87,88) and is consistent with precipitate shearing. At 704°C and 927°C, 50%/minute strain rate, the stress range was essentially constant throughout the test, as observed in zero-tension-zero testing of MAR-M200 (50) at 760°C and 927°C. At 927°C, 0.5%/minute, and at 1093°C, marked softening was observed. Although the decrease might at first seem to be due to particle shearing, TEM studies (which are discussed insubsequent paragraphs) revealed that particle coarsening was taking place with relatively little or no shearing.

The curve for one test at 1093°C (Fig. 30d) indicated

some apparent hardening in the latter part of the test, but this was due to an inadvertant temperature variation (10°C). The behavior of this test has general implications on how carefully LCF testing must be done to achieve meaningful results, especially in terms of temperature control.

Fracture Character

SEM examination of LCF fracture surfaces revealed marked differences dependent on test condition. At room temperature, initiation was due to cracking at carbides in the interdendritic regions, and subsequent formation of slip bands (Fig. 31). Fracture surfaces were perpendicular to the stress axis and fracture was highly crystallographic (Figure 32), indicative of intense planar slip.

At 704°C, 50%/minute, fracture in the propagation region was crystallographic, but less distinctly so than at 20°C, and at 704°C, 0.5%/minute, fracture was even less crystallographic (Fig. 33). At 704°C fracture usually initiated at interdendritic carbides. In one case initiation occurred along a transverse dendrite arm (Fig. 34a). Optical examination revealed that at both 20°C and 704°C cracks followed transgranular paths along interdendritic regions, regions that were expected to be more brittle due to the eutectic and carbides in those regions (Fig. 34b). Only slight deflection was observed at vertical grain boundaries.

At 927°C the fracture character was quite different. The fracture surfaces were still perpendicular to the stress axis. The fracture surfaces did not have the crystallographic character seen at lower temperatures (Fig. 35). As expected the surface was heavily oxidized. Optical microscopy (Fig. 36) confirmed the formation of cracks perpendicular to the stress axis (Stage II) due to oxidation of eutectic constituent in interdendritic regions. The oxidation was more severe at the slow strain rate tests, which caused reductions in lives at 927°C and 1093°C. At 1093°C the initiation region was similar to 927°C: flat and featureless and resulting from Stage II initiation at oxide spikes. However, behind the flat initiation region, the crack changed direction slightly and deviated from a plane normal to the stress axis (Fig. 37a). Secondary cracking and some deflection at grain boundaries was also observed (Fig. 37b). At the slow strain rate, oxidation resulting in precipitate depletion, was severe (Fig. 38). Oxidation was found to cause a reduction in life with decreasing strain rate at 850°C for IN-738LC, with no strain rate effect observed in vacuum (114). Stage II cracking has been observed at elevated temperatures in MAR-M200 by other investigators (50,80). The observed crack behavior paralleled results reported for DS IN-738 (113) in FCP testing. In that study, at room temperature, cracks propagated perpendicular to the stress axis with a

crystallographic character, while at 850°C, more crack deflection occurred. The oxidation observed at 1093°C and 927°C suggests that the oxidation model proposed by Antolovich and coworkers (85) should predict life. For the 50%/min. strain rate data available, this model does indeed predict life well at 1093°C as previously shown (Fig. 28), but does not work as well for 927°C. This may be due in part to the fact that some damage is still occurring by planar slip at 50%/minute at 927°C, discussed in greater detail in the next section.

Dislocation Substructures

The dislocation substructures were examined using TEM. The dislocation substructures, along with the observations concerning fracture character and cumulative glide behavior, show that the LCF behavior of this material is highly dependent on the precipitate/matrix relationship.

At 20°C, there were linear dislocation segments throughout the microstructure with a significant amount of dislocation debris at the precipitate-matrix interface (Fig. 39). The overall dislocation density was quite high. The dislocations were of the type a/2<110> (111). This structure was indicative of heterogeneous, planar slip and precipitate shearing and is consistent with the surface slip lines, the gradual drop in life over the last portion of the test, and the highly crystallographic fracture behavior (Fig. 31). The initial hardening during the test followed

by softening could be explained by hardening in the matrix to a point where a critical stress was reached onthe interfaces and shearing occurred. This explanation has been proposed for Waspaloy (87,88). It should be noted that the TEM substructure was taken from the failed specimen. A worthwhile experiment would be to run an interrupted test, to a point before the maximum stress is reached, and study the deformation substructure. The completion of the present study will involve a complete matrix of interrupted testing.

At 704°C, the overall dislocation density was lower. Dislocations were present on the interface and there was evidence of precipitate shearing (Fig. 40). Most of the dislocations were of type a/2<110> (111). However, some a/2<110> (110) dislocations were found (marked with arrows in Fig. 40). These dislocations were pure edge, and near the precipitate/matrix interfaces, where the strong component of the Burger's vector in the direction of the cube face would serve to accommodate the lattice mismatch. This is a significant result, because pure edge dislocations on (110) in the FCC structure are sessile, and would cause hardening. Note that at 704°C, at both strain rates, the stress range of all tests is stable almost immediately. The stability of the stress range appears to be due to a balance of precipitate shearing, which would eventually soften the material, and strengthening from the immobile dislocations on (110) planes. On the basis of plastic strain range, the

lives at 704°C were much shorter than for other test conditions. This corresponds to the minimum in ductility near this temperature, at the maximum γ' strength. There was little qualitative difference between the substructures between the two strain rates (comparing Figs. 40a and b), with the exception of slightly more wavy dislocations in the 0.5%/min. strain rate tests, especially along the interface regions.

At 927°C, 50%/min., shearing of γ' by a/2 <110> (111) dislocations were seen, but the density of this type of dislocation within the precipitate was very low (Fig. 41a). The presence of this type of damage explains the poorer fit with Equation 4.7 for this temperature, compared to 1093°C. Even though oxidation was observed, some damage was occurring by precipitate shearing, which is not accounted for in the model. The significant structural feature observed at 927°C and above was precipitate coarsening, with formation of hexagonal networks of dislocations at the interfaces. Trace analysis showed that the networks were composed of near-edge a/2 <110> dislocations on (111) planes, and some dislocations were on (110) planes. Similar results have been reported for PWA 1480 by Milligan and Antolovich (110), and near-edge character of the networks has been reported for Rene 80 (83). The edge character of the dislocations aids in accommodating the coherency strain. The interfacial

networks were quite well developed at the slow strain rate, and the coarsening was extensive (Fig. 41b).

At 1093°C, 50%/min., no dislocations were observed to be present in the matrix or precipitate interiors (Fig. 42). All dislocations were stored in arrays on the precipitate-matrix interfaces, with the same character as observed at 927°C. The γ' coarsened significantly, in an irregular manner, even at 50%/minute strain rate. Similar coarsening was observed at 927°C at 0.5%/minute strain rate but was absent at the higer strain rate. The coarsening at 1093°C, 50%/min. and lack of such coarsening at 927°C, 50%/min. may partially explain the lower cyclic strain hardening exponent (n') value compared to the 927°C, 50%/min. value.

The coarsening was especially severe at 1093°C at 0.5%/min. strain rate. This test ran for 149 hours, just under one week. The resulting microstructure is shown in Fig. 43. The precipitate particles were greatly increased in size (Fig. 43a), and no dislocations were present except along precipitate-matrix interfaces. Optical microscopy (Fig. 43b) showed that the carbides were almost all resolutioned.

The coarsening of the γ' at 1093°C and at 927°C, 0.5%/min., is consistent with the observed drop in stress range at these test conditions (Figure 30). This coarsening, with the resultant interfacial network of

dislocations, and the low observed dislocation density in the matrix and precipitate are important in determining fatigue life. First, the low dislocation density indicates that recovery processes can occur easily. Thus, the damage due to dislocations is probably minimal. The interfacial networks are not actually damage, because they serve to accommodated the mismatch. Also, the interfacial networks themselves can accommodate large strains by serving as sources and sinks for dislocations. Dislocations can bow out and back from nodes within the networks. This mechanism, which needs experimental verification, perhaps through in situ tests ina loading stage in a high voltage TEM, would explain the observed increase in fatigue lives onthe basis of plastic strain range at 927°C and 1093°C. The lives at these temperatures were oxidation limited, as predicted by the Antolovich oxidation model (85). Coarsening has been discussed instudies on Rene 80 (83), and it was shown that at 871 and 982°C, life was determined by a balance between beneficial coarsening and detrimental oxidation. Essentially the formation of oxide spikes or regions of higher oxygen content constitute damage to the extent that they nucleate stable cracks. The formation of cracks at these defects depends on the stress level, which is determined by the amount of coarsening. In the strain controlled test, more coarsening caused a reduction in stress and an increase in life.

Precipitate coarsening is obviously very important in the high temperature deformation of MAR-M246+Hf. In DS Rene 80, coarsening has been shown to be accelerated by stress (83). To study this effect in MAR-M246+Hf, undeformed samples were held for 49 hours at 927°C and 1093°C. The resulting microstructures are shown in Figs. 44-45. After 49 hours at 927°C, the structure was not dramatically changed. In contrast, after 49 hours at 1093°C, grain boundary depletion of γ' had occurred (Fig. 44b) and the precipitates had coarsened greatly (Fig. 45b). Note that this was without applied stress, and was consistent with earlier observations on Rene 77 (82). The 927°C, 0.5%/minute LCF test coarsened significantly after 49 hours (Fig 42b). The 1093°C, 50%/min. LCF tests coarsened to a greater extent, after test times of about 30 minutes, and at 1093°C, 0.5%/min., the structure coarsened even in a tensile test (Fig. 25b). Thus in MAR-M246+Hf, the high mismatch provides a driving force for coarsening without deformation; however, deformation does increase the rate of coarsening significantly.

Grain Boundary Slip Behavior

The final topic of discussion concerns the grain boundary slip behavior observed at 20°C and 704°C (Figure 46). Studies of bicrystal deformation have provided fundamental information on the role of grain boundaries. As discussed by Hook and Hirth (65,66), the grain boundary is a

source of constraint on deformation, because to remain compatible at the boundary, the displacements across the boundary must be continuous. In an ideal DS structure, because of rotational freedom, the grains will possess different compliance matrices, relative to a common spatial coordinate system, leading to elastic incompatibility. In addition, deformation on the operative slip systems will not be geometrically continuous and consequently will cause plastic incompatibility. In an actual DS structure the situation is even more complicated because of a small allowable degree of tilt misorientation. The tilt misorientation will result in changes in modulus (and therefore stress) and changes in Schmid factors for any given slip system (105). In an HCF study on DS MAR-M246, HCF life was decreased when the orientation was more than 10 degrees from the [001] direction (108).

In Fig. 46a, the grain at the right showed primary slip with slip traces present on the entire grain surface. The grain on the left contained only short slip traces, adjacent to the grain boundary. In Fig. 46b, both grains exhibited primary slip. In the grain on the left, secondary slip was observed on two additional slip systems. These effects are similar to the results of bicrystal studies (63-66,114) and indicate that stresses can arise at the boundary due to incompatibility effects.

A detailed analysis of these slip patterns could be

made following the methods of Margolin (63). However, such an analysis would require knowledge of the exact crystallographic orientations of each grain. Because of the grain size, the available x-ray equipment could not be used for these determinations due to the width of the beam. Following the analysis of Prakash (67), the observed slip pattern can be rationalized based on misorientation. Equation 2.13 showed that the measure of incompatibility, Δ, increased with increasing rotation difference θ. The misorientations of the grains in Fig. 46 were measured by examining the grain structure on transverse planes. The secondary dendrite arms are aligned along <001> directions and may be used to measure orientation differences. The misorientation between the grains was 28 degrees in Fig. 46a and 7 degrees in Fig. 46b, correlating well with the observed degree of incompatibility slip. Greater rotational differences lead to greater amounts of stress near the boundary, which caused local slip.

CHAPTER V

SUMMARY AND CONCLUSIONS

1. The yield stress of DS MAR-M246 + Hf is relatively constant between 20°C and 704°C for the 50%/minute strain rate. At higher temperatures the yield stress drops with increasing temperature. This behavior is typical of other high volume fraction γ' alloys and is related to shearing of the γ' precipitate and a trade-off between matrix softening and precipitate hardening.

2. A strong dependence of yield stress on strain rate was seen at 927°C and 1093°C. This is indicative of the increasing role of thermal activation in deformation at higher temperatures. This behavior could be analysed in terms of an effective activation energy.

3. The monotonic strain hardening behavior changed with test condition. Strain hardening exponents of 0.072 at 20°C and 0.085 at 704°C, 50%/minute contrasted with a strain hardening exponent of 0.226 at 704°C, 0.5%/minute and comparably high strain hardening exponents at the higher temperatures. These results correspond to a change in slip

character from heterogeneous and planar to homogeneous, with 704°C representing a transition temperature.

4. On the basis of plastic strain range, LCF lives were shortest at 704°C and longest at 1093°C.

5. The effect of strain rate on LCF life was temperature dependent. At 704°C, based on plastic strain range, decreasing strain rate caused a life reduction, due to the higher stress for a given plastic strain range at the slow strain rate. On the basis of stress range, lives were equivalent between strain rates. At 927°C and 1093°C, decreasing strain rate caused beneficial coarsening and an increase in life for a given plastic strain range. On the basis of stress range, however, decreasing strain rate caused a life reduction because of an increase in the time available for oxidation for a given number of cycles. A model from the literature (85) based on oxidation was able to predict the life well at 1093°C. In life prediction for a turbine blade application, the exact character of the loading cycle should be known to avoid errors.

6. At 704°C and below, initiation was due to slip band formation at cracked carbides, and propagation was

crystallographic. At 927°C and above, initiation occurred perpendicular to the stress axis as a result of oxidation in interdendritic regions. Propagation was non-crystallographic, and the degree of crack branching tended to increase with temperature.

7. The deformation was found to be a strong function of strain rate and temperature. At lower temperatures and higher strain rates, the deformation mode was heterogeneous and planar. At intermediate temperatures, the deformation substructure was more homogeneous. At the highest temperatures, precipitate coarsening was the dominant characteristic of deformation.

8. The high mismatch of MAR-M246+Hf caused coarsening to occur at elevated temperatures even when no deformation was applied. Coarsening was greatly accelerated by applied deformation.

9. Slip behavior was influenced by grain boundaries in the DS structure. The presence of the boundaries provided additional constraints on deformation which lead to increased stresses at the boundary and secondary slip nucleation. The orientation differences between grains in

the structure also led to different stress responses for a given applied strain range.

CHAPTER VI

BIBLIOGRAPHY

1. C. H. Wells et al. "Mechanisms of Fatigue in the Creep Range." ASTM STP 495 (1971), pp. 61-122.

2. M. Gell and G. R. Leverant. "Mechanisms of High-Temperature Fatigue." ASTM STP 520 (1973), pp. 37-66.

3. L. F. Coffin, Jr. "Fatigue at High Temperatures." ASTM STP 520 (1973), pp. 5-32.

4. S. D. Antolovich. "Metallurgical Aspects of High Temperature Fatigue." Fatigue des Materiaux et des Structures. C. Bathias and J. P. Bailon, editors (1978).

5. S. D. Antolovich. "*Fatigue Mechanisms*". In Pressure Vessels and Piping - A Decade of Progress. S. Y. Zamrick and D. Dietrich, eds. ASME (1982), pp. 533-540.

6. R. F. Decker and C. T. Sims. "The Metallurgy of Nickel Base Alloys." In The Superalloys. C. T. Sims and W. C. Hagel, editors. John Wiley and Sons, N. Y. (1972), pp. 35-78.

7. R. F. Decker. Strengthening Mechanisms in Nickel Base Superalloys. International Nickel Company (1970).

8. S. D. Antolovich and J. E. Campbell. "Fracture Properties of Superalloys." Superalloys - Source Book. ASM, Metals Park, Ohio (1984), pp. 253-310.

9. D. P. Pope and J. L. Garin. "The Temperature Dependence of the Long Range Order Parameter of Ni_3Al." J. Appl. Cryst., 10 (1977), pp. 14-17.

10. M. Naik and G. S. Ansell. "Effect of Refractory Elements on the Coherency Strain and Flow Stress of Nickel-Base Superalloys." In Refractory Alloying Elements in Superalloys, ASM Conference Proceedings. Eds. J. K. Tien and S. Reichmann. ASM, Metals Park, Ohio (1984), pp. 153-164.

AD-A171 480 HIGH TEMPERATURE MONOTONIC AND CYCLIC DEFORMATION IN A DIRECTIONALLY SOLI..(U) GEORGIA INST OF TECH ATLANTA SCHOOL OF MATERIALS ENGINEERING.. E S HURON MAY 86 2/2

UNCLASSIFIED NASA-CR-175101 NAG3-503 F/G 11/6 NL

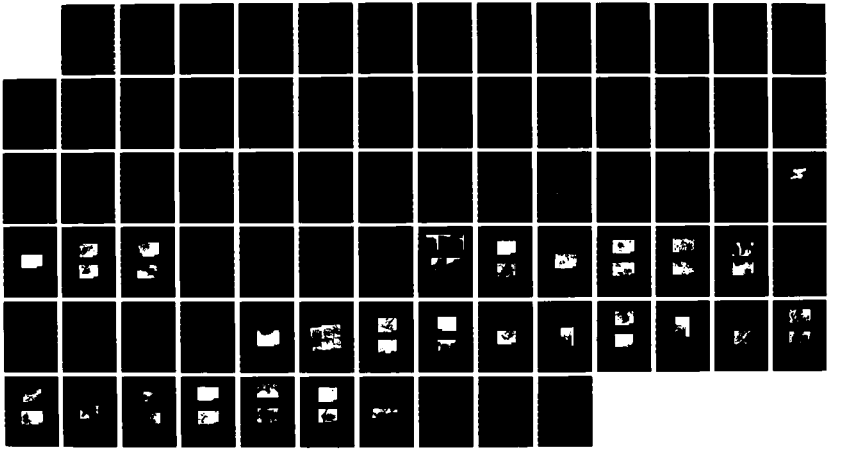

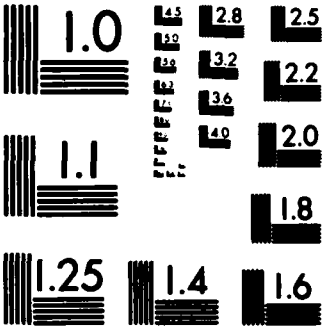

MICROCOPY RESOLUTION TEST CHART
NATIONAL BUREAU OF STANDARDS-1963-A

11. R. F., Decker and J. R. Mihalisin. "Coherency Strains of γ Hardened Nickel Alloys." ASM Transactions Quarterly, 62 (1969), pp. 481-489.

12. M. J. Donachie, Jr. "Relationship of Properties to Microstructure in Superalloys." Superalloys - Source Book. ASM, Metals Park (1984).

13. D. A. Grose and G. S. Ansell. "The Influence of Coherency Strains on the Elevated Temperature Tensile Behavior of Ni-15Cr-Al-Ti-Mo Alloys." Met. Trans., 12A (1981), pp. 1631-1645.

14. J. M. Oblak et al. "Precipitation of γ in the γ' of Nickel-Base Superalloys." Met. Trans., 5 (1974), pp. 1252-1254.

15. H. E. Collins. "The Effect of Thermal Exposure on the Microstructure and Mechanical properties of Nickel-Base Superalloys." Met. Trans., 5 (1974), pp. 189-203.

16. H. E. Collins. "Relative Long-Time Stability of Carbide and Intermediate Phases in Nickel-Base Superalloys." Trans. ASM, 62 (1969), pp. 82-104.

17. Z. Yunrong and C. Yulin. "Phase Transformations in Hafnium - Bearing Cast Nickel-Base Superalloys." Superalloys 1980, J. K. Tien et al., eds. ASM (1980), pp. 465-472.

18. J. E. Doherty, B. H. Kear, and A. F. Giamei. "On the Origin of the Ductility Enhancement in Hf-doped MAR-M200." J. Metals, 23, No. 11 (1971), pp. 59-62.

19. P. S. Kotval et al. "The Role of Hafnium in Modifying the Microstructure of Cast Nickel-Base Superalloys." Met. Trans., 3 (1972), pp. 453-458.

20. J. M. Dahl, W. F. Danesi, and R. G. Dunn. The Partitioning of Refractory Metal Elements in Hafnium-Modified Cast Nickel-Base Superalloys." Met. Trans., 4 (1973), pp. 1087-1096.

21. D. N. Duhl and C. P. Sullivan. "Some Effects of Hafnium Additions on the Mechanical Properties of a Columnar-Grained Nickel-Base Superalloy." J. Metals, 23, No. 7 (1971), pp. 38-40.

22. W. Betteridge and J. Heslop. The Nimonic Alloys. ne, Russak, and Company, New York (1974).

Published in England by Edward Arnold and Company (1959, 1961, 1974).

23. G. P. Sabol and R. Strickler. "Microstructure of Nickel-Based Superalloys." Phys. Stat. Sol., 35, No. 11 (1969), pp. 11-52.

24. B. H. Kear and D. E. Fornwalt. "On the Structure and Properties of Alloy B-1950." In Superalloys: Metallurgy and Manufacture. Proceedings of the 3rd International Symposium, Seven Springs, Pa., 1976. B. H. Kear et al., eds. Claitor's Publishing Division, Baton Rouge (1976), pp. 255-264.

25. C. T. Sims. "The Occurrence of Topologically Close Packed Phases." The Superalloys, edited by C. T. Sims and W. C. Hagel, John Wiley and Sons, N. Y. (1972). pp. 259-284.

26. A. Havalda. "Influence of Tungsten on the to Transformation and Carbide Reactions in Nickel-Base Superalloys." Trans. ASM, 62 (1969), pp. 581-589.

27. O. H. Kriege and J. M. Baris. "The Chemical Partitioning of Elements in Gamma Prime Separated from Precipitation-Hardened High Temperature Nickel-Base Alloys." Trans. ASM, 62 (1969), pp. 195-200.

28. C. Lall, S. Chin, D. P. Pope. "The Orientation and Temperature Dependence of the Yield Stress of $Ni_3(Al,Nb)$ Single Crystals." Met. Trans., 10A (1979), pp. 1323-1332.

29. J. K. Tien et al. "Cobalt Availability and Superalloys." J. Metals, 32 (1980), pp. 12-20.

30. G. E. Maurer, L. A. Jackman, and J. A. Dominique. "Role of Cobalt in Waspaloy." In Superalloys 1980, ed. by J. K. Tien et al., ASM, Metals Park, Ohio (1980), pp. 43-52.

31. M. V. Mathal, R. D. Maier, and L. J. Ebert. "The Influence of Cobalt on the Tensile and Stress-Rupture Properties of the Nickel-Base Superalloy MAR-M247." Met. Trans. A, 13A (1982), pp. 1767-1775.

32. N. F. Mott and F. R. N. Nabarro. Report of the Conference on Strength of Solids. Phys. Soc. (1948), pp. 1-19.

33. N. S. Stolloff. "Fundamentals of Strengthening." In

The Superalloys, edited by C. T. Sims and W. C. Hagel. John Wiley and Sons, New York, pp. 79-111.

34. R. W. Guard ,and J. H. Westbrook. "Alloying Behavior of Ni_3Al (γ Phase)." Trans. TMS-AIME, 215 (1959), pp. 807-814.

35. R. D. Rawlings and A. E. Staton-Bevan. "The Alloying Behavior ,and Mechanical Properties of Polycrystalline Ni_3Al (γ Phase) with Ternary Additions." J. Matls. Sci., 10 (1975), pp. 505-514.

36. D. P. Pope and S. S. Ezz. "Mechanical Properties of Ni_3Al and Nickel Base Alloys with High Volume Fraction of γ'." Inter. Met. Reviews, 29, No. 3 (1984), pp. 136-167.

37. D. Hull and D. J. Bacon. Introduction to Dislocations, 3rd ed. Pergamon, Oxford (1984).

38. P. A. Flinn. "Theory of Deformation in Superlattices." Trans. TMS-AIME, 218 (1960), pp. 145-154.

39. B. H. Kear. J. M Oblak, and A. F. Giamei. "Stacking Faults in Gamma Prime $Ni_3(Al,Ti)$ Precipitation Hardened Nickel-Base Alloys." Met. Trans., 1 (1970), pp. 2477-2486.

40. S. Takeuchi and E. Kuramoto. "Temperature and Orientation Dependence of the Yield Stress in Ni_3Ga Single Crystals." Acta Met., 21 (1973), pp. 415-425.

41. B. H. Kear, G. R. Leverant, and J. M. Oblak. "An Analysis of Creep-Induced Intrinsic/Extrinsic Fault Pairs in a Precipitation Hardened Nickel-Base Alloy." Trans. ASM, 62 (1969), pp. 639-650.

42. B. H. Kear and H. G. F. Wilsdorf. "Dislocation Configurations in Plastically Deformed Polycrystalline Cu_3Au Alloys." Trans. AIME, 224 (1962), pp. 382-386.

43. P. H. Thornton, R. G. Davies, and T. L. Johnston. "The ,Orientation Dependence of the Flow Stress of the γ Phase Based upon Ni_3 Al." Met. Trans., 1 (1970), pp. 207-218.

44. E. Kuramoto and D. P. Pope. "The Orientation Dependence of The Yield Stress of $Ni_3(Al,W)$." Acta Met., 26 (1978), pp. 207-210.

45. S. S. Ezz, D. P. Pope, V. Paidar. "The Tension/Compression Flow Stress Asymmetry in $Ni_3(Al,Nb)$ Single Crystals." Acta. Met., 30 (1982), pp. 921-926.

46. R. G. Davies and T. L. Johnston. "The Metallurgical Design of a Superalloy." Ordered Alloys, ed. B. H. Kear et al. Claitor's Publishing Division, Baton Rouge, La. (1970), pp. 447-474.

47. R. A. Ricks, R. J. Porter, and R. C. Ecob. "The Growth of precipitates in Nickel-Base Superalloys." Acta Met., 31 (1983), pp. 43-53.

48. S. D. Antolovich and N. Jayaraman. "Effects of ENvironment and Structural Stability on the Low Cycle Fatigue Behavior of Nickel-Base Superalloys." High Temperature Technology, 2, No. 1, (1984), pp. 3-13.

49. M. Gell and G. R. Leverant. "The Fatigue of the Nickel-Base Superalloy, MAR-M200, in Single Crystal and Columnar-Grained Forms at Room Temperature." Trans. TMS-AIME, 242 (1968), pp. 1869-1879.

50. G. R. Leverant and M. Gell. "The Elevated Temperature Fatigue of a Nickel-Base Superalloy, MAR-M200, in Conventionally-Cast and Directionally-Solidified Forms." Trans. TMS-AIME, 245 (1969), pp. 1167-1173.

51. T. L. Johnston and C. E. Feltner. "Grain Size Effects in the Strain Hardening of Polycrystals." Met. Trans. 1 (1970), pp. 1161-1167.

52. E. O. Hall. "The Deformation and Aging of Mild Steel: III." Proc. Phys. Soc. (London), 64B (1951), pp. 747-752.

53. N. J. Petch. "The Cleavage Strength of Polycrystals." J. Iron Steel Inst., 174 (1953), pp. 25-28.

54. W. J. Tegart. Elements of Mechanical Metallurgy. McMillan, New York (1966), p. 178.

55. W. M. Baldwin. "Yield Strength of Metals as a Function of Grain Size." Acta Met., 6 (1958), pp. 139-141.

56. J. C. Li and Y. T. Chou. "The Role of Dislocations in the Flow Stress Grain Size Relationships." Met. Trans., 1 (1970), pp. 1145-1159.

57. T. G. Langdon and F. A. Mohamed. "The Enhancement of Creep Rates in Engineering Materials due to Grain Boundary processes." In Grain Boundaries in Engineering Materials. Proceedings of the Fourth Bolton Landing Conference, June 1974. Edited by J. L. Walter, J. H. Westbrook, and D. A. Woodford. Claitor's, Baton Rouge, La. (1975), pp. 339-352.

58. H. J. Frost and M. F. Ashby. Deformation Mechanism Maps. Pergamon, Oxford (1982).

59. J. H. Brophy. "The Role of Grain Boundaries in the Creep and Fatigue of Nickel Containing Alloys." In Grain Boundaries in Engineering Materials. Proceedings of the Fourth Bolton Landing Conference, June 1974. Edited by J. L. Walter, J. H. Westbrook, and D. A. Woodford. Claitor's, Baton Rouge, La. (1975), pp. 289-306.

60. R. Raj and M. F. Ashby. "On Grain Boundary Sliding and Diffusional Creep." Met. Trans., 2 (1971), pp. 1113-1127.

61. K. T. Aust and N. K. Chen. "Effect of orientation Difference on the Plastic Deformation of Aluminum Bicrystals." Acta Met., 2 (1954), pp. 632-638.

62. J. J. Hauser and B. Chalmers. "The Plastic Deformation of Bicrystals of F. C. C. Metals." Acta Met., 9 (1961), pp. 802-818.

63. Yii-Der Chuang and H. Margolin. "Brass Bicrystal Stress-Strain Relationships." Met. Trans., 4, (1973), pp. 1905-1917.

64. T. K. Lee and H. Margolin. "Beta Brass Bicrystal and Tri-Crystal Stress strain Behavior." Meta. Trans., 8A (1977), pp. 157-167.

65. R. E. Hook and J. P. Hirth. "The Deformation Behavior of Isoaxial Bicrystals of Fe-3% Si." Acta Met., 15 (1967), pp. 535-551.

66. R. E. Hook and J. P. Hirth. "The Deformation Behavior of Isoaxial Bicrystals of Fe-3% Si." Acta Met., 15 (1967), pp. 1099-1110.

67. A. Prakash. PhD Thesis, University of Cincinnati (1981).

68. P. Beardmore, R. G. Davies, T. L. Johnston. "On the

Temperature Dependence of the Flow Stress of Nickel-Base Alloys." Trans. TMS-AIME, 245 (1969), pp. 1532-1545.

69. B. J. Piearcey, B. H. Kear, and R. W. Smashey. "Correlation of Structure with Properties in a Directionally Solidified Nickel-Base Superalloy." Trans. ASM, 50 (1967), pp. 634-644.

70. S. M. Copley and B. H. Kear. "A Dynamic Theory of Coherent Precipitation with Application to Nickel-Base Superalloys." Trans. TMS-AIME, 239 (1967), pp. 984-992.

71. G. R. Leverant. M. Gell, and S. W. Hopkins. "The Effect of Strain Rate on the Flow Stress and Dislocation Behavior of a precipitation-Hardened Nickel-Base Alloy." Mater. Sci. Eng., 8 (1971), pp. 125-122.

72. G. R. Leverant and B. H. Kear. "The Mechanism of Creep in Gamma Prime Precipitation-Hardened Nickel-Base Alloys at Intermediate Temperatures." Met. Trans., 1 (1970), pp. 491-498.

73. G. R. Leverant, B. H. Kear. J. M. Oblak. "Creep of Precipitation Hardened Nickel-Base Alloy Single Crystals at High Temperatures." Met. Trans. 4, (1973), pp. 355-362.

74. P. R. Paslay, C. H. Wells, G. R. Leverant. "An Analysis of Primary Creep of Nickel-Base Superalloy Single Crystals." Journal of Applied Mechanics, Sept. (1970), pp. 759-764.

75. J. J. Jackson et al. "The Effect of Volume Percent of Fine γ' on Creep in DS MAR-M200+Hf." Met. Trans., 8A (1977), pp. 1615-1620.

76. R. A. MacKay and R. D. Maier. "The Influence of Orientation on the Stress Rupture Properties of Nickel-Base Superalloy Single Crystals." Met. Trans., 13A (1982), pp. 1747-1754.

77. M. Gell and G. R. Leverant. "The Characteristics of Stage I Fatigue Fracture in a High-Strength Nickel Alloy." Acta met., 16 (1968), pp. 553-561.

78. G. R. Leverant and M. Gell. "The Influence of Temperature and Cyclic Frequency on the Fatigue Fracture of Cube Oriented Nickel-Base Superalloy

Single Crystals." Met. Trans., 6A (1975), pp. 367-371.

79. D. J. Duquette and M. Gell. "The Effects of Environment on the Elevated Temperature Fatigue Behavior of Nickel-Base Superalloy Single Crystals." Met. Trans., 3 (1972), pp. 1899-1905.

80. W. W. Milligan, N. Jayaraman, and R. C. Bill. "Low Cycle Fatigue of MAR-M200 Single Crystals at 760 and 870°C." NASA TM-86933, LeRC (1984).

81. M. A. Burke and C. G. Beck. "The High Temperature Low Cycle Fatigue Behavior of the Nickel Base Alloy IN-617." Met. Trans., 15A (1984), pp. 661-670.

82. S. D. Antolovich, E. Rosa, and A. Pineau. "Low Cycle Fatigue of Rene 77 at Elevated Temperatures." Mat. Sci. Eng., 47 (1981), pp. 47-57.

83. S. D. Antolovic , S. Liu, and R. Baur. "Low Cycle Fatigue Behavior of Rene 80 at Elevated Temperature." Met. Trans., 12A (1981), pp. 473-481.

84. L. F. Coffin, Jr. "The Effect of Frequency on the Cyclic Strain and Fatigue Behavior of Cast Rene at 1600°F." Met. Trans., 5 (1974), pp. 1053-1060.

85. S. D. Antolovich, R. Baur, and S. Liu. "A Mechanistically Based Model for High Temperature LCF of Ni Base Superalloys." Superalloys 1980, J. K. Tien et al., eds. ASM, Metals Park (1980), pp. 605-614.

86. F. E. Organ and M. Gell. "The Effect of Frequency on the Elevated Temperature Fatigue of a Nickel-Base Superalloy." Met. Trans., 2 (1971), pp. 943-952.

87. B. L. Lerch, N. Jayaraman, and S. D. Antolovich. "A Study of Fatigue Damage Mechanisms in Waspaloy from 25 to 800°C." Mat. Sci. Eng., 66 (1984), pp. 151-166.

88. R. E. Stoltz and A. G. Pineau. "Dislocation-Precipitate Interaction and Cyclic Stress-Strain Behavior of a γ' Strengthened Superalloy." Mat. Sci. and Eng., Vol. 34 (1978), pp. 275-284.

89. C. H. Wells and C. P. Sullivan. "The Effect of Temperature on the Low Cycle Fatigue Behavior of Udimet 700." Trans. ASM, 60 (1967), pp. 217-222.

90. C. J. MaMahon and L. F. Coffin, Jr. "Mechanisms of

Damage and Fracture in High-Temperature, Low-Cycle Fatigue of a Cast Nickel-Base Superalloy." Met. Trans., 1 (1970), pp. 3443-3450.

91. K. R. Bain and R. M. Pelloux. "Effect of Environment on Creep Crack Growth in PM/HIP Rene-95." Met. Trans., 15A (1984), pp. 381-388.

92. J. M. Davidson and J. K. Tien. "Environmental Effects on the Creep Behavior of a Nickel-Base Superalloy." Met. Trans., 12A (1981), pp. 865-876.

93. F. L. Versnyder and M. E. Shank. "The Development of Columnar Grain and Single Crystal High Temperature Materials Through Directional Solidification." Mater. Sci. Eng., 6 (1970), pp. 213-247.

94. T. E. Strangman et al. "Development of Exothermically Cast Single-Crystal MAR-M247 and Derivative Alloys." Superalloys 1980, J. K. Tien et al., eds. ASM (1980), pp. 215-224.

95. G. S. Hoppin III, M. Fujii, and L. W. Sink. "Development of Low-Cost Directionally Solidified Turbine Blades." Superalloys 1980, J. K. Tien et al., eds. ASM, Metals Park (1980), pp. 225-234.

96. K. Harris, G. L. Erickson, and R. E. Schwer. "MAR-M247 Derivatives - CM 247 LC DS Alloy - CMSX Single Crystal Alloys - Properties and Performance." Superalloys 1984, AIME, New York (1984), pp. 221-230.

97. J. E. Northwood and T. Homewood. "Unidirectional Solidification of High-Temperature Materials for Gas Turbines." Metallurgia and Metal Forming, 41 (1974), pp. 254-262.

98. J. E. Northwood. "Improving Turbine Blade Performance by Solidification Control." In Superalloys - Source Book. ASM, Metals Park (1980), pp. 292-296.

99. G. F. Harrison and G. P. Tilly. "The Static and Cyclic Creep Properties of Three Forms of a Cast Nickel Alloy," in Creep and Fatigue in Elevated Temperature Applications - International Conference of ASME. Vol. 1 (1975), pp. 222.1-222.9.

100. P. K. Wright and A. F. Anderson. "The Influence of Orientation on the Fatigue of Directionally Solidified Superalloys." Superalloys 1980, J. K. Tien et al. eds. ASM, Metals Park (1980), pp. 689-698.

101. G. R. Leverant and D. N. Duhl. "The Effect of Stress and Temperature on the Extent of Primary Creep in Directionally Solidified Nickel-Base Superalloys." Met. Trans., 2 (1971), pp. 907-908.

102. Lin Dongliang, Y. Deliang, and S. Chuangi. "The Effect of Stress and Temperature on the Extent of Primary Creep in Directionally Solidified Nickel-Base Alloys." Superalloys 1984. AIME, New York (1984), pp. 199-210.

103. D. A. Woodford and J. J. Frawley. "The Effect of Grain Boundary Orientation on Creep and Rupture of IN-738 and Nichrome." Met. Trans., 5 (1974), pp. 2005-2013.

104. M. Yan et al. "Influence of Grain Boundaries on the Mechanical Properties and Fracture Characteristics in a Directionally Solidified Superalloy." Mechanical Behavior of Materials IV, Proc. Conf., Stockholm, 1983. Volume 1, Pergamon Press, Oxford (1984), pp. 307-315.

105. M. Raguet, S. D. Antolovich, and R. K. Payne. "Fatigue and Deformation Behavior of Directionally Solidified Rene 80." Superalloys 1984, Proc. of 5th Intl. Symp. Edited by M. Gell et al. AIME, New york (1984), pp. 231-241.

106. P. T. Bizon and D. A. Spera. "Thermal Stress Behavior of Twenty-Six Superalloys." In Thermal Fatigue of Materials and Components. ASTM STP 612, D. A. Spera and D. F. Mowbray, eds. ASTM (1976), pp. 106-122.

107. R. Bowman. M. S. Thesis, Georgia Institute of Technology, Atlanta, Georgia (1985).

108. M. H. Johnston and R. A. Parr. "A Study of the Solidification Parameters Influencing Structures and Properties in MAR-M246(Hf)." NASA TM-82569, Marshall Space Flight Center (1984).

109. J. E. Restall. "Experimental Cast Nickel Superalloys and Gamma-Prime Alloys for High Temperature Applications in Gas Turbines." In Superalloys: Metallurgy and Manufacture. Proceedings of the 3rd International Symposium, Seven Springs, Pa., 1976. B. H. Kear et al., eds. Claitor's Publishing Division, Baton Rouge (1976), pp. 351-359.

110. W. W. Milligan and S. D. Antolovich. "Yielding and

Deformation Behavior of the Single Crystal Superalloy PWA 1480." Paper submitted for publication.

111. L. F. Coffin, Jr. "Predictive Parameters and Their Application to High Temperature, Low Cycle Fatigue." Proc., Inter. Conf. on Fracture (1969), pp. 643-654.

112. R. P. Dalal, C. R. Thomas, and L. E. Dardi. "The Effect of Crystallographic Orientation on the Physical and Mechanical Properties of an Investment Cast Single Crystal Nickel-Base Superalloy." Superalloys 1984, Proc. of 5th Intl. Symp. Edited by M. Gell et al. AIME, New York (1984), pp. 231-241.

113. L. Masserelli. "High Temperature Low Cycle Fatigue Behavior of Cast IN738LC Alloy." Agard CP 243, April (1973), pp. 8-1 - 8-5.

114. M. Marchionni, D. Ranucci, and E. Picco. "High-Temperature Low Cycle Fatigue Behavior of IN739LC Alloy in Air and in Vacuum." In High Temperature Alloys for Gas Turbines, 1982. R. Brunetaud et al., eds. D. Reidel Publishing Company, Dordrecht, Holland (1982), pp. 791-804.

115. R. B. Scarlin. "Fatigue Crack Propagation in a Directionally-Solidified Nickel-Base Alloy." Met. Trans., Vol. 7A (1976), pp. 1535-1541.

116. J. C. Swearingen and R. Taggart. "Low Amplitude Cyclic Deformation and Crack Nucleation in Copper and Copper-Aluminum Bicrystals." Acta Met. 19 (1971), pp. 543-559.

117. C. H. Wells. "The Elastic Constants of a Directionally Solidified, Nickel-Base Superalloy, MAR-M200." Trans. ASM, 60 (1967), pp. 270-271.

118. B. L. Lerch. "Microstructural Effects on the Room and Elevated Temperature Low Cycle Fatigue Behavior of Waspaloy." NASA CR165497, NASA Lewis Research Center (1982), p. 53.

APPENDIX A

SAMPLE PREPARATION, SECTIONING AND METALLOGRAPHY

Sample Preparation

All specimens were electropolished before testing to reduce surface-related scatter in the results. Specimens were ultrasonically cleaned in methanol to remove any surface oils. The ends and shoulders of the specimens were coated in a commercial polymer coating, leaving only the gauge section exposed. Care was taken during this step to keep the gauge section clean. A solution of 45% glacial acetic acid, 45% butyl cellusolve, and 10% perchloric acid (70%), maintained at 10°C, was used at a voltage of 27-35 V and a current of approximately 70 mA. The specimen was suspended vertically in the solution, which was contained in a stainless steel beaker. It was found that positioning the specimen accurately in the center of the beaker was important to avoid uneven polishing. The specimen diameter was typically reduced by 0.025 mm during the electropolishing process.

Sample Sectioning and Examination

The as-received material was characterized using metallography and x-ray diffraction. Lattice parameters were determined using a Phillips iffractometer and copper

$K\alpha$ radiation. A small block (0.5 cm x 2 cm x 3 cm) was available for this purpose. Slices 0.2 mm thick parallel to the columnar grains (longitudinal) and perpendicular to the columnar grains (transverse) were used for TEM foil preparation as described below.

Tested samples were examined optically. On some specimens, cellulose acetate replicas were taken of the specimen surface. After examination the samples were sectioned. One specimen half was sectioned tranversely below the fracture surface. This specimen was used for SEM analysis of the fracture surface. Transverse slices 0.2 mm thick were cut for TEM foil preparation. The other specimen half was sectioned longitudinally through the fracture surface. This small sample was mounted for optical examination of the microstructure and fracture surface profiles. The undeformed coarsening samples were also sectioned for optical and TEM examination.

Metallography

All optical metallography specimens were prepared using standard techniques. Specimens were mounted in bakelite, rough polished on silicon carbide papers, in the grit sequence of 240, 320, 400, and 600. Further polishing was done using diamond pastes of 6 micron and 1 micron sizes, and final polishing was done using 0.05 micron alumina slurry. Specimens were either examined in the

unetched condition or were etched using a solution of 33% nitric acid, 33% acetic acid, 33% water, and 1% hydroflouric acid, and immersion times of 10-15 seconds.

A LECO Corp. Automet attachment was used for polishing. This is a mechanical polishing attachment that maintains the plane of the sample normal to the polishing wheel surface. This prevents edge rounding and facilitates examination of surface features such as oxidation and crack paths.

Discs 3 mm in diameter were taken from the 0.2 mm slices for TEM foil preparation. These cut using a Bronwill slow rate precision saw, with water cooling to prevent excessive sample heating. Foils were electropolished in a Struers Tenupol unit using a solution of 60% methanol, 35% butyl cellusolve, and 5% perchloric acid, maintained at $-25^{o}C$. The voltage used was 18 V with a current of approximately 30 mA, and thinning times averaged 5 minutes. Thinning performance of the solution was found to diminish after 5-7 foils, so the solution was replaced frequently.

length of the extensometer was 14.35 mm.

The entire extensometer was suspended from a column of the load frame using a machined aluminum bracket with two pulleys, over which a thread and a counter weight was hung. The counter weight was a brass cup filled with lead. The extensometer was held against the sample using another bracket, mounted on the opposite column of the load frame. Two 0.2 mm wires were passed through the holes in the sharp tips, bent in a U-shape, with one leg of the U passing on each side of the specimen, and a 3 mm loop was formed on each end of the wire. Springs were attached from the bracket to glass hooks, which hooked into the loops of the wire. The bracket was constructed in two parts, with one part attached to the load column and the other part held in a sliding groove to allow adjustment of the spring tension.

The extensometer was carefully calibrated using a precision Instron extensometer micrometer calibrator. The voltage corresponding to various levels of tensile and compressive strain was recorded. Linear regression was performed on the strain/voltage points and the resulting equation was used to generate a scale factor for the SATEC strain module. The extensometer was modified and improved until consistent, linear strain vs. voltage values were obtained, with no binding or excessive hinge resistance. Critical areas were the hinge thickness, chosen to prevent

APPENDIX B

MECHANICAL TESTING PROCEDURE

Extensometer

The extensometer is extremely important in strain-controlled testing. The extensometer used in this investigation was based on a modification of an MTS Corp. 632.11 clip gauge for high temperature service. The extensometer is shown in Figure 47. The extensometer consisted of two 6.35 mm diameter alumina rods, 190.5 mm in length, hinged at midlength using a 0.38 mm thick sheet steel hinge. A spring steel loop was wound around the top extensometer rod for attachment of the extensometer suspension cord, and two more spring steel loops were wound around one end of each rod, about 3 cm from the end, for clip-on gauge attachment. The opposite end of each rod was ground to a sharp wedge point using a diamond faced wheel. A 1.0 mm diameter hole was drilled horizontally about 5 mm from the point in each rod. Aluminum cubes, 1.5 cm in size, were drilled to fit over the clip-gauge ends of each rod. Several closely-spaced horizontal grooves were cut on the faces of the cube opposite the pointed ends of the extensometer. These were cut using a fine steel wire coated in diamond paste. The clip-on gauge was fastened to the extensometer, seated in these grooves, and attached using 2 cm springs to the spring steel loops. The resulting gauge

excessive looseness of the extensometer but allow a minimum of spring tension, the balance of the extensometer while hanging, and the grooves in the aluminum end blocks. Shallowness of these grooves was mandatory to prevent binding of the clip-on gauge knife edges at large deflections.

Temperature Control

Temperature Control was achieved through induction heating, using a Lepel 2.5KW generator and induction coils formed from copper tubing. Calibration of the sample temperature was carefully performed using a specimen with multiple chromel-alumel thermocouples over the gauge length and shoulders. The coil and Lepel unit were adjusted until a temperature gradient of +/- $2^{o}C$ was maintained over the gauge length of the specimen. For tensile specimens, thermocouples were attached directly to the gauge section and one of these thermocouples was used for control based on the calibration specimen. For LCF specimens, a shoulder thermocouple was attached to the calibration specimen. The coil was adjusted so the difference in shoulder and gauge section temperatures was as small as possible (generally less than $5^{o}C$). For the test specimens, thermocouples were attached only to the shoulders and one of these thermocouples was used for control, based on the calibration specimen.

Tensile Testing

Tensile tests were performed using strain control to a point past yielding (approximately 1.0% strain) and stroke control for the remainder of the test at a displacement rate chosen to be approximately equivalent to the desired strain rate. The interrupted 704°C test was performed using a feature of the SATEC machine called combinatorial feedback. An equation was programmed into the machine which measured plastic strain based on a previously measured modulus and the machine load. The test was run in strain control until this equation detected a plastic strain of 0.2%, at which time the sample was returned to zero load at an unloading rate of 20000lb/min. The equation was:

$$\Delta\varepsilon_p = \Delta\varepsilon_T - (\sigma/\text{LOAD}.E) \qquad \text{(B.1)}$$

The modulus was measured by loading to 300 lb and measuring the slope of the stress-strain curve. Note that the machine constantly measured total strain and load, and when given a value of area and modulus this equation provided a means of ending the test at a given level of plastic strain. This equation assumes a constant area, and the small error introduced by contraction of the specimen is negligible.

Low Cycle Fatigue Testing

LCF tests were performed over the same temperature

and strain rates as the tension tests using total axial strain control and a fully reversed triangle waveform. The desired strain rates were achieved by choosing a frequency based on the total strain range as follows:

$$\nu\ (\text{Hz}) = \frac{1\ \text{cycle}}{\Delta\varepsilon_t} \times \frac{\text{strain}}{\text{min}} \times \frac{1\ \text{min}}{60\ \text{sec}} \qquad \text{(B.2)}$$

To minimize the effects of air current and fluctuations in the sample temperature due to air conditioning or heating changes, a clear plexiglas enclosure was built to fit around the load columns, between the lower block and the crosshead of the test rig.

Table 1: Chemical Compositions

Composition(%)	MAR-M200 (nominal)	MAR-M246 (nominal)	MAR-M246+Hf (this study)
C	0.15%	0.15%	0.16%
Ni	59	59	Balance
Cr	9	8.25	8.13
Co	10	10	10.15
Mo			2.42
Fe	1		0.05
Al	5	5.5	5.60
B	0.015	0.015	0.018
Ti	2	1.5	1.59
W	12.5	10	9.35
Zr	0.05	0.05	0.03
Nb	1		
Ta		1.5	1.52
Hf			1.95

Table 2: Effect of Hafnium on Tensile Properties of MAR-M200 (Ref. 21)

(directionally solidified)

Orientation	Hf Content (%)	Temp. (C)	0.2% Yield Stress (MPa)	UTS (MPa)	Elong. (%)	Reduction of Area (%)
Longitudinal	nil	20	945	1055	7.7	8.5
		760	1034	1186	7.5	8.6
		982	448	586	18.0	25.6
	2.0	20	938	1110	6.1	8.3
		760	965	1186	9.0	14.0
		982	476	614	21.8	28.0
Transverse	nil	20	800	814	3.0	6.2
		760	807	848	1.7	1.9
		982	393	524	4.2	2.4
	2.0	20	807	917	9.0	14.5
		760	793	972	7.2	13.5
		982	462	586	17.4	15.3

Table 3: Effect of Hafnium on Tensile Properties of MAR-M246 (Ref. 22)

(conventionally cast)

Hafnium Content (%)	Temp. (C)	0.1% Yield Stress (MPa)	UTS (MPa)	Elong. (%)	Reduction of Area (%)
Nil	20	847	938	2.8	7.0
	500	779	975	4.6	7.0
	760	791	940	2.1	3.5
	1000	304	530	5.4	7.1
1.5	20	811	1025	7.1	12.2
	500	803	1008	7.1	7.9
	760	839	1106	6.4	9.4
	1000	303	570	10.3	13.1

Table 4: Tension Matrix

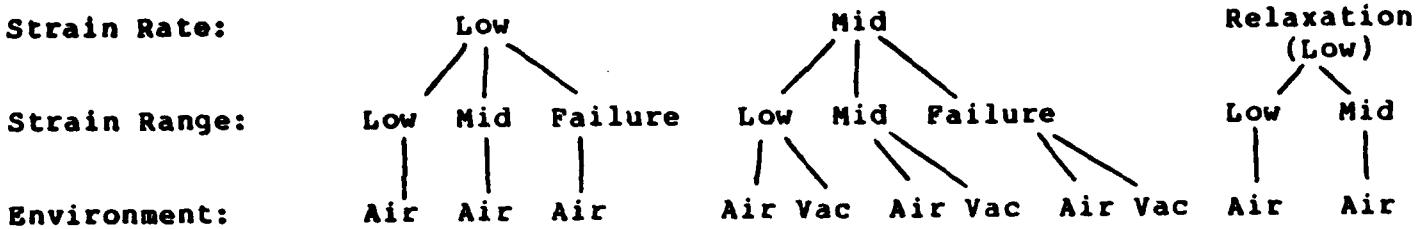

Room Temperature						1*		
704°C/1300°F	1	1*	2	1	1*	1*	1	1
927°C/1700°F	1	1*	2	1	1	1*	1	1
1093°C/2000°F	1	1*	2	1	1	1*	1	1

28 Specimens Total

* - completed tests

Table 5 : Isothermal Fatigue Matrix

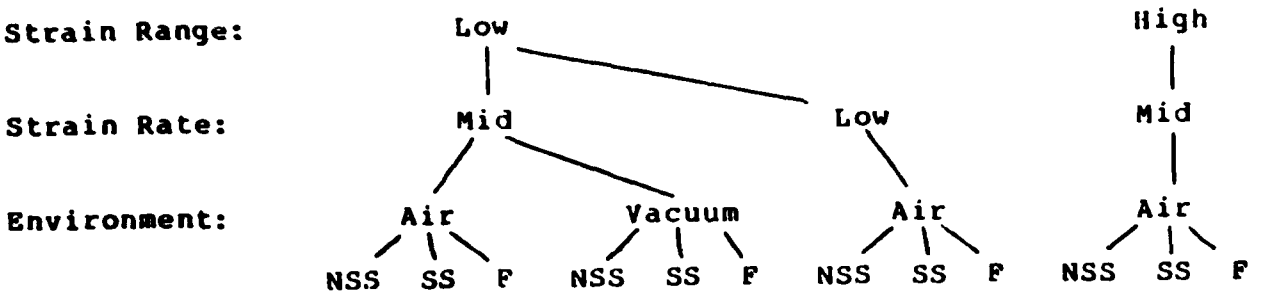

Room Temperature	1	1	1*									
704°C/1300°F	1	1	2*	1	1	1	1	1	2*	1	1	2*
927°C/1700°F	1	1	2*	1	1	1	1	1	2*	1	1	2*
1093°C/2000°F	1	1	2*	1	1	1	1	1	2*	1	1	2*

48 Specimens Total

NSS = Non-Steady State Response
SS = Steady State Response
F = Failure

* - completed tests

Table 6: Tensile Data

Code	Temp (°C)	Strain Rate %/min	Young's Modulus (GPa)	Yield Strength (MPa) 0.05%	0.1%	0.2%	UTS (MPa)	Red. in Area (%)	Strain Hardening Exponent (n)
RTFF1	20	50	119.9	865.3	903.9	915.0	1141.1	7.9	.072
13FH1	704	50	106.2	900.5	907.4	914.6	-	-	.085a.
13SF1	704	0.5	116.5	749.4	831.5	913.6	-	6.4	.226b.
17FF1	927	50	90.3	615.6	675.4	703.6	902.0	8.6	.271
17SF1	927	0.5	82.7	464.4	499.5	562.1	703.6	14.6	.375
20FF1	1093	50	68.4	225.1	242.7	260.3	385.6	35.4	.317
20SF1	1093	0.5	63.6	151.3	161.8	175.9	216.8	37.3	.221

NOTES: a. Interrupted test. b. Test failed outside gage length.

Table 7: Low Cycle Fatigue Data

Code	Temp (°C)	Strain Rate (%/min)	Total Strain Range (%)	Plastic Strain Range(a) (%)	Stress Range σ r/2(a) (MPa)	Young's Modulus (GPa)	Cycles to Init.	Cycles to Failure
RTFLF	20	50	1.750	.1517	1028.1	135.1	396	396
13FLF	704	50	1.790	.0968	891.9	106.9	370	386
13FLF2	704	50	1.790	.1290	867.4	100.0	191	191
13FLLF	704	50	1.684	.1064	843.3	104.8	279b	279
13FLLF2	704	50	1.512	.0288	778.7	107.6	1308	1357
13SLF	704	0.5	1.790	.0258	876.0	102.0	380	409
13SLF2	704	0.5	1.790	.0226	869.4	101.4	441	446
17FLF	927	50	1.554	.1742	697.8	94.5	406	417b
17FLF2	927	50	1.554	.1355	635.2	91.0	806	811b
17FLLF	927	50	1.166	.0387	518.6	93.7	3764	3769
17FLLF2	927	50	1.166	.0323	467.6	94.5	6049	6049b
17SLF	927	0.5	1.016	.1740	379.1	94.5	1317	1459
20FLF	1093	50	.756	.2412	175.9	61.4	1954	2050
20FLF2	1093	50	.648	.2000	160.0	65.5	2466	2601
20FLLF	1093	50	.565	.0989	168.8	73.8	c	c
20FLLF2	1093d	50	.565	.0903	141.3	62.7	7231	7425
20SLF2	1093	0.5	.504	.2060	93.5	67.6	6526	8849

NOTES: a. At half-life. b. Outside gage length of extensometer. c. Testing machine shutoff due to error. d. Temperature fell 10°C after half-life.

Table 8: Life Correlation Results

(all for 50%/minute strain rate)

Parameter	Temperature (^{o}C)	Correlation Coefficient
$\Delta\varepsilon_p$	704	0.996
	927	0.986
	1093	0.999
$\Delta\varepsilon_t$	704	0.967
	927	0.930
	1093	0.861
σ_{MAX}	704	0.872
	927	0.930
	1093	0.864
$\varepsilon_t \cdot E$	704	0.998
	927	0.954
	1093	0.975
$\varepsilon_t \cdot E \cdot \sigma_{MAX}$	704	0.971
	927	0.979
	1093	0.945

Table 9: Comparison of Monotonic and Cyclic Strain Hardening Exponents

Temperature (C)	Strain Rate (%/min)	Monotonic (n)	Cyclic (n')
20	50	.072	
740	50	.085	.076
704	0.5	.226	
927	50	.271	.189
927	0.5	.375	
1093	50	.317	.167
1093	0.5	.221	

Table 10: Activation Energies for Yielding

Strain Rate (%/min)	Temperature (C)	Q* (KJ)	Q (KJ)
50	t > 927	60.7	592
	704 < t <927	10.7	104
0.5	t > 927	72.9	710
	704 < t < 927	55.5	54

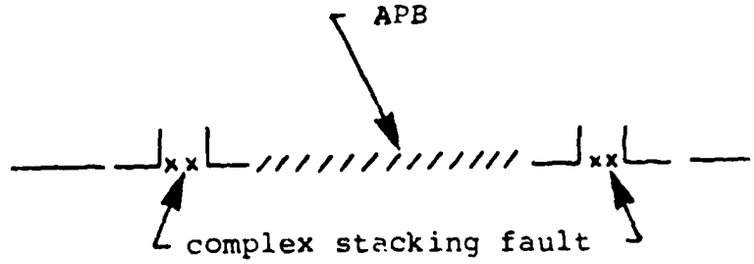

Figure 1. Dislocation Configuration in Ni_3Al.
Two a/2 <110> dislocations, separated by a region of anti-phase boundary energy (APBE), are each split into their constituent partials. Ref. 36.

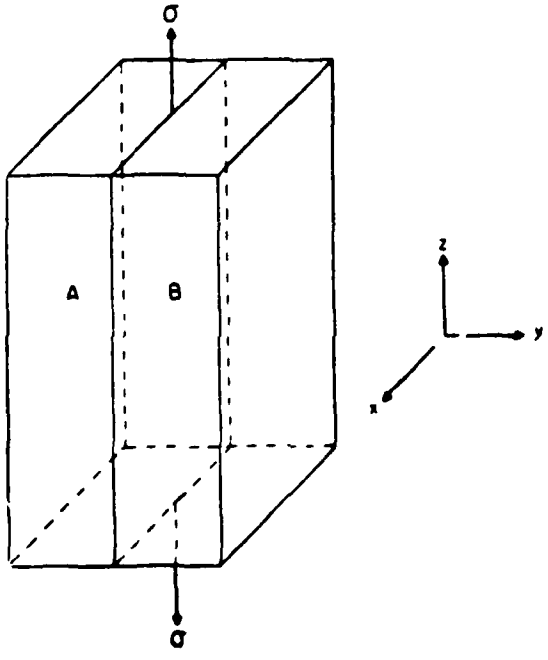

Figure 2. Bicrystal Geometry. Ref. 65.

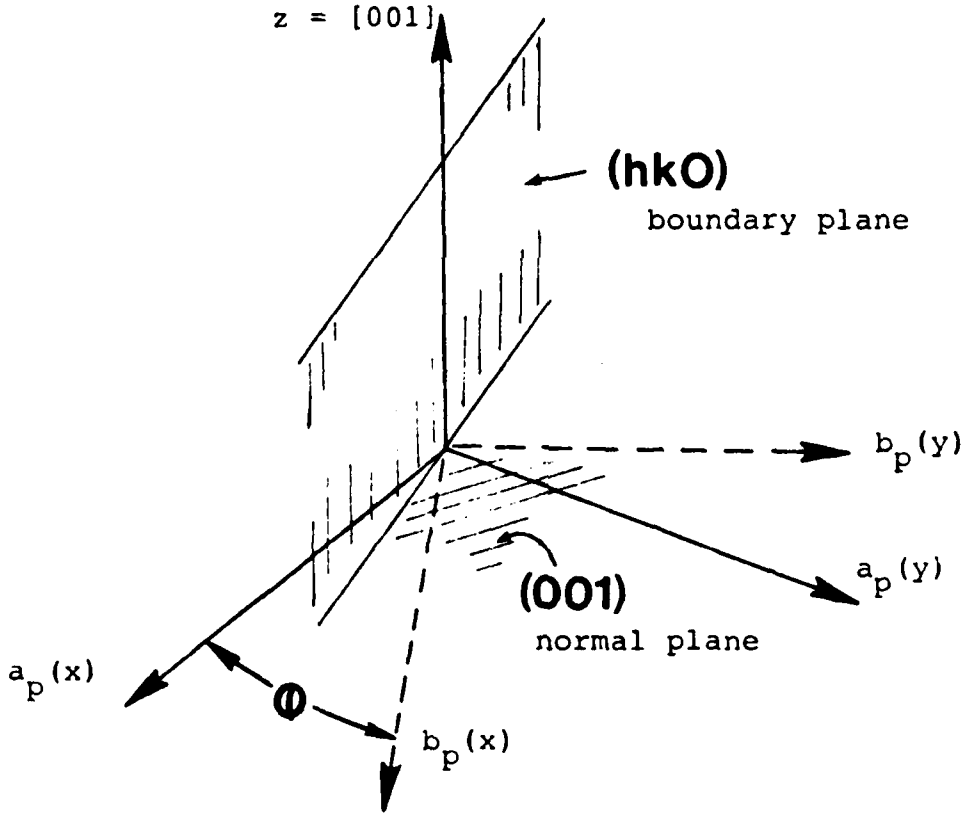

Figure 3. Projected Slip Vector Analysis of Grain Boundary Incompatibility. Ref. 67.

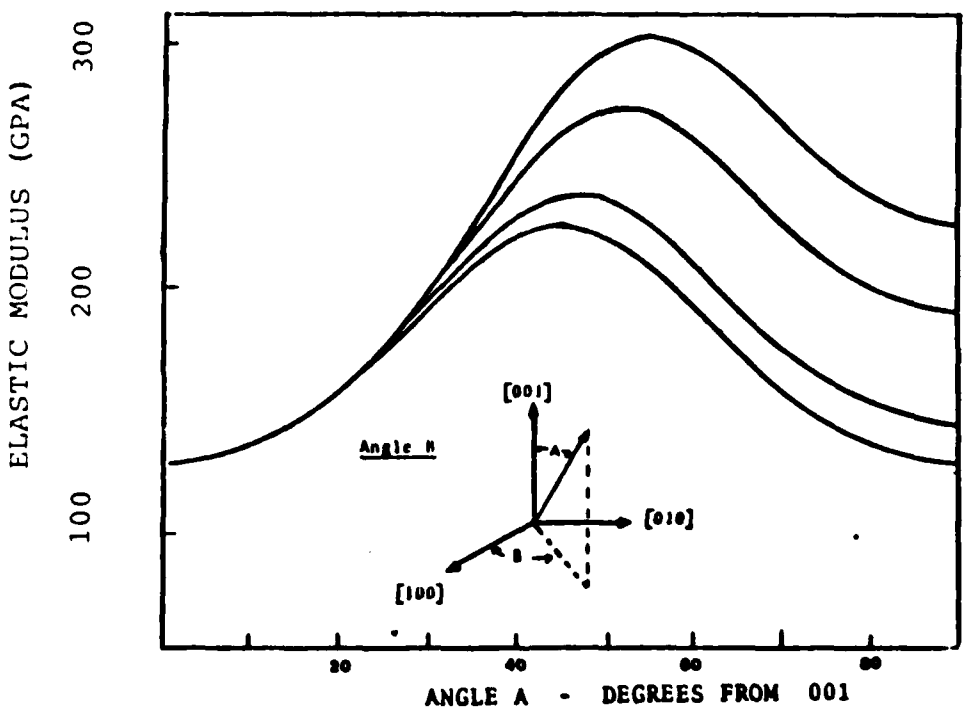

Figure 4. The Effect of Orientation on Elastic Modulus. Ref. 105.

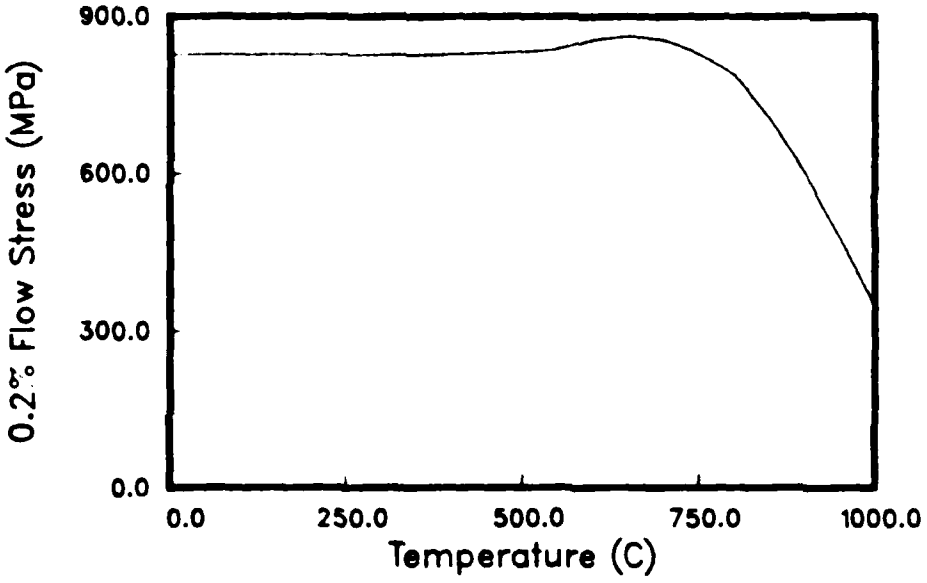

Figure 5. Flow Stress vs. Temperature Curve for Conventionally Cast MAR-M246. Ref. 68.

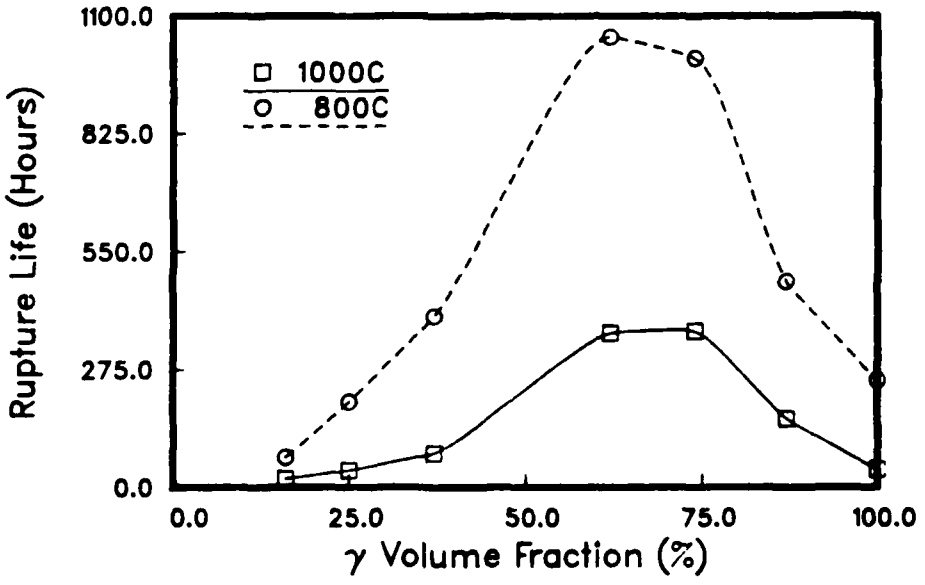

Figure 6. Relationship Between Creep Rupture Life and Volume Fraction v'. The peak rupture life occurs at about 60%. Ref. 36.

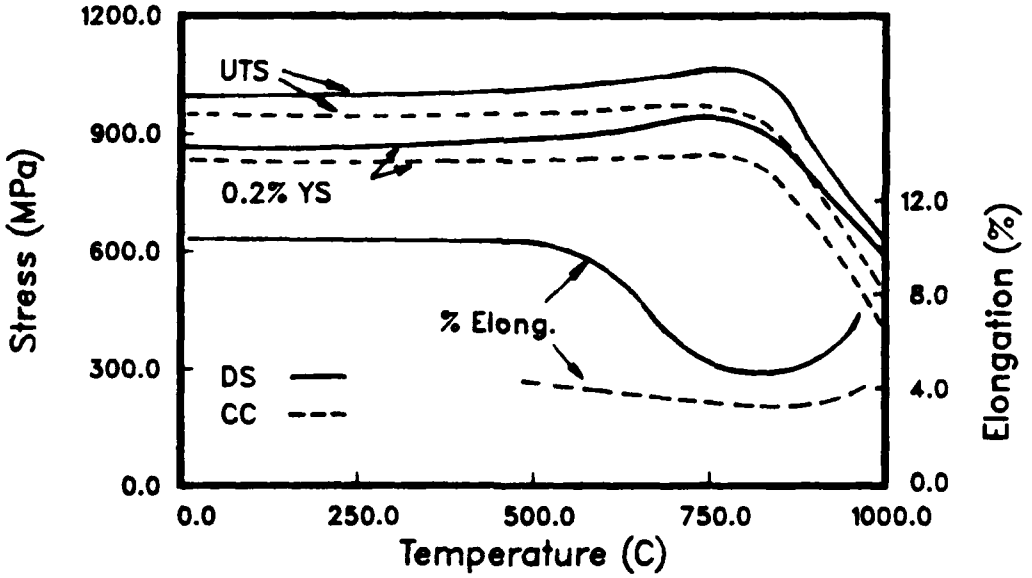

Figure 7. Flow Stress vs. Temperature Curve for Conventionally Cast and Directionally Solidified MAR-M200. The DS material shows an overall increase in elongation but has a pronounced ductility minimum at 871°C. Ref. 69.

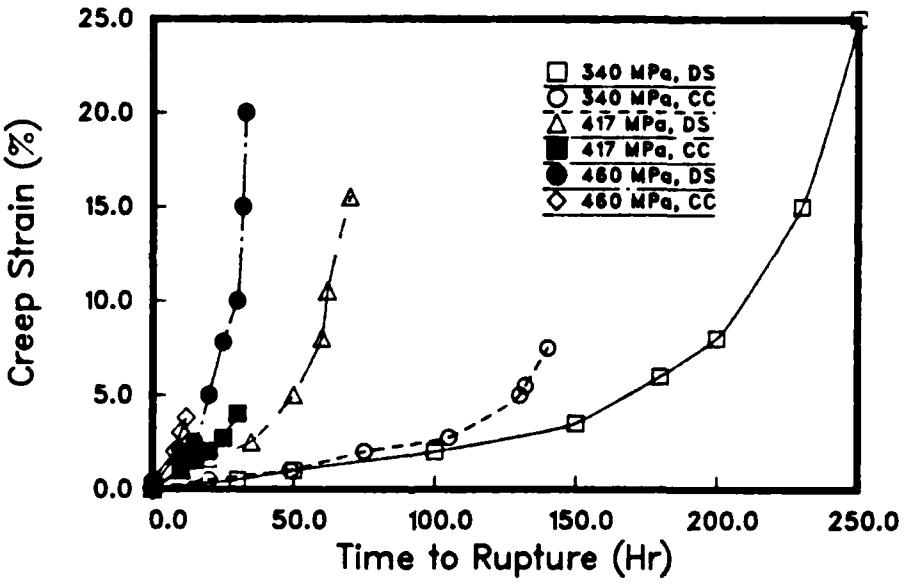

Figure 8. Tensile Creep Curves for Conventionally Cast and Directionally Solidified MAR-M246. The DS material shows a delayed transition to tertiary creep and increased creep ductility. Ref. 99.

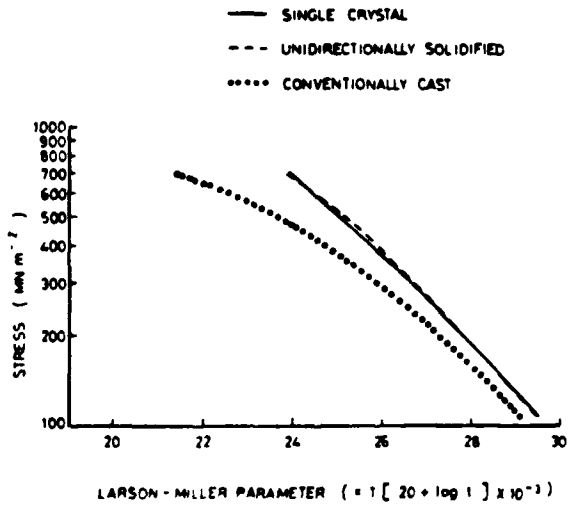

Figure 9. Larson-Miller Curve for MAR-M246. Note the improvement for single crystal and directionally solidified forms over conventionally cast material. Ref. 98.

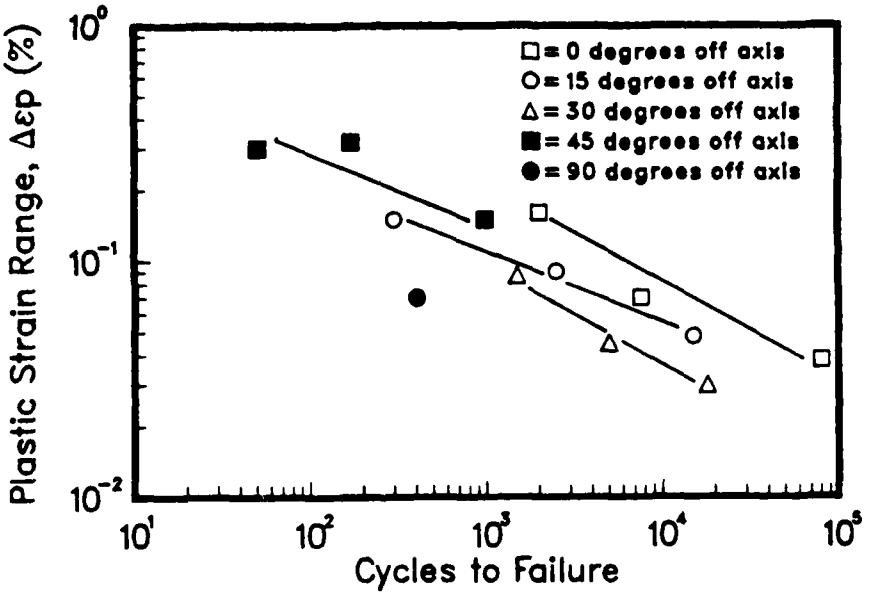

Figure 10. Influence of Orientation on LCF Life for DS Rene 120. Tested in strain control, at 982°C and 20 Hz. For a given plastic strain range, life is longest for longitudinal orientations. Ref. 100.

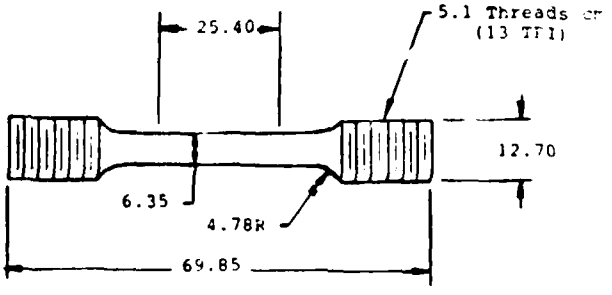

All dimensions in millimeters

a.

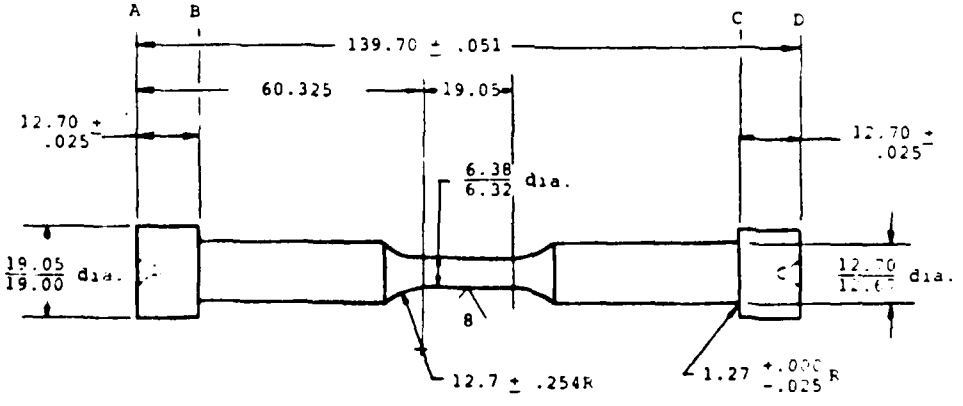

Surfaces A, B, C, and D must be parallel within .025 mm
All dimensions are in millimeters

b.

Figure 11. Specimen Geometries.
a. Tensile specimen, with threaded ends.
b. Smooth bar low cycle fatigue specimen, with button head ends.

a.

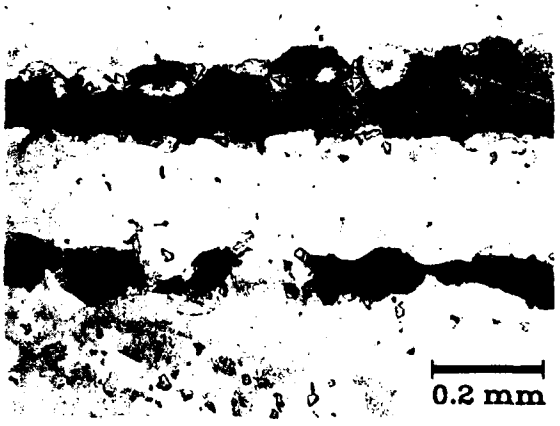

b.

Figure 12. Optical Micrographs of As-received Structure.
a. Longitudinal orientation, showing transverse grain boundaries and tapered grains. Tensile axis is horizontal.
b. Longitudinal orientation. Note that the amounts of eutectic and carbide constituent along the boundaries are not uniform.

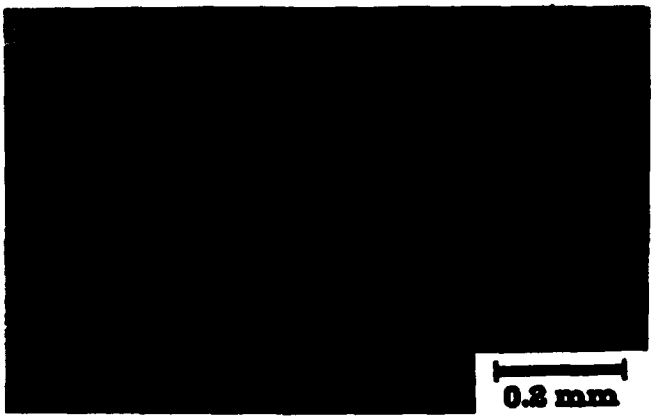

Figure 13. Optical Micrograph of As-received Structure. When viewed in the transverse orientation, the carbides display a slight script morphology. Note the eutectic constituent at grain boundaries.

a.

b.

Figure 14. TEM Micrographs of As-received Structure. Foils were cut transverse to stress axis.
a. <200> bright field. Note the sharp cube corners of the precipitates and the dislocations on the interface. The volume fraction of precipitate was found to be 60% (107).
b. <100> dark field, imaging the precipitates.

a.

b.

Figure 15. TEM Micrographs of a Eutectic Region in the As-received Microstructure. Diffraction spots from the carbides in a. were used to form the dark field image shown in b. The carbides are brightly imaged (arrows).

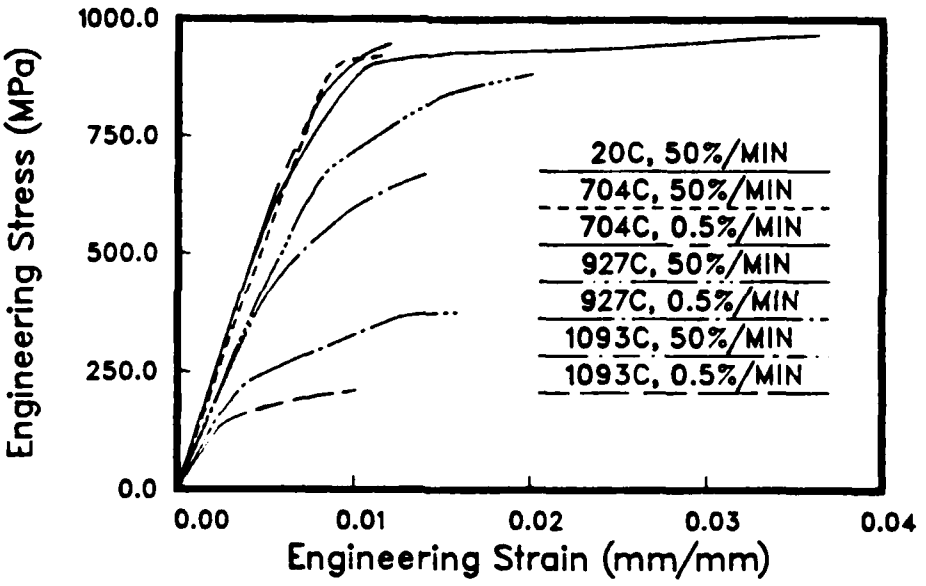

Figure 16. Tensile Stress-Strain Curves. The 20°C and 704°C, 50%/min. curves displayed a lower slope after yielding than the other tests. Note that the extensometer was removed before failure to prevent damage upon speciimen separation.

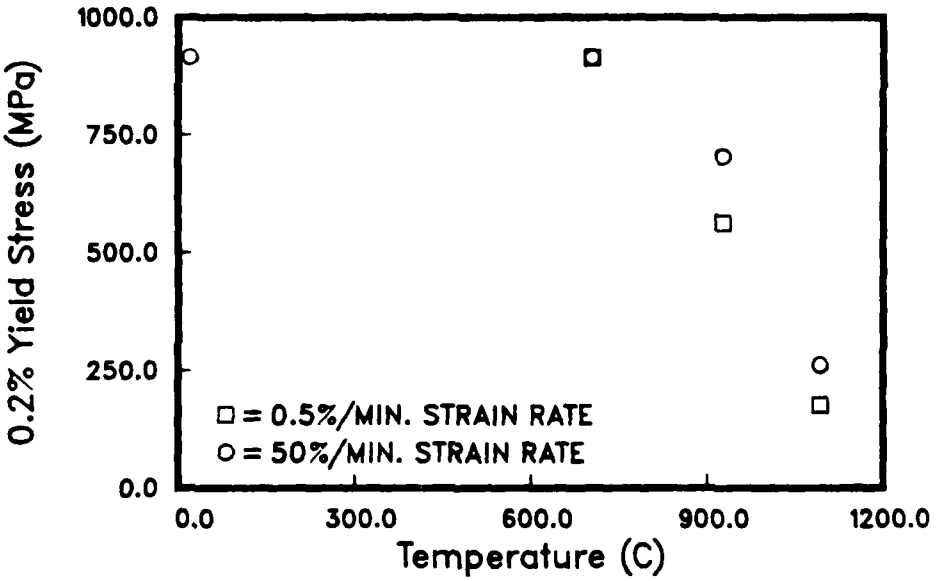

Figure 17. 0.2% Yield Stress vs. Temperature. There is a strong reduction in strength at the 0.5%/minute strain rate at the higher temperatures.

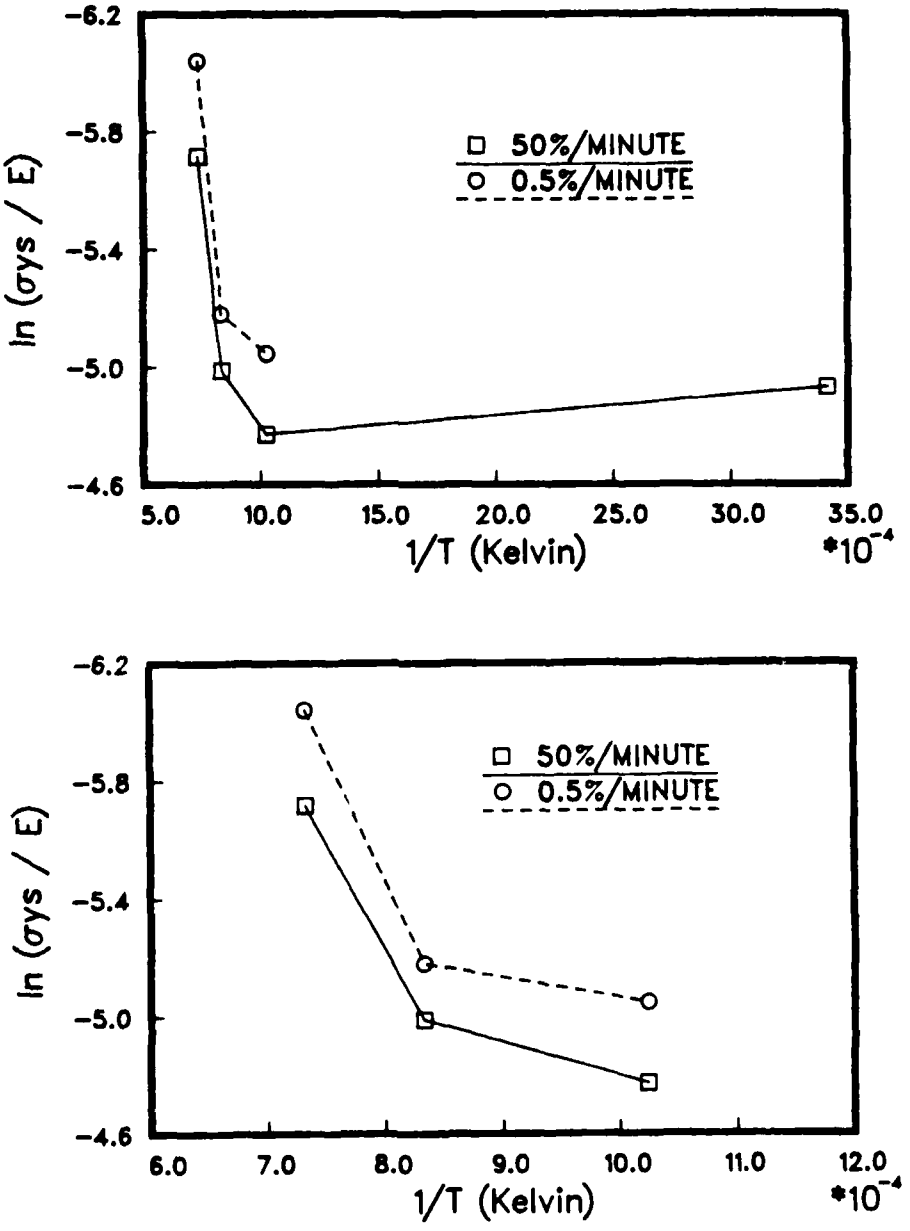

Figure 18. Thermal Activation in Yielding. Note the equivalent slope between strain rates above 927°C and the steeper slope at 0.5%/minute strain rate between 704°C and 927°C. In the lower graph , the room temperature point is omitted and the scale is expanded for clarity.

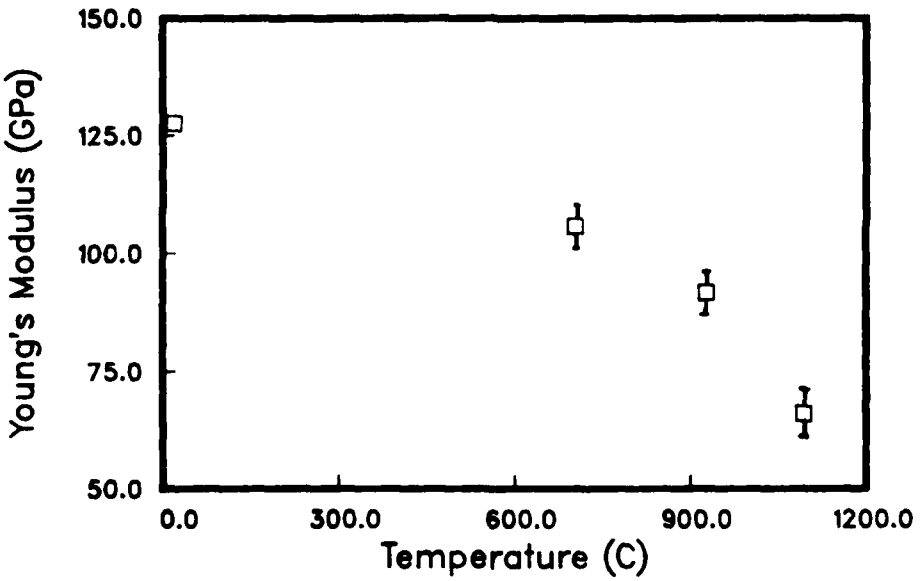

Figure 19. Young's Modulus vs. Temperature.

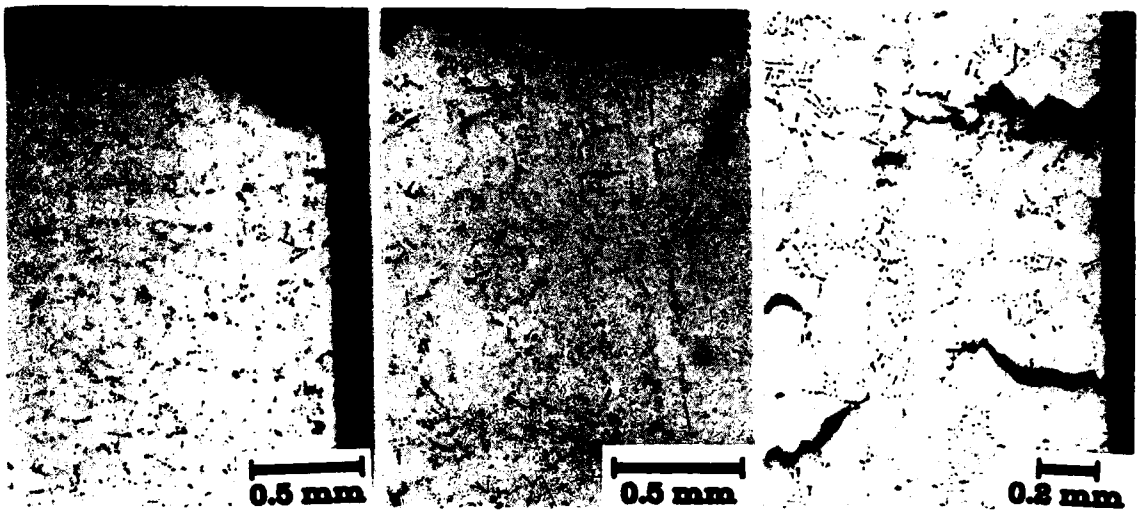

a. b. c.

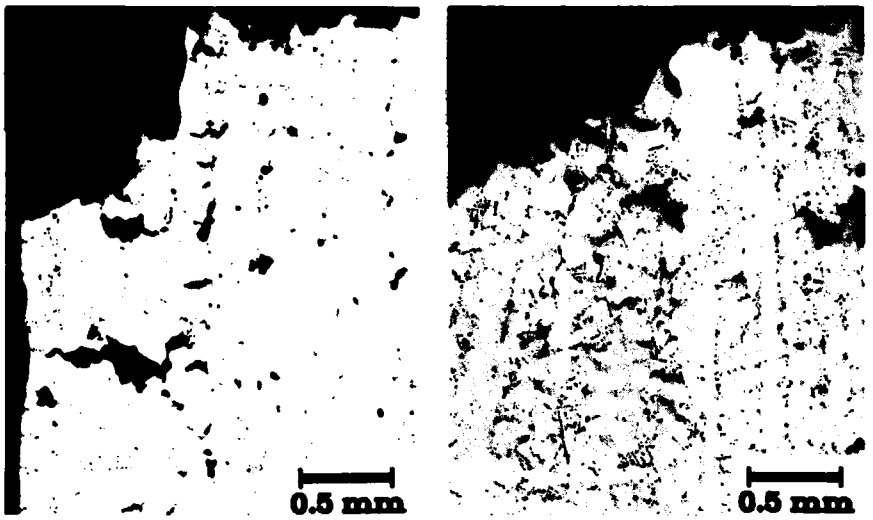

d. e.

Figure 20. Optical Micrographs of Failed Tensile Tests.
a. 20°C, 50%/minute. No void formation.
b. 927°C, 50%/minute. No void formation.
c. 927°C, 0.5%/minute. Some void formation.
d. 1093°C, 50%/minute. Extensive void formation.
e. 1093°C, 0.5%/minute. Extensive void formation.

a.

b.

Figure 21. SEM Micrographs of Tensile Fracture Surfaces. a. 20°C, 50%/minute. Note the star shaped fracture morphology around the script carbides. b. 1093°C, 50%/minute. Fracture is much more ductile in appearance.

Figure 22. TEM Micrograph of Dislocation Substructure, for 20°C, 50%/minute Strain Rate. The linear dislocation structure and slip bands are indicative of particle shearing. Note the dislocations stored on the interfaces. Milligan (Ref. 110) has shown that the deformation behavior during yielding may be different than deformation during further plastic flow.

a.

b.

Figure 23. TEM Micrographs of Dislocation Substructure for tension, 704°C.
a. 50%/minute. Linear dislocations and heterogeneous slip.
b. 0.5%/minute. Some wavy and intersecting dislocations are evident.

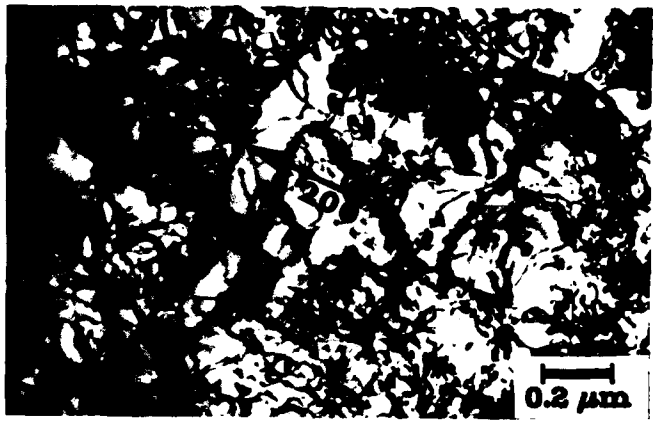

a.

b.

Figure 24. TEM Micrographs of Dislocation Substructure for Tension, 927°C.
a. 50%/minute. The substructure consists of wavy and intersecting dislocations.
b. 0.5%/minute. Note the dislocations on the interfaces and the wavy character of the dislocations.

a.

b.

Figure 25. TEM Micrographs of Dislocation Substructure for Tension, 1093°C.
a. 50%/minute. The deformation mode is homogeneous.
b. 0.5%/minute. Precipitate coarsening has occurred, and most dislocations are stored in the form of interfacial networks.

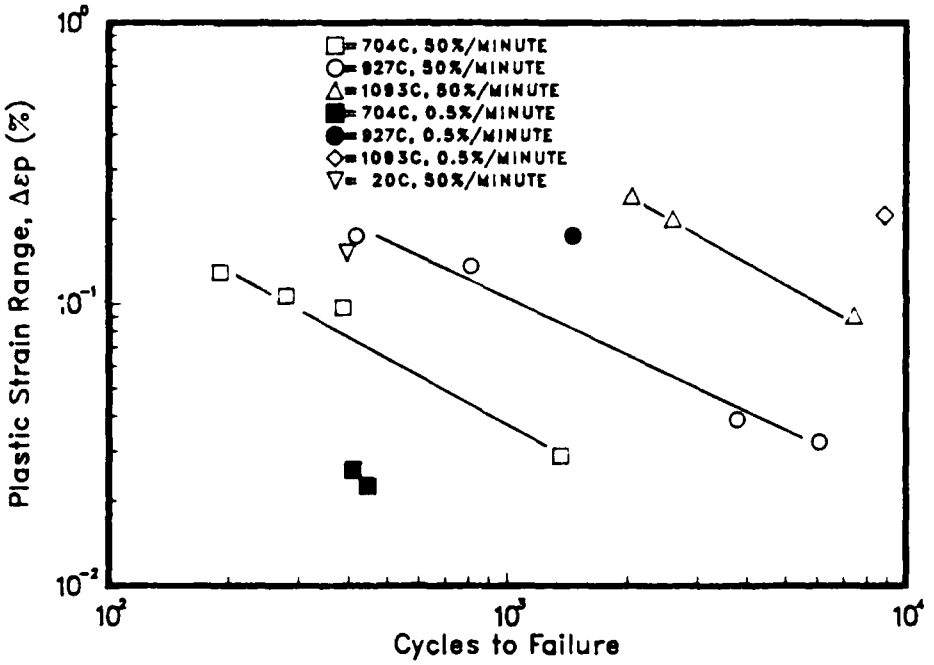

Figure 26. Coffin-Manson Plot of Fatigue Lives. Life is plotted against plastic strain range. The Coffin-Manson exponents for the 50%/minute tests were calculated using linear regression and are given below:

$704^{\circ}C$: b = .783
$927^{\circ}C$: b = .676
$1093^{\circ}C$: b = .762

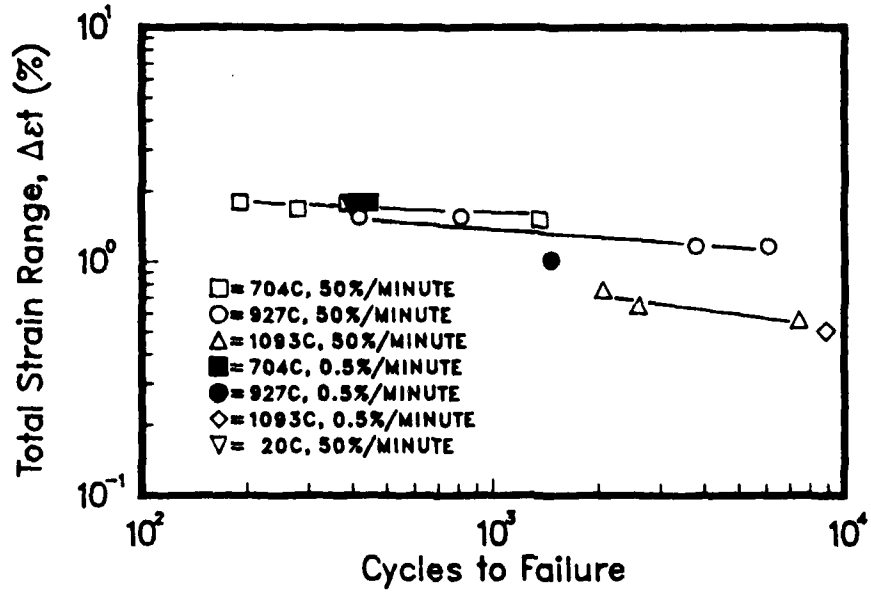

a.

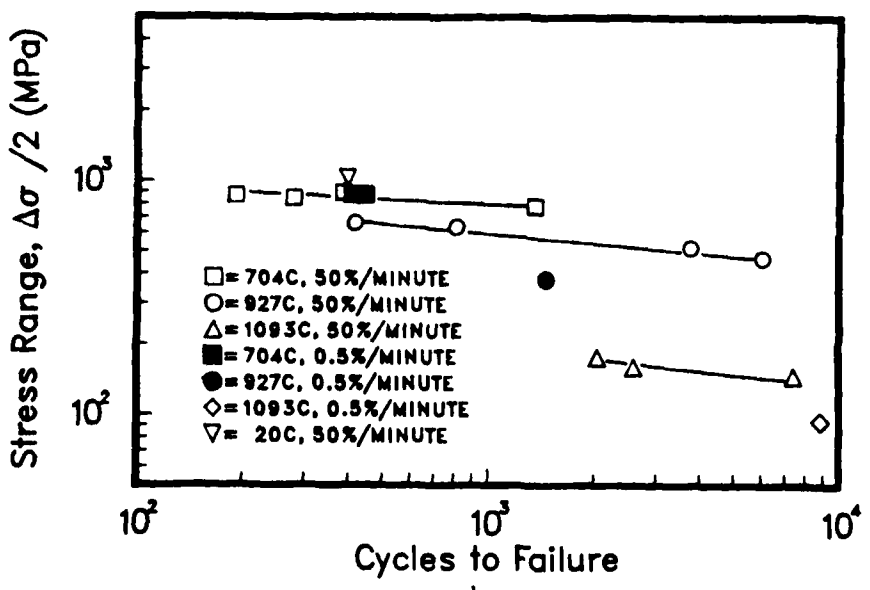

b.

Figure 27. Fatigue Life Plots.
a. Total strain range vs. life.
b. Stress range vs. life.

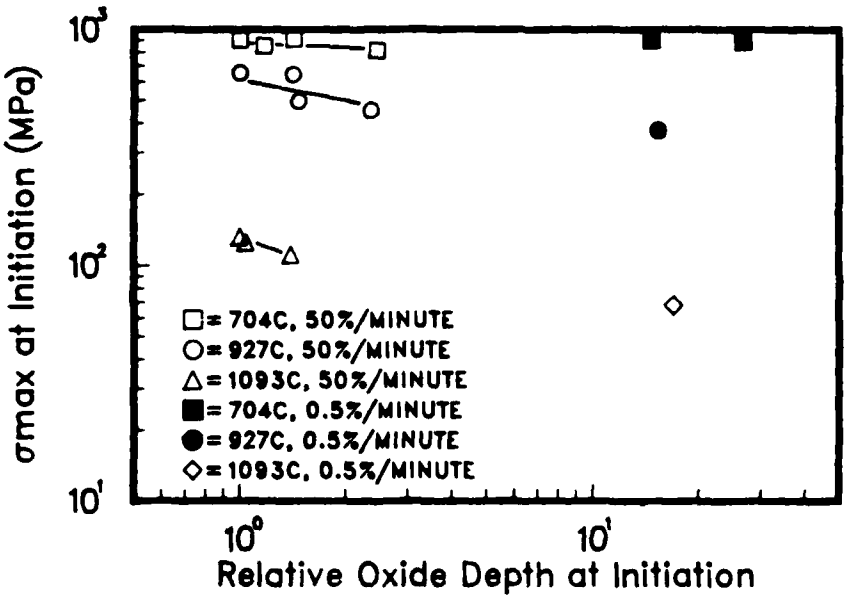

Figure 28. Stress at Initiation vs. Oxide Depth. This plot is based on the model proposed by Antolovich and coworkers (Ref. 85). The slopes of the data at 704°C and 927°C are nearly horizontal, indicating little dependence of life on oxidation, while a stronger dependence is noted at 1093°C.

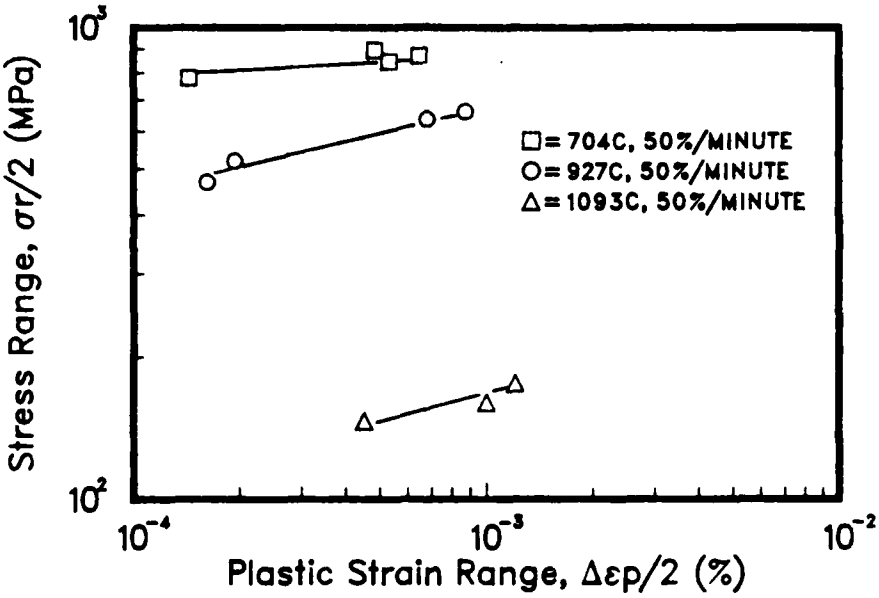

Figure 29. Cyclic Stress-Strain Curves. The n' value is lowest at 704°C.

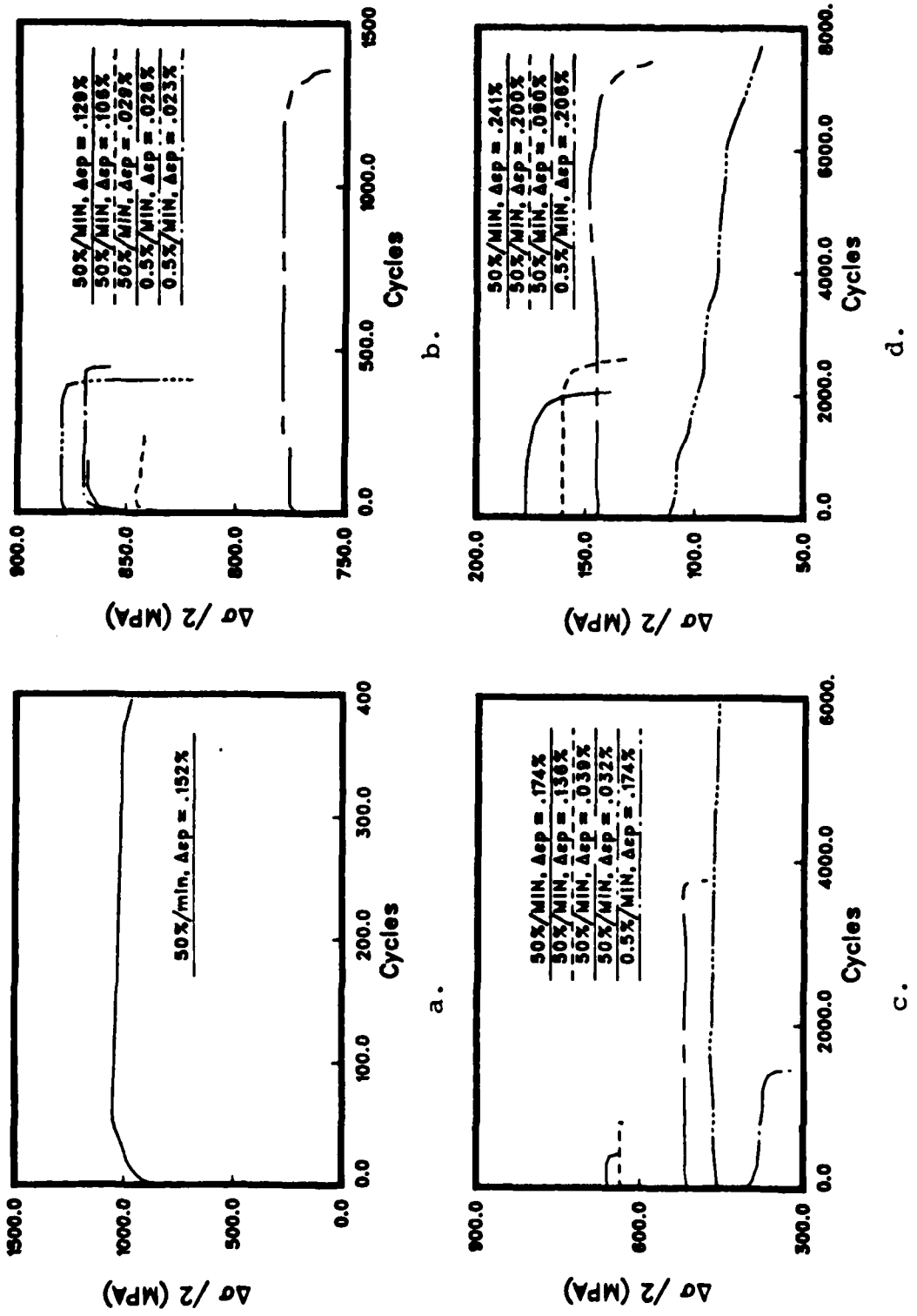

Figure 30. Cumulative Glide Curves.
a. 20°C b. 704°C
c. 927°C d. 1093°C

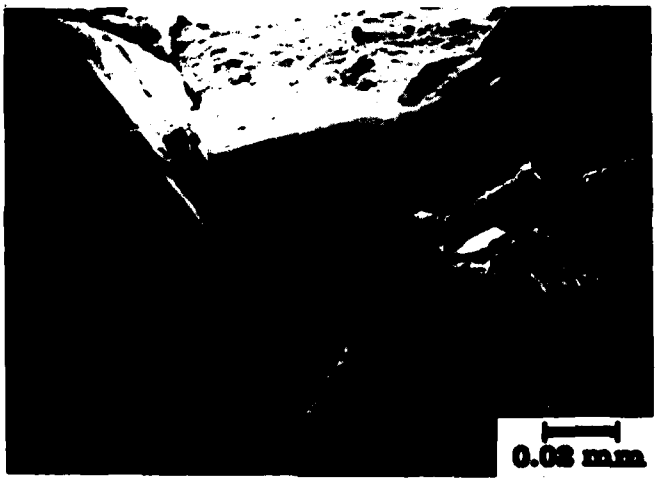

Figure 31. SEM Micrograph of Initiation at 20°C. Initiation of crack is due to slip around cracked interdendritic carbides.

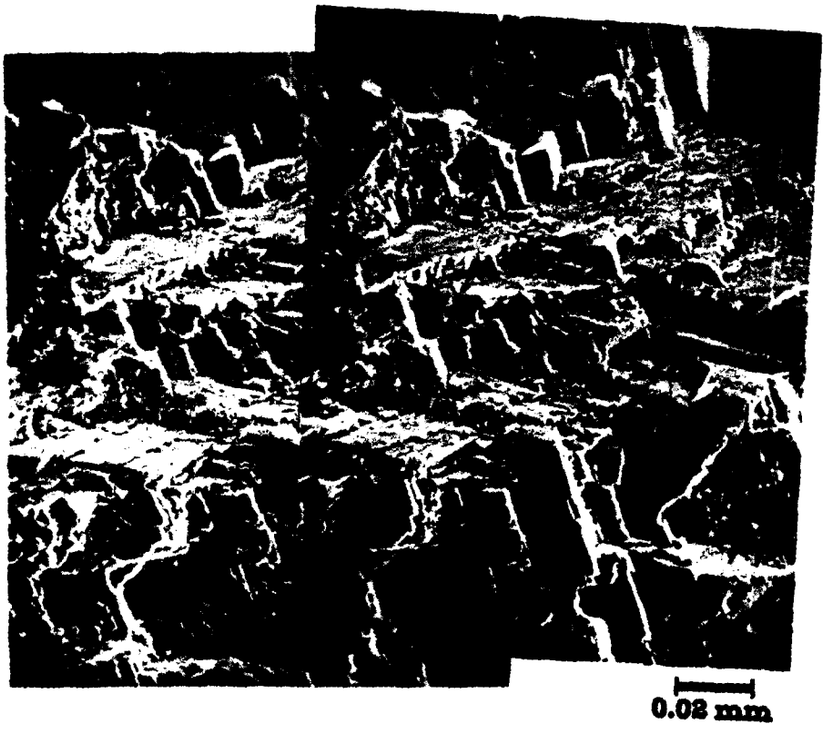

Figure 32. Stereopair of Fracture Surface, 20°C.

b.

Figure 33. SEM Micrographs of Fatigue Fracture Surfaces, 704°C.
a. 50%/minute. Propagation is crystallographic.
B. 0.5%/minute. Fracture is somewhat less crystallographic in character.

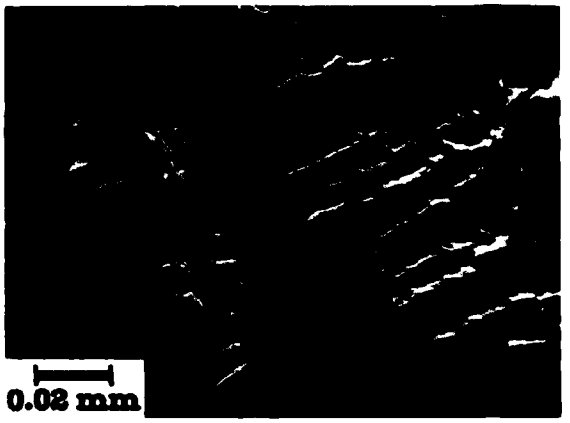

a.

b.

Figure 34. Initiation and Crack Behavior at 704°C.
a. SEM micrograph of initiation at transverse dendrite arm.
b. Optical micrograph showing transgranular cracking. Slight deflection occurred at grain boundaries.

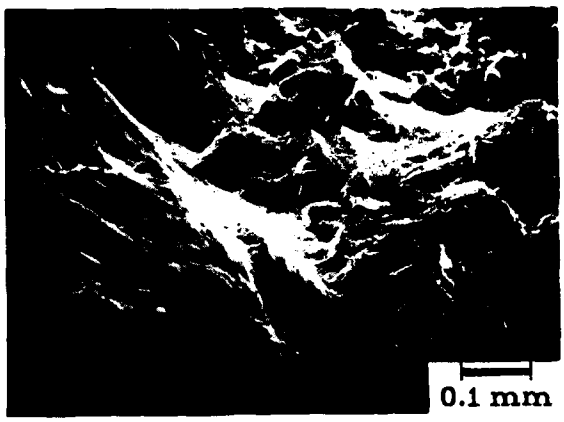

Figure 35. SEM Micrograph of Fatigue Fracture Surface, 927°C. The fracture surface is flat and featureless and highly oxidized. Similar fracture surface appearance was noted at both strain rates.

Figure 36. Optical Micrograph of Initiation at 927°C. Initiation has occurred due to the formation of oxide spikes at interdendritic regions, perpendicular to the tensile axis.

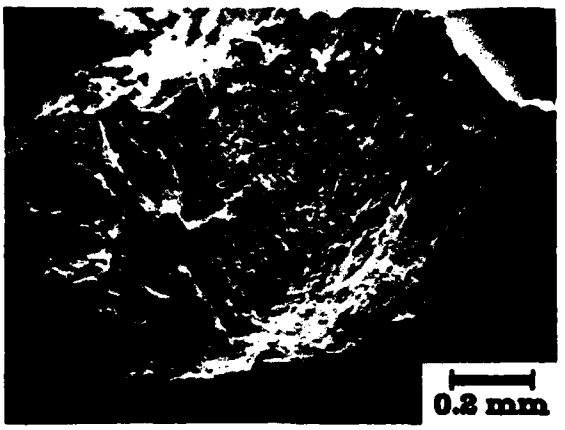

a.

b.

Figure 37. Fracture Behavior at 1093°C.
a. SEM micrograph of initiation region. The flat region near the surface is similar to the 927°C behavior. However, behind the initiation region, the crack path deviates from a plane normal to the stress axis.
b. Optical micrograph of secondary cracking observed at 1093°C.

Figure 38. Optical Micrograph of Oxidation at 1093°C, 0.5%/minute. Severe oxidation has occurred, resulting in precipitate depletion along the specimen surfaces and adjacent to fatigue cracks.

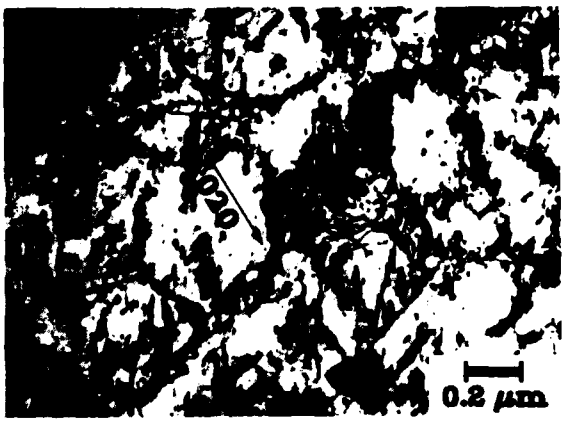

Figure 39. TEM Micrograph of LCF Dislocation Substructure, 20°C. The substructure is indicative of precipitate shearing. Note that linear dislocations are present within the precipitate, and dislocations are stored on the interfaces.

a.

b.

Figure 40. TEM Micrographs of LCF Dislocation Substructure, 704°C.
a. 50%/minute. Note the stacking faults and dislocations within the precipitate particles, indications of shearing. The dislocation marked "d" lies on the (101) plane.
b. 0.5%/minute.

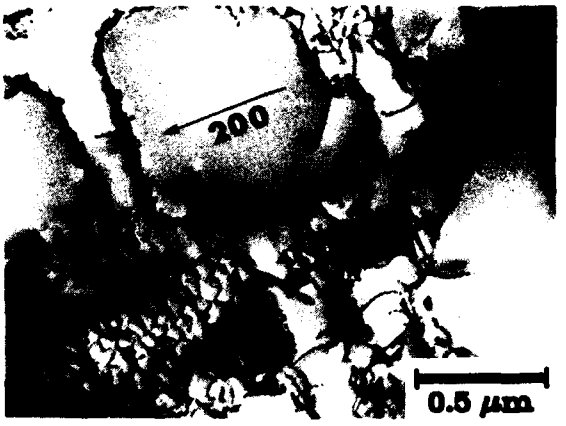

a.

b.

Figure 41. TEM Micrographs LCF Dislocation Substructure, 927°C.
a. 50%/minute. The overall dislocation density is lower and the initial formation of interfacial networks has occurred.
b. 0.5%/minute. Precipitate coarsening has occurred. Compare with Figure 42.

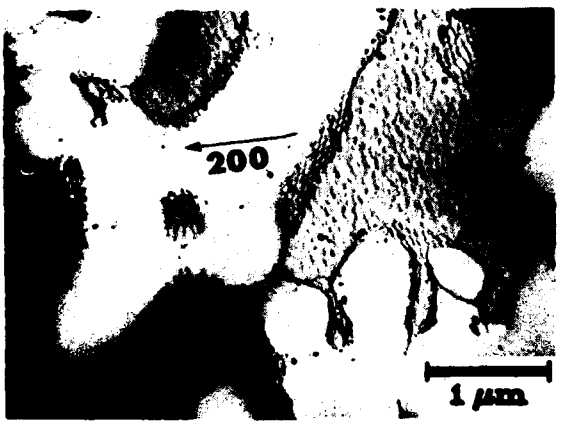

Figure 42. TEM micrograph of LCF Dislocation Substructure, 1093°C, 50%/minute. Precipitate coarsening is the dominant feature of the substructure, with all dislocations stored in interfacial arrays.

a.

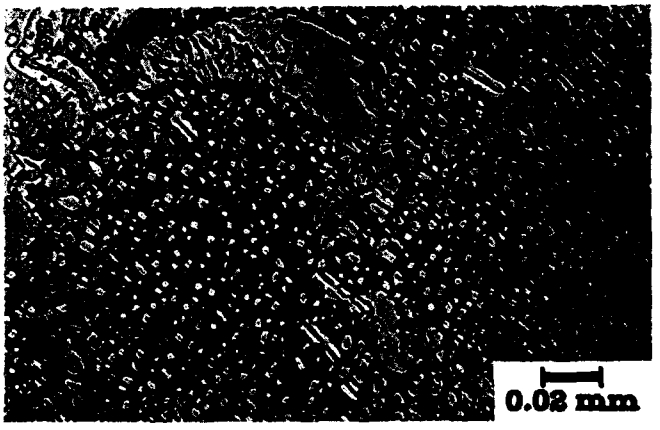

b.

Figure 43. Structure After 1093°C, 0.5%/minute LCF Test.
a. TEM micrograph of dislocation substructure. The overall dislocation density is quite low, with all dislocations stored in the interfaces.
b. Optical micrograph of coarsening that occurred during this test. The carbides have been almost completely resolutioned.

a.

b.

Figure 44. Optical Micrographs of Coarsening in Undeformed Specimens.
a. Structure after 49 hours at 927°C. Significant changes in the structure have not occurred.
b. Structure after 49 hours at 1093°C. Grain boundary depletion of the precipitate has occurred.

a.

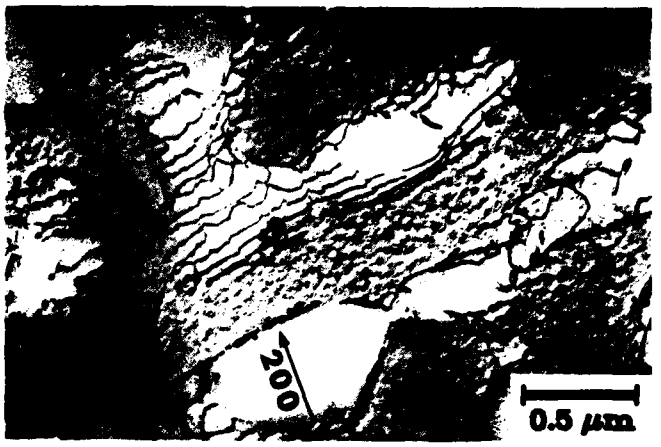

b.

Figure 45. TEM micrographs of Coarsening, Undeformed Samples.
a. 927°C, 49 hours.
b. 1093°C, 49 hours. Compare with Figure 42.

a.

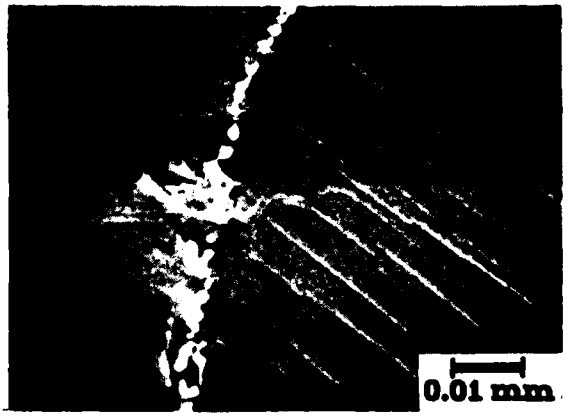

b.

Figure 46. Grain Boundary Slip Behavior in 20°C LCF Test.
a. Primary slip has occurred in both grains, with secondary slip on two systems in the grain on the left. Misorientation is approximately 28 degrees.
b. Primary slip has occurred only in the grain on the right, with some secondary slip in the grain on the left. Misorientation is approximately 7 degrees.

Figure 47. High Temperature Strain Extensometer.

1. Report No. NASA CR-175101 USAAVSCOM-TR-86-C-19	2. Government Accession No.	3. Recipient's Catalog No.

4. Title and Subtitle	5. Report Date
High Temperature Monotonic and Cyclic Deformation in a Directionally Solidified Nickel-Base Superalloy	May 1986
	6. Performing Organization Code
7. Author(s)	8. Performing Organization Report No.
Eric S. Huron	None
	10. Work Unit No.
9. Performing Organization Name and Address	11. Contract or Grant No.
Georgia Institute of Technology School of Materials Engineering Atlanta, Georgia 30332-0245	NAG 3-503
	13. Type of Report and Period Covered
12. Sponsoring Agency Name and Address	Contractor Report
NASA Lewis Research Center, Cleveland, Ohio 44135 and U.S. Army Aviation Research and Technology Activity - (AVSCOM), Propulsion Directorate, Lewis Research Center, Cleveland, Ohio 44135	14. Sponsoring Agency Code 533-13-00

15. Supplementary Notes

Intermediate report. Project Managers: Robert C. Bill, Propulsion Directorate, U.S. Army Aviation Research and Technology Activity - AVSCOM; Rebecca A. MacKay, Materials Division, NASA Lewis Research Center. This report was a thesis submitted in partial fulfillment of the requirements for the degree Master of Science in Metallurgy to Georgia Institute of Technology, Atlanta, Georgia in March 1986.

16. Abstract

Directionally solidified (DS) MAR-M246+Hf was tested in tension and fatigue, at temperatures from 20 °C - 1093 °C. Tests were performed on (001) oriented specimens at strain rates of 50 % and 0.5 % per minutes. In tension, the yield strength was constant up to 704 °C, above which the strength dropped off rapidly. A strong dependence of strength on strain rate was seen at the higher temperatures. The deformation mode was observed to change from heterogeneous to homogeneous with increasing temperature. Low Cycle Fatigue tests were done using a fully reversed waveform and total strain control. For a given plastic strain range, lives increased with increasing temperature. For a given temperature, strain rate had a strong effect on life. At 704 °C, decreasing strain rates decreased life, while at the higher temperatures, decreasing strain rates increased life, for a given plastic strain range. These results could be explained through considerations of the deformation modes and stress levels. At the higher temperatures, marked coarsening caused beneficial stress reductions, but oxidation limited the life. The longitudinal grain boundaries were found to influence slip behavior. The degree of secondary slip adjacent to the boundaries was found to be related to the degree of misorientation between the grains.

17. Key Words (Suggested by Author(s))	18. Distribution Statement
Directional solidification, Low cycle fatigue testing, Nickel-base superalloy	Unclassified-unlimited STAR Category 26

19. Security Classif. (of this report)	20. Security Classif. (of this page)	21. No. of pages	22. Price*
Unclassified	Unclassified	171	A08

*For sale by the National Technical Information Service, Springfield, Virginia 22161

A

END

DTIC

9-86